Novel Growth Routes and Fundamental Understanding of Pseudo-One-Dimensional Materials

by

Kedi Wu

A Dissertation Presented in Partial Fulfillment
of the Requirements for the Degree
Doctor of Philosophy

Approved June 2018 by the
Graduate Supervisory Committee:

Sefaattin Tongay, Chair
Matthew Green
Houlong Zhuang

ARIZONA STATE UNIVERSITY

August 2018

ABSTRACT

Recently, two-dimensional (2D) materials have emerged as a new class of materials with highly attractive electronic, optical, magnetic, and thermal properties. However, there exists a sub-category of 2D layers wherein constituent metal atoms are arranged in a way that they form weakly coupled chains confined in the 2D landscape. These weakly coupled chains extend along particular lattice directions and host highly attractive properties including high thermal conduction pathways, high-mobility carriers, and polarized excitons. In a sense, these materials offer a bridge between traditional one-dimensional (1D) materials (nanowires and nanotubes) and 2D layered systems. Therefore, they are often referred as pseudo-1D materials, and are anticipated to impact photonics and optoelectronics fields.

This dissertation focuses on the novel growth routes and fundamental investigation of the physical properties of pseudo-1D materials. Example systems are based on transition metal chalcogenide such as rhenium disulfide (ReS_2), titanium trisulfide (TiS_3), tantalum trisulfide (TaS_3), and titanium-niobium trisulfide ($Nb_{(1-x)}Ti_xS_3$) ternary alloys. Advanced growth, spectroscopy, and microscopy techniques with density functional theory (DFT) calculations have offered the opportunity to understand the properties of these materials both experimentally and theoretically. The first controllable growth of ReS_2 flakes with well-defined domain architectures has been established by a state-of-art chemical vapor deposition (CVD) method. High-resolution electron microscopy has offered the very first investigation into the structural pseudo-1D nature of these materials at an atomic level such as the chain-like features, grain boundaries, and local defects.

Pressure-dependent Raman spectroscopy and DFT calculations have investigated the origin of the Raman vibrational modes in TiS_3 and TaS_3, and discovered the unusual pressure response and its effect on Raman anisotropy. Interestingly, the structural and vibrational anisotropy can be retained in the $Nb_{(1-x)}Ti_xS_3$ alloy system with the presence of phase transition at a nominal Ti alloying limit. Results have offered valuable experimental and theoretical insights into the growth routes as well as the structural, optical, and vibrational properties of typical pseudo-1D layered systems. The overall findings hope to shield lights to the understanding of this entire class of materials and benefit the design of 2D electronics and optoelectronics.

DEDICATION

I DEDICATE THIS DISSERTATION TO MY FAMILY.

ACKNOWLEDGMENT

First, and foremost, I would like to express my sincere gratitude to my advisor Dr. Sefaattin Tongay for his endless support and guidance in my trail of pursuing Ph.D. Within the past four years, Sef has been endlessly supporting my Ph.D. study and research with his patience, encouragement, and enormous knowledge. I have been feeling deeply grateful for the time we spent together, starting from the very first e-mail he sent to me. This dissertation would never have been accomplished without his dedication.

I would like to thank my committee members: Dr. Matthew Green, Dr. Houlong Zhuang, and Dr. Hanqing Jiang. Thank you for your time serving as my committee members and your valuable suggestions to this dissertation.

I am very grateful to my collaborators: Dr. Houlong Zhuang, Dr. Hasan Sahin, and their teams for performing theoretical calculations for my research. Special thanks to Dr. Emmanuel Soignard for the insightful suggestions he offered and discussions we had.

I thank all the alumni and current members in the group: Aslihan Suslu Tuna, Xiuqing Meng, Yuxia Shen, Sijie Yang, Hui Cai, Bin Chen, Anupum Pant, Wilson Kong, Mark Blei, Ashutosh Agarwal, Ying Qin, Yi Zhou, Han Li, Kentaro Yumigeta, Dipesh Trivedi, Debarati Hajra, Juliana Bennett, Sarah Alamdari, and Eddie Vinciguerra.

Finally, the most special thank you goes to my wife Shiyao Xu.

TABLE OF CONTENTS

Page

CHAPTER Page

CHAPTER Page

CHAPTER Page

LIST OF TABLES

Table Page

LIST OF FIGURES

Figure Page

Figure Page

Figure Page

Figure Page

Figure Page

Chapter 1 INTRODUCTIONS

1.1. Emerging of two-dimensional (2D) layered materials

Two-dimensional (2D) layered materials consist of layered sheets weakly coupled through van der Waals (vdWs) interaction, allowing the isolation into free-standing, atomically thin layers[1-2]. After the first demonstration of semi-metallic carbonaceous graphene[3] sheets in 2004, layered materials have attracted great research interests in various cross sections of sciences owing to the significant difference in their properties from their bulk counter-parts as well as conventional materials in various aspects such as the strong light-matter interaction[4], rich exciton complexes[5-6], large exciton binding energy[7], mechanical flexibility[8-9], and spin-orbit degree of freedom[10-12] due to strong quantum confinement effects. The current research of 2D materials is mostly focused on expanding the regime of 2D materials, exploring their extraordinary optical, electrical, and mechanical properties, and demonstrating state-of-art devices for various applications[13-15].

As a well explored 2D material, semi-metallic graphene consists of atomically thin sheets where sp^2 hybridized carbon atoms are hexagonally connected. The conduction band and valence band edges of intrinsic graphene touch each other at the Dirac points in the Brillouin zone, thus the carriers in graphene behaves as if massless Dirac Fermions that can move at the speed of light, leading to extremely high theoretical carrier mobility[3, 16]. Due to its zero-bandgap nature, graphene is also considered as semi-metallic. Within the past decade, extensive scientific progress has been made to explore the extraordinary

optical, thermal, mechanical, and electrical properties[17-19] of this graphene, demonstrating graphene as an attractive candidate for flexible photo-electronic devices. As mentioned earlier, however, pristine graphene lacks a bandgap and as a result, it is impossible to achieve a high on/off ration in FET devices made from graphene. Even though such techniques as strain engineering and chemical functionalization can open a reasonable bandgap in graphene[20-21], extensive post-processing also restrict the overall device performance by diminishing the carrier mobility.

Layered semiconducting transition metal chalcogenides[22] (TMDs) form a large group of materials with a common chemical formula of MX_n, where M is a transition metal atom from group IV (Ti, Zr, or Hf), group V (V, Nb, or Ta), group VI (Mo or W) or group VII (Re), X represents a chalcogen (S, Se, or Te), and n equals from 1 to 5. In contrast to zero bandgap graphene, TMDs offer tunable bandgaps ranging from infrared to visible range[23-24] that are appropriate for high performance electrical devices[25]. Among the TMD families, the group VI transition metal dichalcogenides (TMDCs), including MoS_2, $MoSe_2$, WS_2, and WSe_2, present indirect to direct bandgap transition from bulk to monolayer due to the quantum confinement effect that changes the atomic orbital hybridization[26-28]. Specifically, for example, the indirect bandgap for bulk MoS_2 is 1.2 eV with the valance band maximum found at the Γ point. For the monolayer MoS_2, the band gap value increases to 1.9 eV with both the valance band maximum and conduction band minimum found at K point, showing a direct transition nature. These interesting properties in the quantum confinement limit has significant implications for a variety of applications and fundamental studies[29-30]. For instance, the chemically passivated surfaces of TMDC monolayers absorb and emit photon rather efficiently, and offer

unique opportunities to stack them vertically to fabricate atomically thin heterojunctions[31] for optoelectronic applications[32-33], and to possess rich-excitonic complexes[6, 34] for photonic applications. Another highly explored layered 2D material is hexagonal born nitride (*h*-BN). Like graphene, *h*-BN is composed of alternating boron and nitrogen atoms in a honeycomb architecture. However, the *h*-BN is an insulator with a large bandgap of up to 6 eV. The thermally and chemically stable *h*-BN 2D layers have been serving as a suitable dielectric substrate or isolation / protection layer[35] for graphene or TMC electronics.

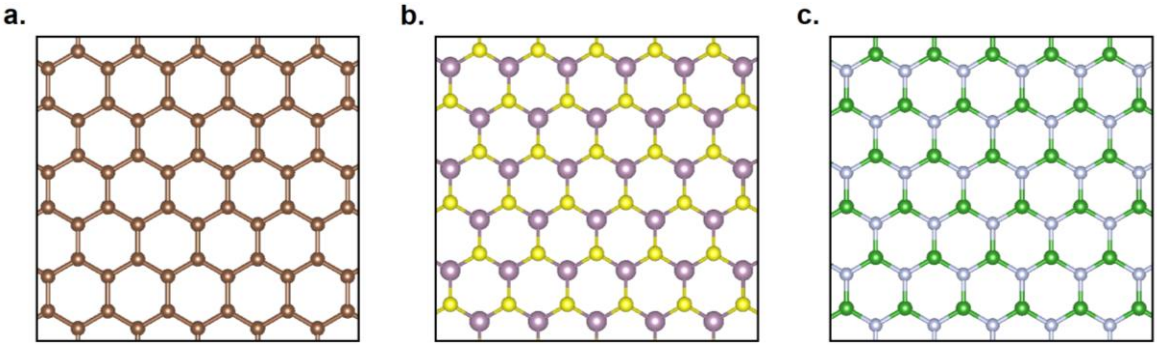

Figure 1.1 The lattice structure of the a. semi-metallic graphene, b. semiconducting MoS_2, and c. insulating h-BN.

Most of the layered materials are structurally anisotropic along *c*-axis (out-of-plane direction), whereas each individual 2D layer presents strong in-plane isotropy since they are atomically arranged identically along different lattice directions. The in-plane structure of typical isotropic 2D materials such as semi-metallic graphene, semiconducting MoS_2, and insulating *h*-BN are shown in **Figure 1.1.** There is no doubt that such isotropic 2D material systems have been well developed and investigated, exhibiting a variety of extraordinary properties over conventional materials. Due to the structural isotropy, these materials offer uniform / identical optical, electrical and

vibrational responses along different crystal orientations, and in return limits the applications where direction-selective functions are required. Based on this demand, the work presented in this thesis focus the layered materials with in-plane anisotropy and distinct angle-dependent behaviors.

1.2. Pseudo one-dimensional (1D) materials

Beyond the well explored families of the isotropic layered materials, there also exists a limited amount of 2D materials with reduced crystal symmetry to form 1D chain-like features. Therefore, this class of materials is generally referred as anisotropic 2D material, quasi-1D, or pseudo-1D materials. Despite the various structures in different systems, the common feature shared by this class of materials is geometrically anisotropy, which forms in plane zigzag/armchair or chain-like structures. The in-plane structure of selected pseudo 1D materials are shown in **Figure 1.2.**

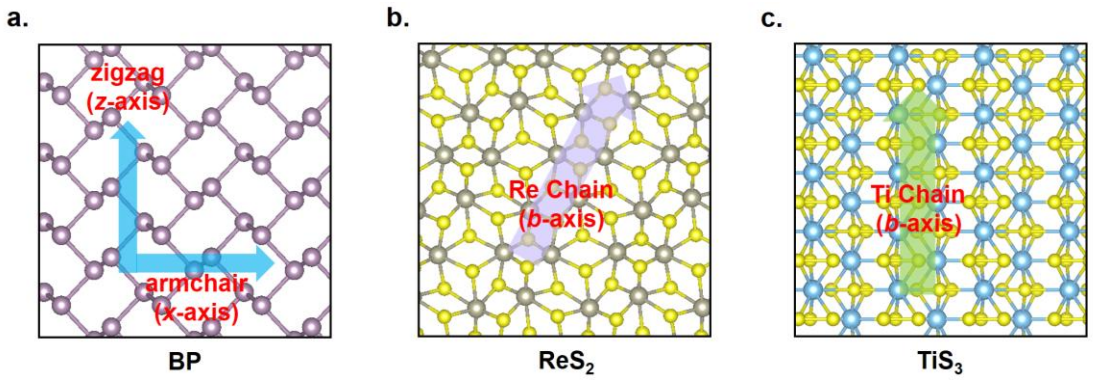

Figure 1.2 a. The armchair and zigzag structures of the BP along *x*- and *z*-axis. The chain structures along *b*-axis of b. ReS_2 and c. TiS_3

Examples of these anisotropic 2D materials include, but not limited to, black phosphorus (BPs) [36], the group III-VI, IV-VI compounds (GaTe and SnSe) group-VII

transition metal dichalcogenides[37-39] (ReS_2 and $ReSe_2$). And group-IV transition metal trichalcogenides[40] (TiS_3 and ZrS_3),. In these materials, strong metal-metal interaction takes place, causing small clusters of the metal atoms to form infinite chains extending along either *a*- or *b*-axis lattice direction without hurting the 2D lamellar in-plane structure. Combining the sheet-like 2D and chain-like 1D features, these material systems can be referred as 'pseudo one-dimensional materials' to highlight their chain-like 1D nature. Therefore, such pseudo 1D materials offer considerably distinct properties that share the novelty of both 1D and 2D materials, such as highly anisotropic optical absorption and emission, thermal conductivity, and carrier mobility.

1.2.1. Black phosphorous (BP)

As a relatively stable isotope of the phosphorous family, layered black phosphorous (BP)[36, 41] is emerging as a promising 2D material due to its widely tunable direct bandgap (0.3 - 2.0 eV) and high in-plane intrinsic carrier mobility. Owing to the strong structural anisotropy, the Hall mobility of holes measured at ultra-thin (15 nm) BP layers reaches above 1,000 and 600 $cm^2 V^{-1} s^{-1}$ along the *x*- and *y*-axis at 120 K[42], respectively, and the mobility measurements at 8 nm thick BP films also presents anisotropic electrical response, as shown in **Figure 1.3a**. Recent studies on the optical properties[43] of monolayer black phosphorus have shown that the exciton photoluminescence (PL) always presents a linearly polarized two-lobed feature regardless of the excitation laser and detection polarization (**Figure 1.3b**), which is in sharp contrast to other 2D materials. Density functional theory (DFT) calculations attributes this unusual effect to the emission from highly anisotropic bright excitons leading to polarized light emission. Therefore, the

light emission of BP can be polarized on demand after excitation by linearly or circularly polarized light.

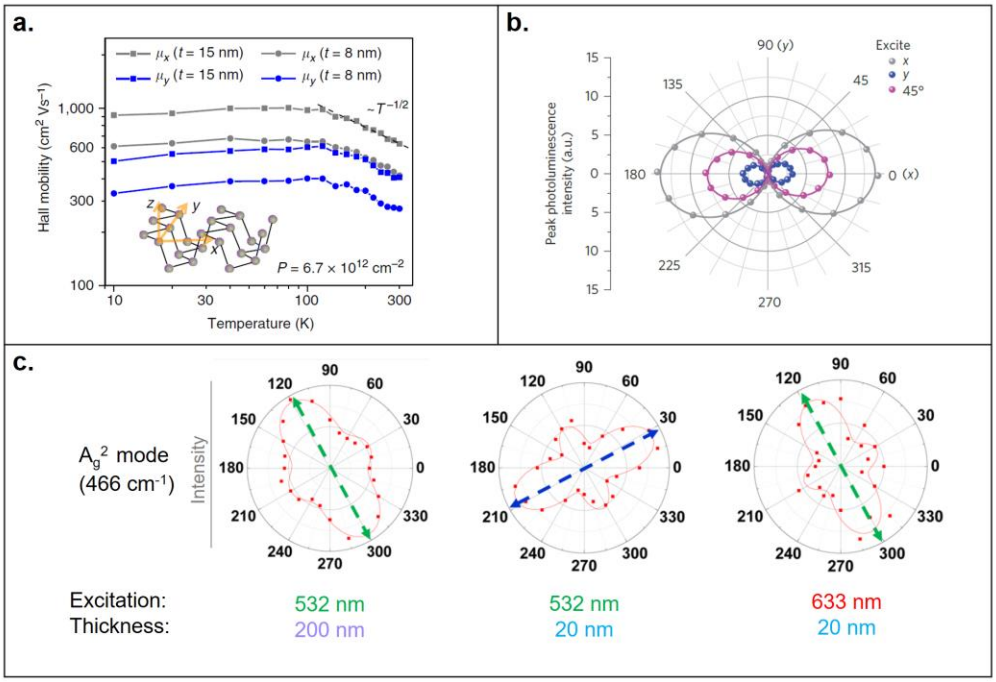

Figure 1.3 a. Anisotropic hole motilities of few-layer BP measured from 10 to 300K. Figure adapted with permission from ref. [42] b. Photoluminescence of BP presenting a linearly polarized feature. Figure adapted with permission from ref. [43] c. Anisotropic Raman scattering of the A_g^2 mode in BP measured at 20 nm and 200 nm thick flakes under different incident laser energy. Figure adapted with permission from ref. [44]

More interestingly, theatrical studies as well as experiment measurements suggest that the in-plane Raman anisotropy of black phosphorous relies on flake thickness as well as photon and phonon energies[44]. Specifically, results show that anisotropic features of the Raman modes vary with incident photon energy as well as flake thickness, indicating the anisotropic electron-photon and electron-phonon interactions. For example, angle dependent Raman intensity of the A_g^2 mode taken on two flakes of 20 and 200 nm thick under different laser wavelength show distinct two-lobed features as shown in **Figure**

1.3c However, the anisotropic optical absorption characteristics of BP flakes of various thickness retain the same even under different incident photon energy, indicating optical absorption seems to be a more reliable and simple way to identify the crystalline orientation of BP than Raman spectroscopy. However, pristine black phosphorus is environmentally unstable, which may limit its broader applications.

1.2.2. Titanium trisulfide (TiS_3)

Titanium trisulfide (TiS_3) belongs to group-IV transition metal trichalcogenides with the chemical formula of MX_3 (M = Zr, Ti, Hf and X = S, Se) that are known to be anisotropic 2D system. Recently, TiS_3 has attracted the interests from researchers due to its theoretically calculated 1.0 eV direct gap[45] and the anisotropic optical, vibrational, and electronic properties[46-47]. TiS_3 possess strong optical absorption anisotropy as the incident light is polarized along *a*- and *b*-axis (**Figure 1.4a**). The Raman intensity of the peak of taken from 3 nm thick TiS_3 nanosheets also displays angle dependent response as shown in **Figure 1.4b**. The electrical anisotropy of TiS_3 has been demonstrated by field effect transistors (FETs)[48]. Due to the strong in-plane anisotropy, TiS_3 nanosheets measure polarized carrier mobility of 40 $cm^2 V^{-1} s^{-1}$ along the *a*-axis whereas 80 $cm^2 V^{-1} s^{-1}$ along

the *b*-axis a shown in **Figure 1.4c**.

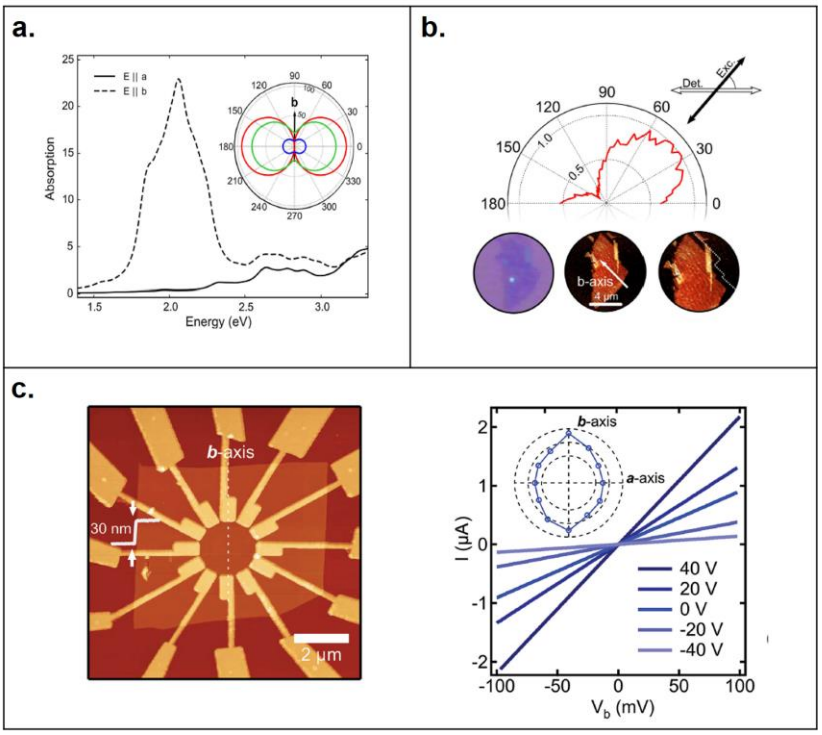

Figure 1.4 Calculated anisotropic optical absorption of TiS_3 as incident light is a polarized along *a*- and *b*-axis, and (inset) angle-dependent transmittance spectrum. Figure adapted with permission from ref. [47] b. Anisotropic Raman intensity of the 370 cm^{-1} peak. Figure adapted with permission from ref. [47] c. Device geometry and anisotropic electrical properties of TiS_3 FET. Figure adapted with permission from ref. [48]

Despite above remarkable work on TiS_3, there still exists a gap between a systematic work forcing the fundamental properties and deep origins of the chain behaviors in such pseudo-1D materials. The studies of the quasi-1D material is still at a seminal stage compared to in-plane isotropic 2D materials. For example, the fundamental vibrational properties of TiS_3, such as the origins of experimentally measured Raman peaks and theoretically calculated vibrational dispersion are still mysterious. Presently, all the prominent Raman modes of TiS_3 have been identified as A_g (out-of-plane) mode[49], but

further insight into the origins and behaviors of Raman modes remain mostly unknown. Lack of fundamental understanding of the vibrational properties of this material limits our ability to explore its potential in variety of applications and determination of its full anisotropic properties.

1.2.3. Rhenium disulfide (ReS_2)

Rhenium disulfide (ReS_2) is a member of group-VII transition metal dichalcogenides with an optical bandgap around 1.4 eV in bulk and 1.6 eV in monolayer form[37]. In comparison to those well explored group-VI TMDCs such as MoS_2 and WSe_2, each Re atom in ReS_2 has an extra electron. As a result, it is predicted that the hexagonal phase is unstable and the octahedral phase undergoes Peierl's distortion thus forms 1T' phase Highly oriented Re chains are formed along *b-axis* lattice direction due to the strong dimerization between the adjacent Re atoms[50]. The existence of in-plane anisotropy distinguishes ReS_2 from the other TMDCs structurally[37], optically[51], and electronically[52]. More recently, the effect of structural anisotropy on the optical[53] and vibrational[38] properties of 2D ReS_2 has been studied on exfoliated layers by various groups. Few-layer ReS_2 photodetectors[52] have demonstrated the capability of highly sensitive detection of polarized light, and photo-generated current reaches its maximum at 90°, which in consistent with the angle dependent optical absorption.

The current studies on ReS_2 have offered new routes to exploit the intrinsic anisotropy of this materials. Those studies, however, were mostly based on mechanically exfoliated ReS_2 that were ideal for understanding the fundamental properties and exploring the potential for device applications. To unravel their true potential, however, it

is essential to develop controlled and tunable growth methods to fabricate large scale 2D layers. Up until now, 2D ReS_2 nanosheets have already been synthesized by Keyshar *et.al* using low-temperature chemical vapor deposition (CVD) techniques[54] onto thermal SiO_2. Owing to amorphous nature of the SiO_2 substrate, however, the growth routes cannot be controlled to achieve high crystallinity that are required to yield high structural anisotropy. Therefore, it is essential to develop advanced techniques to synthesize highly crystalline ReS_2 monolayers with well-disciplined crystalline orientation and structural anisotropy. To fill the above gaps, the current work focused on the rediscovering the unique vibrational properties of TiS_3, developing techniques to synthesize highly crystalline 2D ReS_2 and investigating the anisotropic optical response with its structural anisotropy. Since, these pseudo-1D materials hold a promising potential for electronic devices where anisotropy is a desirable trait, our work hopes to open new paths for researchers in this area.

1.3. Alloying 2D materials

Traditional bulk and nanomaterials become useful and technologically relevant when selected atoms are alloyed into the host matrix to form binary, ternary, or other alloy systems, which enables the engineering of their optical, electronic, thermal, and chemical characteristics of a variety of material systems[55-58]. Recently, two-dimensional (2D) alloys of atomically thin materials have been demonstrated to achieve continuously tunable bandgap in the full composition range as demonstrated for $MoS_{2x}Se_{2-2x}$[59-63], $WS_{2x}Se_{2-x2}$[64-65], and $ReS_{2x}Se_{2-2x}$[66-67]. In addition, alloying transition metal atoms in ternary $Mo_xW_{1-x}S_2$[23, 68-69] and $Mo_xW_{1-x}Se_2$[70-71] has enabled engineering of dark and bright

excitonic states, exciton binding energies, and quasi- and single-particle band gaps to create highly luminescence 2D semiconducting materials. In these material systems, 2D alloying is accomplished across the same crystalline phases and the alloy systems retain their crystalline structure and phases independently from the composition values. Besides, there also exist a small number of alloys whose maternal binary counterparts crystalize in different phases. For instance, $MoTe_2$ is stable in both hexagonal (2H) or monoclinic (1T') phases whereas WTe_2 crystallize only in 1T' phase in nature[72-73]. Large changes in the crystal structure naturally affect their electronic band structures and as a result, these two phases exhibit semiconducting and metallic behavior in 2H and 1T' phases, respectively, and the structural (2H) and electronic (semiconducting) phase of $MoTe_2$ can be effectively engineered by laser irradiation[74] or W substitution[75-77]. In the following sections, we review several exciting findings observed in $MoS_{2x}Se_{2(1-x)}$, $WS_{2x}Se_{2(1-x)}$ and $GaSe_{1-x}Te_x$ alloy systems.

1.3.1. Tunable composition and bandgap engineering in $MoS_{2x}Se_{2(1-x)}$

Unlike the semi-metallic graphene, such monolayers of TMDCs as MoS_2, $MoSe_2$, WS_2, and WSe_2 possess direct bandgaps and offers strong light emission. For example, the direct bandgaps for 2H-MoS_2 and 2H-$MoSe_2$ are 1.86 eV and 1.56 eV, respectively. Due to the similarities in the atomic structure and stacking symmetry, alloying these two materials have offered the opportunity for continuous tunable bandgap and photoluminescence across the composition range.

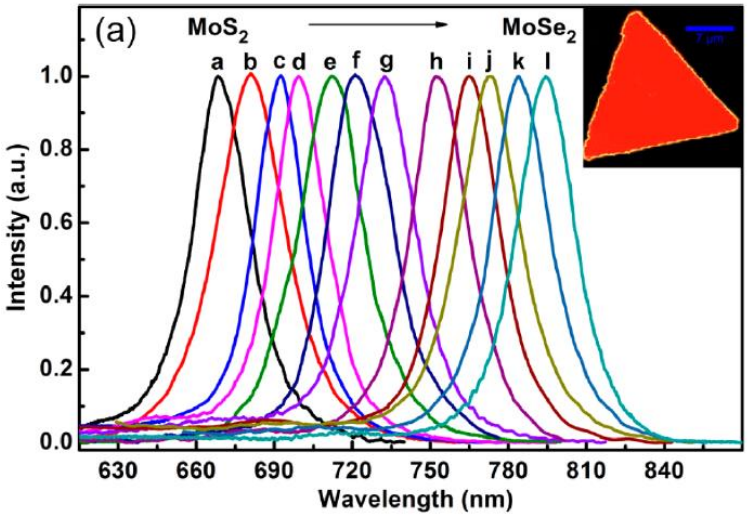

Figure 1.5 PL spectrum of the complete composition $MoS_{2x}Se_{2(1-x)}$ nanosheets and a PL mapping of a single ternary nanosheet (the inset, scale bar, 7 um) excited with a 488nm argon ion laser. Figure adapted with permission from ref. [78]

Honglai Li *et al*. reported a temperature gradient controlled CVD process and complete composition of $MoS_{2x}Se_{2(1-x)}$ nanosheets were synthesized in a one-step process using MoO_3 sulfur and selenium as precursors[78]. It is observed that the $MoS_{2x}Se_{2(1-x)}$ nanosheets gradually change the composition from $x = 1$ (pure MoS_2) at cold zone (796 ℃) to $x = 0$ (pure $MoSe_2$) at hot zone (830 ℃). Photoluminescence (PL) studies gives single emission bands for all the composition with the PL peak position shifting from 668 nm for MoS_2 to 795 nm for $MoSe_2$, which agrees with the band edge transition. Further analysis shows that the composition dependent band gap of the alloy does not follow a linear relation with the change in composition, instead the band gat can be fitted to $E_g(x) = xE_g(MoS_2) + (1 - x)E_g(MoSe_2) - bx(1 - x)$, where the x is composition, and the b ($b = 0.05$) represents the bandgap bowing parameter. In addition to the PL studies, Raman spectra spectroscopy was used to characterize the vibration modes of these alloys. Across the entire composition range, most of the alloys exhibit four modes, assigned as

$A_{1g(Se–Mo)}$, $E_{2g(Se–Mo)}$, $E_{2g(S–Mo)}$, and $A_{1g(S–Mo)}$, respectively. With decreasing of the sulfur molar fraction (*x*), all the modes shift to lower wavenumber, and the $E_{2g(S–Mo)}$ and $A_{1g(S–Mo)}$ modes gradually become weaker until eventually absent $MoSe_2$. These highlighted results developed a simple one-step CVD method to synthesize 2D $MoS_{2x}Se_{2(1–x)}$ alloy nanosheets with high crystallinity, and offered novel routes to achieve continuous bandgap engineering in 2D semiconducting TMDCs.

1.3.2. Tunable electronic properties in $WS_{2x}Se_{2(1–x)}$

Alloying selected elements introduces a significant number of impurities / dopants into host matrixes and offers the opportunity to control the electric properties. It has been recently established that the CVD grown WS_2 and WSe_2 on SiO_2/Si substrates exhibit n-type and p-type characteristics, respectively. Therefore, alloying these materials offers a pathway to control the carrier type and the transport properties. Recent work on 2D $WS_{2x}Se_{2(1–x)}$ alloys by Xidong Duan *et al*. shows that full composition of $WS_{2x}Se_{2(1–x)}$ nanosheets can be synthesized with tunable optical and electrical behaviors[64].

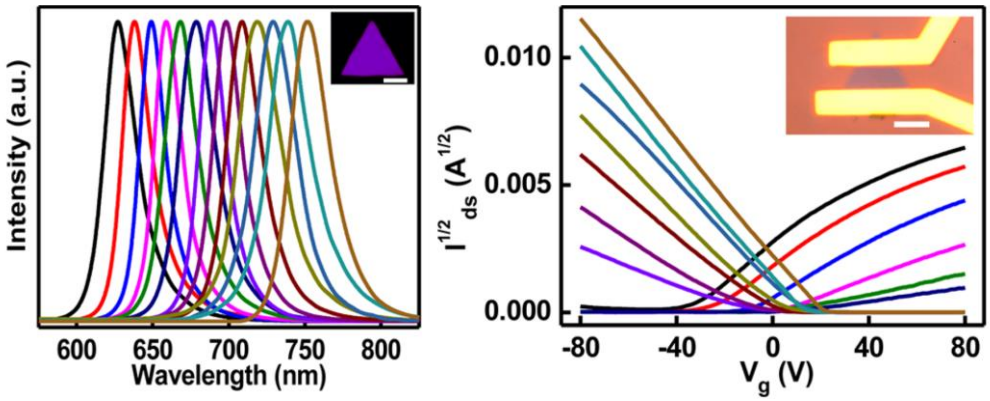

Figure 1.6 Photoluminescence spectra (left) and transfer characteristics (right) of a series of composition tunable $WS_{2x}Se_{2-2x}$ monolayer nanosheets. Figure adapted with permission from ref. [64]

In this work, continuous bandgap engineering was achieved and vibrational properties were discussed, which is similar to the work on $MoS_{2x}Se_{2(1-x)}$ that we will not review the details. Moreover, the composition modulation of electrical properties, such as conductivity, threshold voltage, carrier type, and mobility was investigated using back-gated field effect transistors (FETs) based on $WS_{2x}Se_{2(1-x)}$ alloys. For the sulfur rich alloys (~ 0.55 -1.0 S atomic ratio), the FETs display n-type semiconducting properties with a highest threshold voltage (V_t) of - 50 V observed in the nearly pure WSe_2 samples, and the amplitude of this negative threshold voltage decreases with increasing selenium fraction, indicating the drop in the amount of electron carriers. One the other hand, for the selenium-rich alloys, a p-type semiconducting behavior is observed and the highest threshold voltage reaches + 33 V in the nearly pure WSe_2 nanosheets, indicating relatively high hole concentration. It is also noteworthy that the n-type to p-type carrier transition takes place nearly in the middle of the composition range, where the carrier mobility minimum is noticed. In the sulfur-rich alloys, the electron mobility decreases

from 11.8 $cm^2 V^{-1} s^{-1}$ in nearly pure WS_2 to 0.9 $cm^2 V^{-1} s^{-1}$ before switching to a p-type semiconductor. In the selenium-rich alloys, the electron mobility decreases from 68.2 $cm^2 V^{-1} s^{-1}$ in nearly pure WSe_2 to 5.3 $cm^2 V^{-1} s^{-1}$ in the p-type limit. The relatively low mobility in the intermediate composition range is attributed to higher contact resistance due to low doping concentration and impurity scattering. Overall, the successful synthesis of 2D $WS_{2x}Se_{2(1-x)}$ alloys with tunable optical and electrical properties further expands the library of 2D materials and shield lights to the design of 2D electronics and optoelectronics.

1.3.3. Phase engineering in 2D alloys

Unlike graphene, 2D transition metal chalcogenides can stabilizes in different phases while keeping their 2D nature. For instance, $MoTe_2$ is stable in both hexagonal (2H) or monoclinic (1T') phases whereas WTe_2 crystallize only in 1T' phase in nature[72-73]. Large changes in the crystal structure naturally affect their electronic band structures and as a result, the 2H phases exhibit semiconducting behavior whereas the 1T' phase is metallic. The structural (2H) and electronic (semiconducting) phase of $MoTe_2$ can be effectively engineered by laser irradiation[74] or W substitution[75-77]. Recently, it has been experimentally demonstrated that these two phases can be controlled on demand through electrolyte gating[79] which introduces a large density of carriers into the 2D sheets thus increases the total formation energy of 2H-$MoTe_2$ compare with the values of 1T'-$MoTe_2$ to induce structural transformation. This effect heavily relies on identification of 2D material systems that exhibit formation (total) energies close enough to each other such that one phase can be destabilized over another to induce desired phase changes.Thus far,

most of these well-investigated 2D alloy systems retain their crystalline structure and phases independently from the composition values. Due to the smaller mismatch in lattice parameters and electronegativity, alloying the materials from the same phase are more feasible but in return, limits the band bowing parameter as well as bandgap tunability.

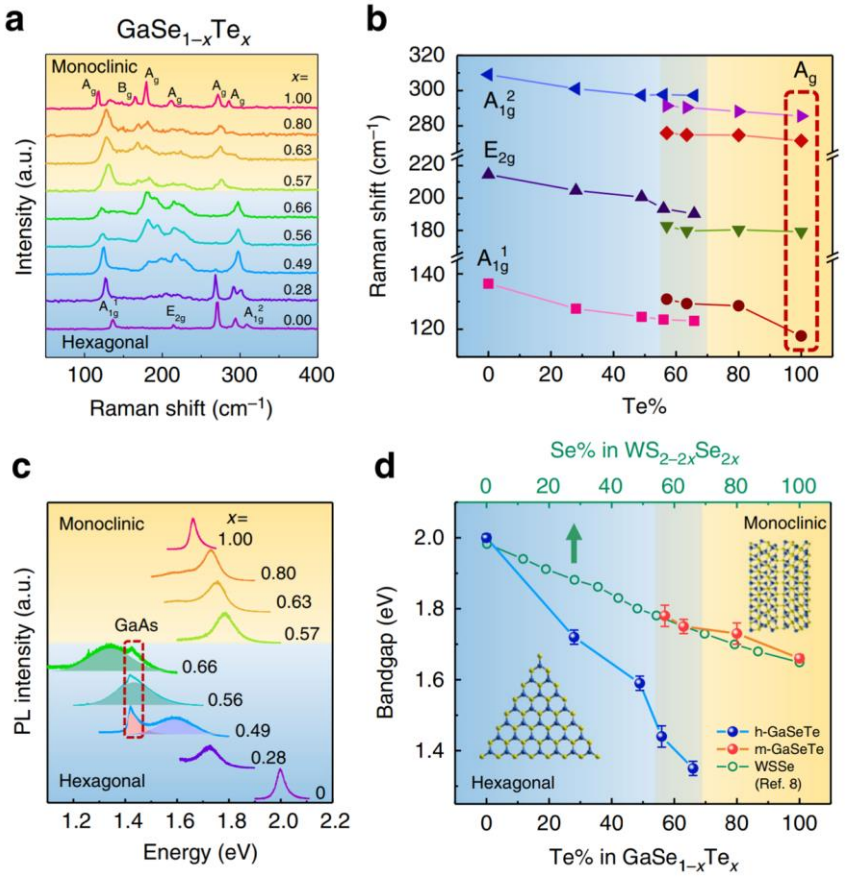

Figure 1.7 a. Raman spectra of $GaSe_{1-x}Te_x$ nanostructures at different compositions. Monoclinic and hexagonal structures are separated by different background colors. b Peak positions of different Raman modes as a function of Te content in $GaSe_{1-x}Te_x$.c. PL spectra of $GaSe_{1-x}Te_x$ nanostructures at different compositions. d Bandgap as a function of Te content in $GaSe_{1-x}Te_x$.Error bars indicate standard deviation of PL peak position measured from five or more points on the same sample. Figure adapted with permission from ref. [80]

Recent work by Hui Cai *et al*. reported the anomalous band bowing effect in the phase instability crossover region of $GaSe_{1-x}Te_x$ nanomaterials[80]. Specifically, gallium selenide (GaSe) crystallized in an isotropic hexagonal phase whereas gallium telluride (GaTe) stabilizes in an anisotropic monoclinic phase. Due to the huge difference in crystalline symmetry, traditional phase diagram of Ga-Se-Te suggested that alloying bulk crystals is forbidden in the full composition range under equilibrium conditions. However, author have successfully synthesized $GaSe_{1-x}Te_x$ nanomaterials across the entire range through the physical vapor deposition (PVD) method on GaAs (111) substrates, which stabilizes the metastable phase. More interestingly, at a magical range ($0.5 < x < 0.7$), the $GaSe_{1-x}Te_x$ alloy undergoes hexagonal to monoclinic phase crossover with a coexisting region and abnormal band bowing effects proved by angle resolved Raman & PL spectroscopy, HR-TEM, and optoelectrical measurements. The overall results provide valuable insight into tuning the optical and electrical properties of 2D materials through phase engineering and offer new opportunities for potential device application in photoelectronic.

Chapter 2 EXPERIMENTAL METHODS

2.1. Material growth

2.1.1. Chemical vapor transport (CVT)

Chemical Vapor Transport (CVT) has been widely applied as a bulk crystal synthesis method from their constituent elements. This method represents a serious of reactions that share one common feature: a condensed phase (solid) sublimates in presence of gaseous reactant and deposit elsewhere in form of crystals. A typical transition metal chalcogenide growth takes place in an evacuated (< 10^{-5} torr) and sealed ampule using elemental form of the metal and chalcogen as precursors (**Figure 2.1 a**). In the growth temperature, metal atoms escape from its surface, mix / react with chalcogen vapor, transport, and eventually crystallize at the other end of the ampule.

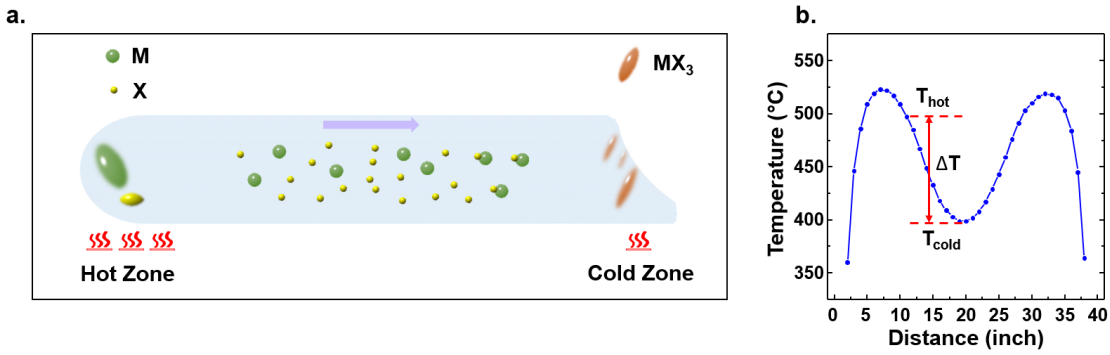

Figure 2.1 a. Schematic view of the CVT growth process for MX_3. b. The temperature profile of the furnace used for TiS_3 growth.

High-purity and large-yield single crystals of transition metal trichalcogenides[81], MX_3 (M = Ti, Zr, Hf, Ta and X=S, Se) and have been grown using these techniques. Typically, 1.0 – 2.0 g of the high purity precursors in stoichiometric ratio were sealed inside an evacuated quartz tube. A small amount (20-30 mg) of iodine (I_2) could be added as a

transport agent. As shown in **Figure 2.1 a**, the sealed ampule is then placed into a two-zone furnace with a temperature gradient, ΔT (**Figure 2.1 b**). The precursor side is placed at the hot zone (T_{hot}) and crystal growth takes place at the cold zone (T_{cold}). Since the CVT growth is typically an endothermic process, the heating rate was kept at 1 °C/min to avoid possible explosion. During the heating process, the precursors slowly turned into vapor phase and were transported to the cold zone as a result of the temperature gradient. After 5-7 days of heating, large crystals were found in the interior surface. Crystals grown through CVT technique are usually high in purity owing to the high purity of the precursor elements. **Table 2.1** shows the detailed growth conditions of the crystals.

Table 2.1 Growth conditions of selected crystals.

Crystal	T_{hot} (°C)	T_{cold} (°C)	Growth time (Days)	Transport agent
TiS_3	500	400	5	Not added
ZrS_3	700	600	5	I_2
HfS_3	650	550	5	I_2
TaS_3	650	550	7	I_2
$Nb_{(1-x)}Ti_xS_3$	550 – 520	450 - 420	7	Not added

2.1.2. Chemical vapor deposition (CVD)

Chemical vapor deposition (CVD) method has been used in semiconductor industry to produce thin films. Different from the physical vapor transport process which is a bulk crystal growth technique, the CVD process and is currently applied as an effective method to synthesize two-dimensional materials at large scales. In a CVD process, the

desired substrate is exposed to a carrier gas (usually inert gas such as N_2 or Ar) with one or more volatile precursors, which decompose and/or react on surface of the substrate to produce the desired film deposit. In general, the outcome of a CVD process is affected by a variety of parameters including temperature profile (growth temperature, heat and cooling rate), carrier gas flow rate, growth time, the amount of each precursor, and the distance between precursors and substrate. Despite the difference in the growth process of various materials, the common features of a general growth involve mass flux of precursors and the growth rate of films[82]. As the mass flux is high, it provides the pathway to grow large-scale continuous films with small domains at a low growth rate or large domains at high film growth rate. On the contrary, low mass flux offers the opportunity to synthesize discrete single domains of monolayers, and the growth rate controls the domain size of monolayer films: a low rate often leads to small domains whereas at high growth rate gives rise to large single domains.

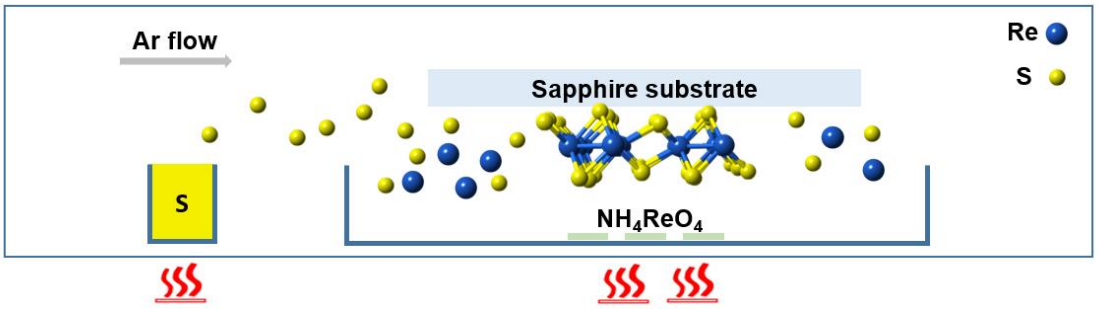

Figure 2.2 Schematic view of the CVD growth process for ReS_2.

In our work, hexagonal and truncated triangular rhenium disulfide (ReS_2) flakes have been synthesized on sapphire substrates under controlled conditions. Prior to growth, sapphire substrates were treated under oxygen plasma flow for 3 minutes in order to remove surface contaminants, and then placed at the top of alumina boat containing 10 -

50 mg of ammonium perrhenate (NH_4ReO_4, ⩾99.99%, Sigma Aldrich) precursor. As shown in **Figure 2.2**, ceramic boat was placed at the center of the heating zone of the furnace, and 1.0 grams of sulfur (S, ⩾99.998%, Sigma Aldrich) precursor was placed approximately 18.5 cm upstream from the boat. The sulfur precursor was then transported to the substrate under high purity argon flow. During the growth, the substrates were first heated to 300 °C under Argon flow of 100 sccm, which was gradually decreased to 10 - 50 sccm at the growth temperature (490-520 °C). The heating rate was kept at 30 °C/min. During the growth, the sulfur precursor firstly sublimated at 350 - 420 °C temperature range, and was carried to the substrate by Argon flow constantly. The growth was carried out at 490 - 520 °C for 20 - 30 minutes followed by a controlled cooling (5 °C min^{-1}) process to 420 °C and a fast cooling process (>10 °C min^{-1}) to room temperature. The flow rate of the Argon gas was kept 50 sccm during the whole cooling process.

2.2. Sample preparation

2.2.1. Mechanical exfoliation

After the isolation of graphene in 2004, the ‘scotch tape’ exfoliation method has become one of the most popular techniques to achieve high yield monolayer to few layers of 2D materials. In our work, this technique was extensively used. Prior to exfoliation, the sapphire or 285 nm SiO_2/Si substrate was treated under oxygen plasma flow for 2 minutes in order to remove surface contaminants. For exfoliation, a small flat piece of crystal was placed at the sticky side of a scotch tape, which was then folded and stuck to another sticky side of the tape. The crystal was then exfoliated onto another piece of tape. The process was repeated 4 to 6 times until the crystals appeared dull. Finally, the

exfoliated crystal was transferred onto the substrate by gently printing the tape onto the substrates.

2.2.2. TEM/STEM sample preparation

The quality of sample preparation is very critical in STEM/TEM measurement. In general, samples should be thinned down to electron transparency limit which is preferably less than 10 layers of atoms. CVD grown of mechanically exfoliated samples were transferred onto copper grids prior to measurements. Firstly, a copper grid was mounted on the wafer at the area of interest, and grid was immersed by a drop of PMMA (495, A4), with the solvent (anisole) removed by heating the substrate at 140 °C for 3 mins. Then, the copper grid with the wafer was immersed into KOH solution (2 mol/L) until the copper grid floats up. After rinsing by DI water, the PMMA film was removed by acetone, leaving the samples on the grid. Finally, the grid was washed by isopropanol alcohol (IPA) to removed acetone residues. Samples made from the wet transfer method typically contains amorphous organic residues, therefore a pre-baking process was usually preformed before electron microscopy measurements.

Alternatively, a PMMA-free wet transfer technique was also used to prepare TEM sample. A copper grid was first mounted on top of the area of interest, after a drop of IPA was applied and dried, and the grid stick to the surface of the substrate. Then the substrate was flipped over and immersed in KOH solution (2 mol/L) until the copper grid was detached from the substrate. Finally, the grid was rinsed by DI water and naturally dried. This PMMA-free route significantly reduces the contamination in the transfer process and is more widely used in our sample preparation.

2.2.3. Diamond Anvil Cell (DAC) preparation

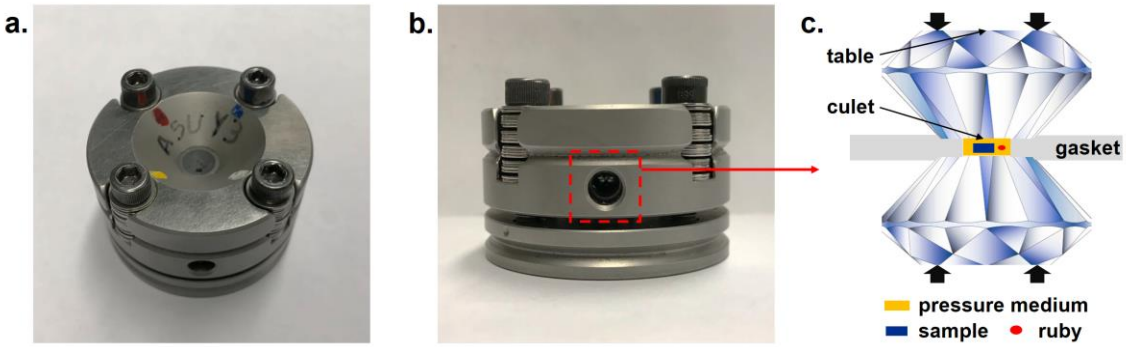

Figure 2.3 a. The top view and b. side view of the diamond anvil cell (DAC) used in this work. c. Schematic view of the working principle of the DAC.

The research at high pressure is dependent on techniques and a diamond anvil cell (DAC) is becoming a powerful device to offer ultra-high pressure. Despite the difference in the design / alignment of various DACs, the principle of a DAC is very simple. A specimen is placed in the sample chamber between the culets of two opposed diamonds, and the high pressure is generated when a force pushes the two diamonds together[83]. Depending on the design of a DAC, the pressure in the sample chamber can reach pressures over 300 gigapascal (GPa). The DAC used in our work was developed by Mao and Bell[84] at the Geophysical Laboratory. In this type of design, the force is generated by a spring-loaded lever-arm mechanism where the anvils are supported by tungsten carbide half cylinders. The DAC used in this work is shown in **Figure 2.3a** and **2.3b**, and the working principle of the cell is shown in **Figure 2.3c**. In general, gasket in a DAC apparatus is very critical since it not only prevents the two diamond anvils from touching each other but also paves the way to offer ultra-high pressure in the sample chamber[85]. In our experiment, a gasket made of stainless T301 was cut pre-indented to the designated

pressure, and a pinhole (~ 200 μm diameter) was drilled in the center of the culet of the gasket to create the sample chamber.

A pressure transmitting medium is another critical part of measurements in DACs. Such a medium is usually a soft and compressible material that fills the sample chamber and transmits pressure to the sample. Typical medium can be a gas (He, Ar, or N_2), liquid (4:1 methanol/ethanol), or solid (NaCl or CsI). In general, hydrostatic pressure is preferred in high pressure measurements since variation in the pressure (distortion) applied to a sample could cause different sample behaviors. In the high-pressure our studies on TiS_3, methanol/ethanol mixture was used to transmit the pressure whereas CsI was applied in the studies on *o*-TaS_3. The pressure measurement in a cell is offered by ruby fluorescence method which was first established in the 1970's[86]. It was found the fluorescence ruby (Cr-doped Al_2O_3) shifts with applied pressure, and in our measurement, a tiny piece (~ 20 μm) of ruby was excited by a 532-nm laser and the fluorescence peaks were recorded to estimate the pressure in the cell.

2.3. Characterization methods

2.3.1. X-ray diffraction

Crystals can be considered as highly ordered array of atoms, and X-rays forms waves of electromagnetic radiation with a wavelength that is comparable to atomic spacings. As the incoming X-ray interacts with atoms, it is scattered in a specular fashion. These spherical waves will be added constructively only when the path-length difference of the

X-ray equals integer multiples of the wavelength of the incoming X-ray, as shown in **Figure 2.4**. In this case, the constructive reflection takes place only as selected directions (θ) determined by Bragg's law: $2d\sin\theta = n\lambda$, where d is the lattice spacing, θ is the reflected angle, and λ is the wavelength of the X-ray.

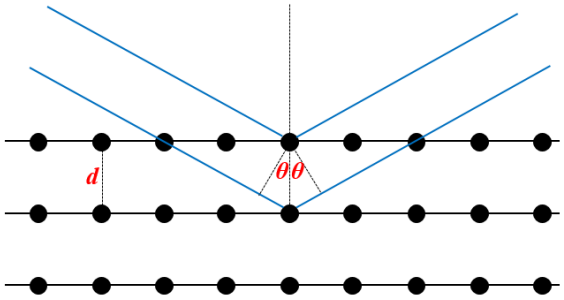

Figure 2.4 A general description of Bragg's law.

The crystallinity of the CVT grown samples was examined by powder X-ray diffraction (XRD) technique using Cu Kα irradiation (λ = 1.54 Å). The high-resolution X-ray diffractometer (PANalytical X'Pert Pro MRD) and the powder X-Ray diffractometer (Siemens D5000) in the LeRoy Eyring center for solid state science were used. Typically, a small piece of sample was mounted onto a zero-background plate and the 2θ angle is scanned from 5 to 65 degrees.

2.3.2. Atomic force microscopy (AFM)

Atomic force microscopy (AFM) is a high-resolution type of scanning probe microscopy (SPM) that pictures the interaction between the very sharp tip on a cantilever and the sample surface to produce nanometer scale images. The working principle of an AFM is not complex. As the cantilever approaches a specimen, the sharp tip is brought into proximity of the surface and oscillates due to the force between the tip and surface.

The deflection of the tip (displacement with respect to the equilibrium position) is recorded by a detector through the reflected laser beam focused on the tip. The optical signal is eventually converted into an electrical signal to generate the surface topography images. In addition to the fundamental of application of surface imaging, AFM and SPM techniques are extensively used in the research of 2D materials to investigate a wide range of properties such a conductivity, surface potential, and magnetic behaviors

Within the scope of this work, the AFM technique was applied primarily to achieve the topography information of our samples. The experiments were preformed using Dimension Multimode 8 AFM under a tapping mode. Depending on the size of the area of interest, the resolution was set from 256 × 256 to 512 × 512. Based on the morphology of the sample surface, the scanning rate was typically set to from 0.5 to 1.0 Hz.

2.3.3. Electron microscopy

Electron microscopy technique is an indispensable tool for studying the structure of materials. In this work, the scanning electron microscopy (SEM), transmission electron microscopy (TEM), and scanning transmission electron microscopy (STEM) have been used to understand the surface topography and atomic-level structure of our psedo-1D materials. The SEM measurements on TaS_3 and $Nb_{(1-x)}Ti_xS_3$ alloys were performed using Hitachi S4700 field emission SEM equipped with energy dispersive X-ray spectroscopy (EDS). The acceleration voltage was set to 15 kV, and working distance was typically 12 - 14 mm, respectively. The TEM images of TiS_3 nano ribbons were taken using JEOL 2010F TEM at a voltage of 100 kV. The high-resolution TEM and the diffraction patterns of $Nb_{(1-x)}Ti_xS_3$ alloys were achieved by a FEI Titan 80−300 TEM at 300 kV with a

spherical aberration corrector. Our STEM measurements and valence electron energy loss spectroscopy (EELS) of the CVD-grown ReS_2 were performed using Nion 100 STEM equipped with a high energy resolution monochromator and a modified Gatan Enfinium electron energy loss spectrometer. The accelerating voltage was typically set to 80 kV, and the probe size was about 0.3 nm with a probe current of approximately 12 pA.

2.3.4. Raman spectroscopy

Raman spectroscopy has been widely applied to understand the lattice vibrational properties of layered material systems. The general description of Raman effect has been established for a long time. As the incident phonon interacts with the matter, the phonon can be scattered either elastically (also called Rayleigh scattering) or inelastically. In an inelastic scattering process, the scattered phonon can either lose energy (Stokes scattering) or gain energy (anti-Stokes scattering). Raman technique relies on the inelastic scattering process and typically measures the phonon scatter in a Stokes scattering process. Specifically, as phonon of a wavelength of λ_0 interacts with the lattice vibration of a specimen, the incident photon loses its energy and red shifts to a higher wavelength of λ_1. The Raman shift ($\Delta\omega$) is described as the change in frequency (wavenumber) of the incident photon (ω_0) with respect to the scattered photon (ω_1):

$$\Delta\omega = \omega_0 - \omega_1 = \frac{1}{\lambda_0} - \frac{1}{\lambda_1}$$

As earlier mentioned, Raman offers the opportunity to understand the vibrational properties of materials. However, not all vibrational modes are Raman active. Raman spectroscopy only measures those vibrations with a non-zero change in polarizability

induced by the electric field (***E***) of the incident light. The strength of the dipole moment (***P***) can be described as:

$$\boldsymbol{P} = \alpha\, \boldsymbol{E}$$

Here, the α represents polarizability of a vibration mode, and it can be written as:

$$\alpha = \alpha_0 + \frac{\partial \alpha}{\partial Q} \cos(\omega_v t),$$

where the α_0 is polarizability of the molecular mode at equilibrium position, $\frac{\partial \alpha}{\partial Q}$ is the change of polarizability with respect to physical displacement caused by the vibrational motion. The $\cos(\omega_v t)$ represents oscillating of the lattice vibration with a frequency of ω_v.

The electric field (***E***) can be described as:

$$\boldsymbol{E} = \boldsymbol{E}_0 \cos(\omega_0 t),$$

where ω_0 is the frequency of the incident light.

Therefore, the dipole moment (***P***) can be rewritten as:

$$\boldsymbol{P} = \alpha\, \boldsymbol{E} = \alpha_0 \boldsymbol{E}_0 \cos(\omega_0 t) + \frac{\partial \alpha}{\partial Q}\, \boldsymbol{E}_0 \cos(\omega_0 t) \cos(\omega_v t)$$

$$= \alpha_0 \boldsymbol{E}_0 \cos(\omega_0 t) + \frac{\partial \alpha}{\partial Q}\, \frac{E_0}{2} [\cos(\omega_0 + \omega_v) t + \cos(\omega_0 - \omega_v) t]$$

Here, the $\alpha_0 \boldsymbol{E}_0 \cos(\omega_0 t)$ term represents elastic scattering where the frequency (ω_0) of scattered phonon remains unchanged. In contrast, the second term $\frac{\partial \alpha}{\partial Q}\, \frac{E_0}{2} [\cos(\omega_0 + \omega_v) t + \cos(\omega_0 - \omega_v) t]$ represents the inelastic scattering process that is related to Raman effect. Therefore, for a vibration mode to be Raman active, the change in polarizability term $\frac{\partial \alpha}{\partial Q}$ should be non-zero.

The polarizability change of a vibration mode can be expressed by Raman tensor.[87] which is a 3 × 3 matrix decided by the symmetry of a vibration mode and the crystal structure of the materials. Raman tensors can be found in the standard textbooks and review articles. Besides, the configuration of the incoming light ($\boldsymbol{e}_i$) and scattered light ($\boldsymbol{e}_s$) is critical to Raman response. Typically, Raman measurements are taken under either parallel configuration where $\boldsymbol{e}_i$ and $\boldsymbol{e}_s$ are parallelly aligned ($\boldsymbol{e}_i \parallel \boldsymbol{e}_s$), or a cross configuration where the $\boldsymbol{e}_i$ and $\boldsymbol{e}_s$ are perpendicular to each other ($\boldsymbol{e}_i \perp \boldsymbol{e}_s$). In this work, the $\boldsymbol{e}_i$ and $\boldsymbol{e}_s$ are also referred as excitation ($\boldsymbol{E}$) and detection ($\boldsymbol{D}$).

The overall Raman intensity (I) is determined by the Raman tensor ($\boldsymbol{R}$) and the polarization vector of the incoming light and scattered light.

$$I = \left| {}^{t}\boldsymbol{e_s} \boldsymbol{R} \boldsymbol{e_i} \right|^2$$

As discussed in the section 2.1, the material properties of pseudo-1D materials is anisotropic, thus the vibrational nature / Raman intensity of these class of materials shows angle dependent variation as the E-field of incoming phonon rotates with the primary axis of the crystal. In the backscattering geometry with a parallel configuration ($\boldsymbol{e}_i \parallel \boldsymbol{e}_s$), the propagating direction is z, and we define the incoming light ($\boldsymbol{e_i}$) is polarized at an angle θ measured from the x-axis

$$\boldsymbol{e}_i = \begin{pmatrix} cos\theta \\ sin\theta \\ 0 \end{pmatrix} \text{ and } \boldsymbol{e_s} = \begin{pmatrix} cos\theta \\ sin\theta \\ 0 \end{pmatrix}$$

Next, we show the angle-dependent Raman intensity of the A_g mode of GeAs[88] by Shengxue Yang *et al*. as an example.

For the Raman active A_g mode in GeAs, the Raman tensor is

$$R = \begin{pmatrix} a \cdot e^{i\phi_a} & & d \cdot e^{i\phi_d} \\ & b \cdot e^{i\phi_b} & \\ d \cdot e^{i\phi_d} & & c \cdot e^{i\phi_c} \end{pmatrix}$$

The measurements were taken under a backscattered geometry, in a parallel or cross configuration, the Raman intensity of the A_g mode are:

$$I^{para}(A_g) \propto \left[(\cos^2(\theta) + \frac{a}{b} \cdot \sin^2(\theta) \cdot \cos(\phi_{ab})\right]^2 + \cdot \sin^2(\theta) \cdot \sin^2(\phi_{ab})$$

$$I^{cross}(A_g) \propto \left\{\left[\cos(\phi_{ab}) - \frac{a}{b}\right]^2 + \sin^2(\phi_{ab})\right\}^2 \cdot \sin^2(\theta) \cdot \cos^2(\theta)$$

Here, the term ϕ_{ab} is the phase difference of *a* and *b* values in the Raman tensor. Based on the intensity calculation results, the possible patterns of the polar plots for the angle-dependent Raman intensities of the A_g mode is shown in **Figure 2.5**. Interestingly, the polar plots of the A_g mode under these two configurations can be totally different. Depending on the phase difference and the ratio of the *a* and *b* values in the Raman tensor, the A_g mode can show five types of patterns in the parallel configuration. In contrast, under a cross configuration, simulation results show a four-leaf pattern, and experimental results show two lobed features with a secondary maximum.

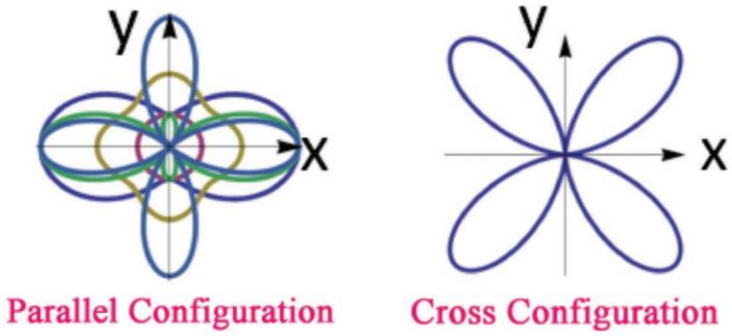

Figure 2.5 Possible patterns of the polar plots for the angle-dependent Raman intensities of the A_g mode under parallel and cross configuration. Figure adapted with permission from ref. [44]

In our work, Raman measurements were performed in two systems. Our commercial Renishaw InVia Raman microscope is equipped with both UV (λ = 325 nm) and green (λ = 488 nm) laser as the excitation source. In this system, an objective lens of 50× (NA = 0.95) was used to take data and the laser power was set as 0.1 to 2.0 mW. Angle-dependent measurements were carried out by rotating the sample stage. The other Raman system used in our work was a home-built system equipped with green laser (λ = 532 nm), red laser (λ = 633 nm), and IR laser (λ = 785 nm). In this system, a half-wave plate was incorporated in to change the polarization direction of incident laser for angle-dependent studies. In the measurement, samples were placed under long working distance 50x optical lens (NA = 0.42) using green laser (λ=532 nm) as radiation source with a power of 0.5 - 1.3 mW. The data were collected using an Acton 300i spectrograph with a back thinned Princeton Instruments liquid nitrogen cooled CCD detector or an Andor 750 spectrometer combined with an iDus back thinned CCD detector.

2.4. Density function theory (DFT) calculations

2.4.1. Phonon dispersion calculation of TiS_3

The first-principles calculations were carried out in the framework of DFT as implemented in the Vienna *Ab Initio* Simulation package[89-90] (VASP). Generalized gradient approximation (GGA) of Perdew-Burke-Ernzerhof was employed for the exchange and correlation potentials[91]. A 10 × 15 × 5 Γ-centered **k**-point mesh was used for the Brillouin zone integration for the primitive unit cell of bulk TiS_3. Frozen-core projector-augmented wave potentials were used with 500 eV kinetic energy cutoff for the plane-wave[92-93] expansion. The convergence criterion for energy is set to 10^{-5} eV between

two consecutive steps in the self-consistent field calculations. The atomic positions were relaxed until the Hellmann-Feynman forces are less than 10^{-4} eV $Å^{-1}$. We used the DFT-D2 method of Grimme as implemented in VASP in order to describe the vdW interaction between TiS_3 layers correctly. The vibrational spectrum of the systems was investigated via ab initio phonon calculations. These were performed in the harmonic approximation by making use of the small displacement method implemented in the PHON code[94].

2.4.2. Formation energy calculation of $Nb_{(1-x)}Ti_xS_3$ alloy system

The Vienna *Ab initio* Simulation Package (VASP, version 5.4.4)[95] was used to perform density functional theory calculations. To model the triclinic and monoclinic structures of $Nb_{(1-x)}Ti_xS_3$ with different compositions x ranging from 0 to 1 at an incremental step of 1/8, we used $2 \times 2 \times 1$ and $2 \times 2 \times 2$ supercells, respectively. We created the supercell structures based on the Special Quasirandom Structures (SQS) method[96] as implemented in the ATAT package. Each supercell therefore consists of 64 atoms.[97] In all of the VASP calculations, we used the Perdew-Burke-Ernzerhof functional[98] and potentials from the projector augmented-wave method.[99-100] We used a cutoff energy of 600 eV for the plane wave basis sets and the *k*-point sampling grids for the supercells were $8 \times 6 \times 9$ and $8 \times 12 \times 5$ for the triclinic and monoclinic supercells, respectively. The formation energy E_f of $Nb_{(1-x)}Ti_xS_3$ was calculated as $E_f = (E_{Nb(1-x)TixS3} - (1-x)\,E_{Nb} - xE_{Ti} - 3E_S)/4$, where $E_{Nb(1-x)TixS3}$ denotes the energy per formula unit of a $Nb_{(1-x)}Ti_xS_3$ supercell. E_{Nb}, E_{Ti}, and E_S are the energies of Nb, Ti, and S atoms in their bulk unit cells with 2, 2, and 32 atoms, respectively. To simulate the *p*-type doping effects on

the energetics of NbS_3, we remove the same number density of electrons from the triclinic and monoclinic unit cells.

Chapter 3 DOMAIN ARCHITECTURES AND GRAIN BOUNDARIES IN HIGHLY ANISOTROPIC RHENIUM DISULFIDE

This chapter shows the successful growth of ReS_2 flakes of hexagonal and triangle shape with well-defined crystalline using CVD method. Results have established Re-chain orientation and domain architecture within ReS_2 flakes, and provided the first atomic resolution insight into ReS_2 grain boundaries. We find that cluster and vacancy defects are formed by collusion of Re-chains at the GBs, and surprisingly these defects dramatically impact the crystal structure by changing the Re-chain directions, thus alternating the overall in-plane anisotropy. Overall results shed light on domain structure of anisotropic 2D ReS_2, anticipated to allow researchers to attain much desired crystalline anisotropy in CVD grown ReS_2 for tangible applications in photonics and optoelectronics where linearly polarized material properties are required.

3.1. Crystal structure of rhenium disulfide (ReS_2)

The unit cell of rhenium disulfide (ReS_2) contains four rhenium atoms and eight sulfur atoms, and ReS_2 monolayers exhibit a distorted 1T structure (**Figure 3.1a**). Due to the extra valence electron shared by neighboring Re atoms, ReS_2 contains both Re-S and Re-Re bonds. As a result, the Re atoms form unique chain structure along the *b*-axis (**Figure 3.1b)** due to strong interaction and dimerization between the adjacent Re atoms. The reduced distorted 1T structure, together with the rhenium chains, are responsible for the strong in-plane anisotropy, leading to many attractive properties of ReS_2.

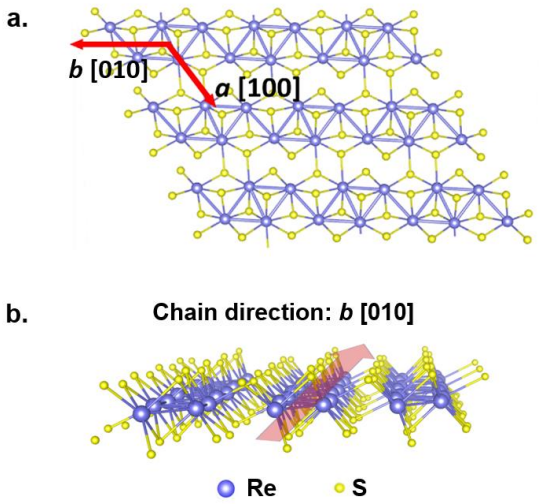

Figure 3.1 a. Atomic configuration of ReS_2 monolayer in distorted 1T structure. b. Re chain structures along the *b*-axis.

3.2. Growth dynamics

Developing controllable growth techniques to achieve highly crystalline ReS_2 monolayers with well-defined domain structure is critical to explore its attractive properties. To achieve this goal, the growth substrate needs to provide low-enough energy barrier for nucleation. Here, pre-cleaned double polished c-cut sapphire wafers have been chosen. In a typical CVD process, sulfur and ammonium perrhenate (NH_4ReO_4) precursors are transported to sapphire wafers at controlled temperatures (490 - 520 °C), flow-rates (10 - 50 sccm), and NH_4ReO_4 amount (10 - 50 mg). The NH_4ReO_4 decomposes prior to the growth, forming highly volatile Re_2O_7 and ReO_2 rhenium oxide complex, which then proceed oxide sulfurization reaction to yield ReS_2. Based on this principle, after formation of intermediate rhenium oxide complexes and physically adsorbed on the surface, the rhenium oxide complex diffuses on the substrate till losing

the kinetic energy. Once sulfurized, ReS_2 is nucleated at random locations, initiating one of the common 2D growth modes (layer by layer, dendritic, or screw-dislocation driven).

In our studies, we find that the growth temperature, initial loading amount of NH_4ReO_4 and overall flow rate make largely changes in overall coverage and domain structure of ReS_2 layers. Firstly, increasing the NH_4ReO_4 precursor amount under same temperature and flow rate results in much smaller domain sizes and higher nucleation densities. This implies that the intermediate rhenium oxide complex controls the nucleation density and large-area growth. Secondly, high flow rate of carrier gas may improve the mass transfer and increase in the crystal growth rate. In this case, atoms do not have enough time to move into the right lattice locations, where crystal domains could have the lowest surface free energy, and defect density increases under high flow rate. Therefore, the ReS_2 crystals are more likely to grow under kinetics condition, which results in the formation of dendritic morphologies rather than the thermodynamic ones. Overall, the hexagonal ReS_2 monolayers are synthesized at reduced temperature (490 °C), NH_4ReO_4 precursor amount, and flow-rate conditions, whereas triangular features are observed at slightly higher temperatures (520 °C).

3.3. Domain structures of ReS_2 monolayers

After the CVD growth, a variety of highly crystalline ReS_2 monolayers with different domain shapes, including separated truncated ReS_2 triangles (**Figure 3.2a**), relatively large area separated (**Figure 3.2b**) or nearly merged (**Figure 3.2c**) hexagonal ReS_2 domains, and fully merged ReS_2 monolayers (**Figure 3.2d**), were observed. The truncated triangle-like shape monolayers were grown at higher temperatures (500 -

520 °C) in relatively broad flow rates of 12 to 50 sccm, and the hexagonal features were achieved at lower temperature (490 °C) and low flow-rates (12-15 sccm). The small nano-dot feature in the middle of each ReS_2 domain is identified as a nucleation center.

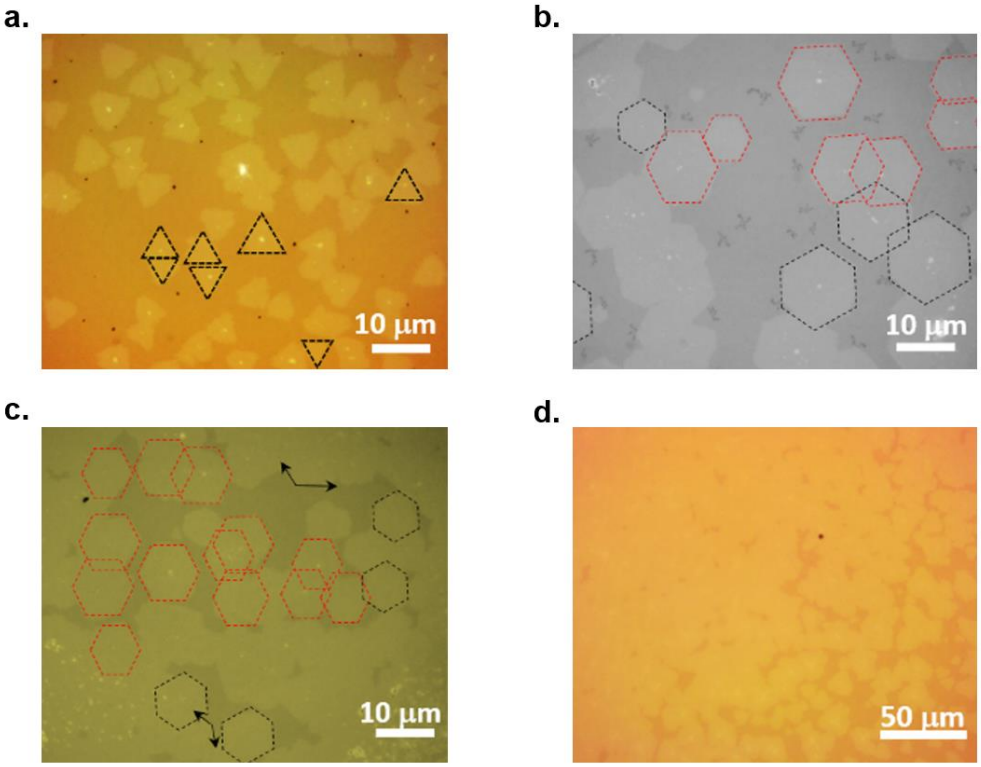

Figure 3.2 a. Separated truncated ReS_2 triangles. b. Relatively large and separated ReS_2 hexagons in two distinct directions (red and black dashed lines). c. Well aligned and nearly coalesced ReS_2 hexagons. e. Full merged ReS_2 monolayers.

During the growth, the nucleation sites, once formed, continue to grow and form grain boundaries when two or more domains meet, leading to a partially continuous film. The largest continuous monolayer ReS_2 film measures nearly a centimeter in size. The hexagonal ReS_2 domains, however, favorably orient themselves in two distinct geometries on the substrate (red and black hexagons in **Figure 3.2b-c**), which is in large contrast to ReS_2 growth on amorphous SiO_2 know to yield randomly oriented ReS_2

domains. It is also noteworthy to highlight that ReS_2 monolayers are more likely to form close to the step edges of the sapphire subtract compared to center area of the substrate. This is in line with previous theoretical and experimental studies showing a substantial reduction in the energy barrier of nucleation close to the step edges. Therefore, we conclude that similar catalytic processes are also involved in nucleation and diffusion of ReS_2 monolayer growth on sapphire wafers, which lead to preferentially oriented monolayer hexagons.

3.4. Characterization of ReS_2 monolayers

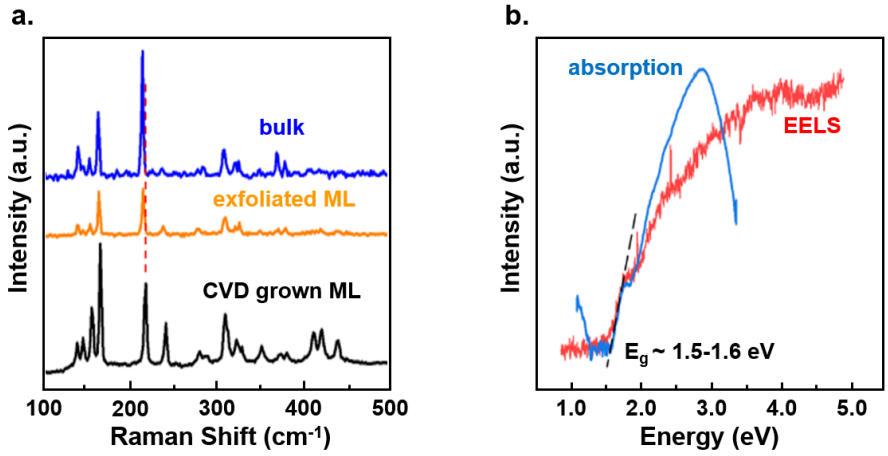

Figure 3.3 a. Raman spectra on bulk, exfoliated monolayer, and CVD grown ReS_2. b. Electron energy loss spectroscopy (EELS) and absorption spectroscopy acquired from monolayer ReS_2.

Single spot Raman spectroscopy, micro-absorption, nano electron energy electron loss (EELS), and atomic force microscopy (AFM) measurements were taken to characterize CVD grown ReS_2 monolayers. A comparison of Raman spectroscopy measurements on bulk and exfoliated ReS_2 with CVD grown sample (**Figure 3.3a**)

further confirms the presence of monolayer ReS_2, and unintentional defect density is so low that FWHM values are in the 4-6 cm^{-1} range. EELS and micro-absorption spectroscopy data in **Figure 3.3b** demonstrate a 1.5 - 1.6 eV bandgap value of monolayer ReS_2.

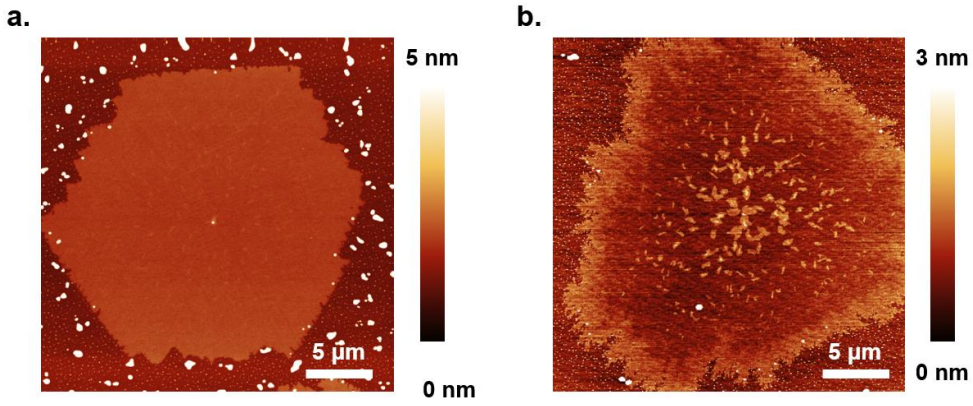

Figure 3.4 Atomic force microscopy (AFM) taken from a. hexagonal ReS_2, and b. truncated ReS_2 triangles.

Representative AFM images on hexagonal (**Figure 3.4a**) and truncated triangle (**Figure 3.4b**) ReS_2 domains display dendritic like growth at the edges that do not appear to be atomically sharp, suggesting that the monolayer flakes, either hexagons and truncated triangles, might be grown in dendritic form. Due to the randomly oriented dendritic features, the CVD grown ReS_2 may lack a structural anisotropy within each domain and may compromise its overall anisotropy properties. However, we find that structural anisotropy is surprisingly retained within each single domain.

3.5. Anisotropic properties in ReS_2 domain structures

Due to lower symmetry of the lattice, ReS_2 presents more Raman modes compared to other 2D systems such as MoS_2. As shown in **Figure 3.3a**, a series of Raman modes

appear between 100 - 400 cm^{-1}. These peaks are mostly associated with in-plane (E_{2g}) and out-of-plane (A_g) vibrations. Here, the Raman peak located at 214 cm^{-1} is noteworthy to discuss since recent studies have shown that the intensity of this mode reaches its maximum when incident laser polarization is nearly parallel to the *b*-axis. The intensity of this peak measured by angle resolved Raman spectroscopy yields 2-lobed plot that can be fitted into a $\cos^2(x)$ function. Therefore, the Raman intensity maximum direction of this mode at 214 cm^{-1} allows us to determine the *b*-axis orientation inside each ReS_2 domain.

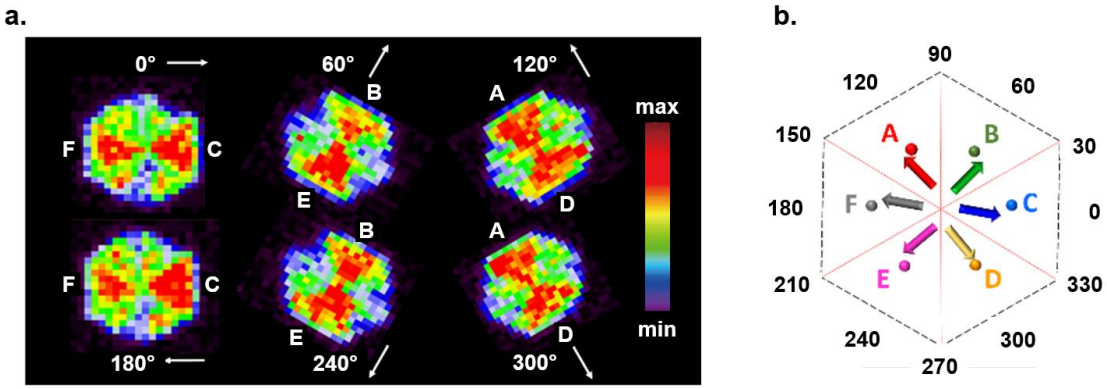

Figure 3.5 a. Angle-resolved Raman (AR-Raman) intensity mapping of the 214 cm^{-1} mode. b. Grain boundary structure and Re-chain direction in each sub-domain.

To understand the domain structure of ReS_2 monolayers and identify Re-chain direction, angle-resolved Raman mapping of the hexagonal ReS_2 domain has been performed and the intensity of the 214 cm^{-1} mode in a 360° circle is shown in **Figure 3.5a**. Successive Raman mapping images demonstrate that different segments (sub-domains) in the ReS_2 hexagon yield at least one order of magnitude in signal intensity compared to other segments. More interestingly, each individual segment displays triangular shape, and six different domains can be clearly identified. Despite the presence

of dendritic edges, this finding convincingly demonstrates that the hexagonal flake is not made of randomly oriented Re-Re chains, but instead is made of six triangle sub-domains, which appear to have grain boundaries roughly aligned at 30° to 210°, 90° to 270°, and 150° to 330°, as shown in **Figure 3.5b**. A closer look at **Figure 3.5a** shows that the equally bright triangles are located 180° across from each other, suggesting that Re-chains parallel to each other in such located sub-domains.

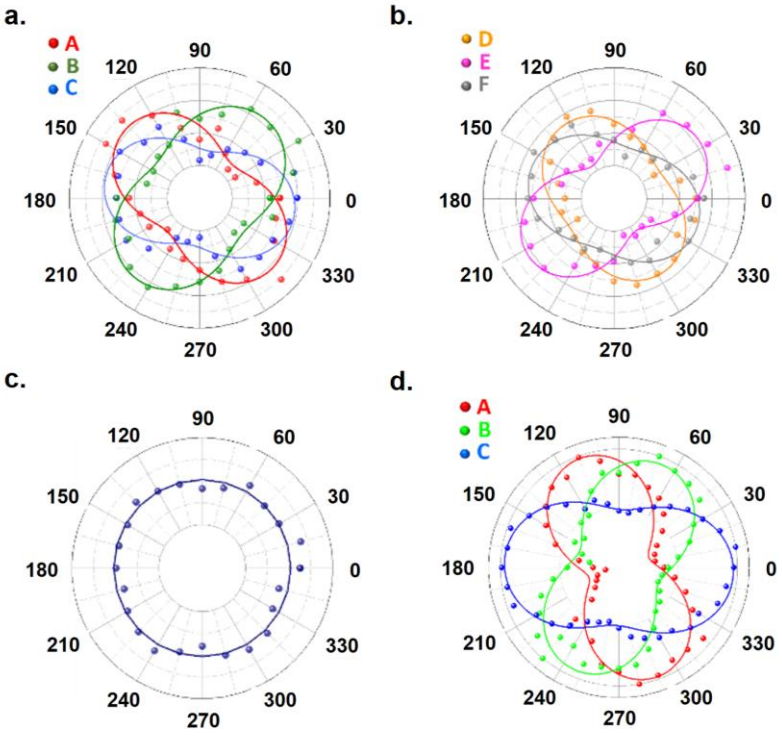

Figure 3.6 Single spot angle-resolved Raman intensity of the 214 cm^{-1} mode taken on a. sub-domain A, B, and C; b. sub-domain D, E, and F; c. the center of the hexagonal domain. d. Angle dependent reflectivity taken on sub-domain A, B, and C, at T= 4K.

To determine domain structure and the *b*-axis direction, angle-resolved Raman measurements have been taken on various spots within each triangular domain (domain A, B, C, D, E, and F in **Figure 3.5b**). As shown in **Figure 3.6a and 3.6b**, in each sub-domain, the 214 cm^{-1} peak intensity as a function of angle yield two-lobed polar plot and

the orientation of *b*-axis with respect to laboratory axes can be identified by fitting to $y = A+B\times cos^2(\alpha+\alpha_0)$. Results show that Raman intensity of the 214 cm^{-1} mode in domain A, B, C, D, E, and F reaches its maximum at 136^0, 50^0, 348^0, 303^0, 214^0, and 160^0 degrees, respectively. These results illustrate that sub-domain has the well-defined structural anisotropy. The offset of 10° between these values and the *b*-axis, mentioned in previous work, can be calibrated. Therefore, the *b*-axis in domain A, B, D, and E are nearly parallel to the grain boundary, whereas *b*-axis in domain C and F are perpendicular to the edge of the hexagonal ReS_2 flake. The proposed domain structure with Re-chain direction (the arrows) is depicted in **Figure 3.5b**. Besides, it is also noteworthy to highlight that the opposite triangular domains (A-D, B-E, and C-F) have the nearly similar *b*-axis orientation with a 180° rotation, which further proves that the Re-chains are nearly parallel to each other opposite sub-domains as discussed in previous paragraph. Similar angle-resolved Raman measurements were also taken on the whole hexagon flake domain using lower magnification yielding larger area probing spot. Surprisingly, the anisotropic response (two-lobed feature) has disappeared, suggesting that a single hexagonal ReS_2 monolayer flake behaves as if isotropic MoS_2 at macroscale by averaging the response over all sub-domains with different Re-chain orientation. We have performed single spot angle dependent reflectivity measurements on sub-domain A, B, and C to at 4K confirm the proposed Re-chain. The reflectivity is preferred over photoluminescence (PL) since the former probes the intrinsic properties of measured material and is less sensitive to defects which badly affects PL measurements. Comparison between **Figure 3.6d** and **3.6a** shows that the two-lobed feature of the angle-resolved reflectivity and Raman

measurements match closely with each other, offering an alternative method to identify Re-chain direction in synthesized ReS_2 layers.

In contrast, the domain structure of truncated triangular ReS_2 may be depicted in the two possible arrangements as constructed by red and blue lines in **Figure 3.7a**. In order to determine the domain architecture and Re chain directions in the triangular flake, we have performed similar angle-resolved Raman measurements on spot A to E. As shown in **Figure 3.7b**, Raman measurements taken at spot A, B, and C display two-lobed anisotropic features. Fitting the data points into $\cos^2(x)$ function reveals that the Re chains are aligned along 90°, 330°, and 210°, respectively, as marked by the arrows. The measurements taken at spot D, E, and F (**Figure 3.7c**), however, show nearly isotropic characteristic, implying that Re-chains are randomly oriented at those spots either because crystalline anisotropy is counteracted due to different *b*-axis orientation at the grain boundaries, or the defects at the boundaries strongly shifts Re chain direction (as discussed in section 3.6).

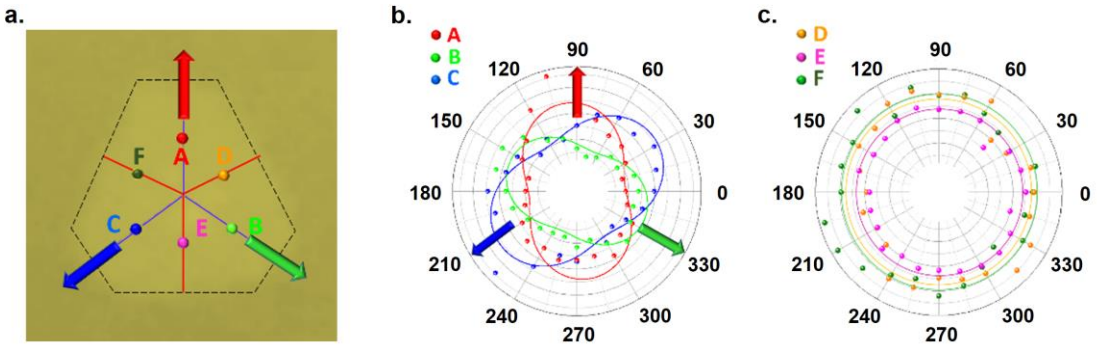

Figure 3.7 a. Construction of domain structure and chain directions of a truncated triangle ReS_2 flake. Angle-resolved Raman intensity of the 214 cm^{-1} mode taken at b. inside the domains (spot A, B, and C) and c. grain boundaries (D, E, and F).

To summarize, the grain boundaries in the truncated triangular domains can be defined by the red lines, and the Re chain within each sub-domain run parallel to the blue lines. Overall results suggest that our advanced CVD growth techniques will further expand the device applications that requires anisotropic structural, optical, and electronic response at chip scales.

3.6. Grain boundaries and defects behaviors

The grain boundaries of isotropic 2D materials have been well investigated and established. Previous studies have shown that grain boundaries in graphene consist of dislocation arrays that are mainly formed by 5-7 carbon rings, and that variety of different kinds of carbon arrangements mediated by carbon vacancies (V_C). The grain boundaries of h-BN and MoS_2, contain similar vacancies or sulfur substituted 4|6, 4|8, 5|7, and 6|8 rings. The grain boundary structure of ReS_2, however, is anticipated to be vastly different from other isotropic 2D systems due to anisotropy in interfacial energy and vast number of different atomic arrangements around defect sites. However, little to none is known about the detailed grain boundary structures in anisotropic 2D systems such ReS_2.

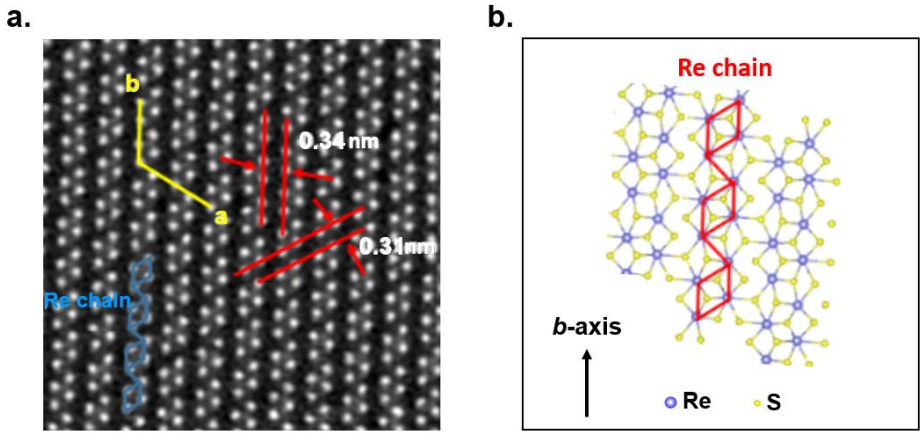

Figure 3.8 a. High resolution scanning transmission electron microscopy (HR-STEM) images taken from monolayer ReS_2. b. Schematic depiction of ReS_2 monolayers.

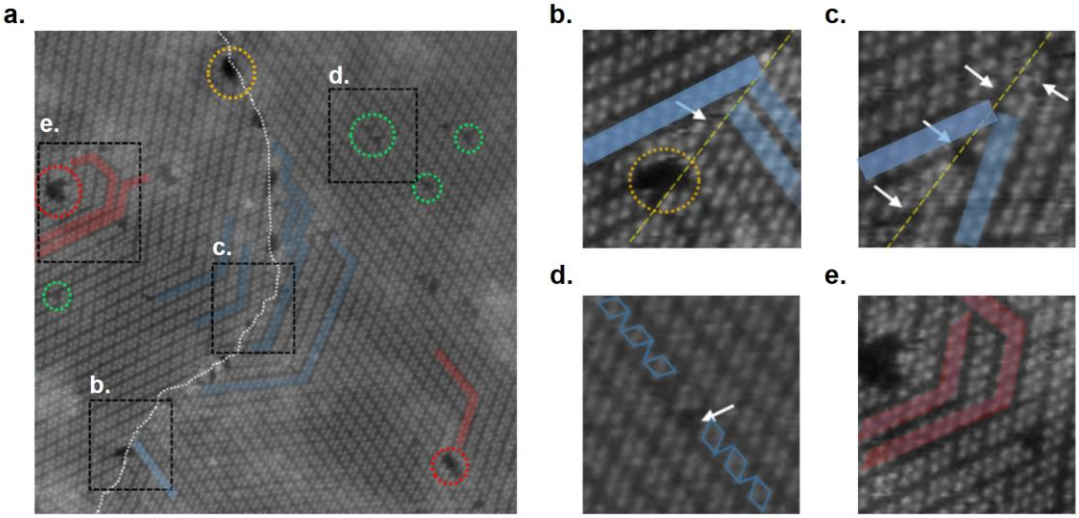

Figure 3.9 a. HR-STEM image taken at ReS_2 grain boundaries (white dash line) and specific zoom in images from b-c. grain boundary region, and d-e away from the grain boundaries.

High resolution scanning transmission electron microscopy (HR-STEM) has been performed to investigate the lattice structure of ReS_2 monolayers atomic level. The HR-STEM image taken from defect-free region in **Figure 3.8a** shows the quasi-1D nature and the Re chains in synthesized monolayers that match the schematic view in **Figure 3.8b.**

The HRSTEM image at grain boundary (**Figure 3.9a** white dash lines) region further visualize the defects behaviors. Since a large number of defects are present in close proximity to the grain boundary, *b*-axis changes its directions in this area, as highlighted by blue strips. The magnified images (**Figure 3.9b and 3.9c**) at the grain boundary clearly show the cluster and vacancy defects causes two Re chains approaching at different angles. Structural imperfections also exist away from the boundary region. The green dashed circles in **Figure 3.9a** highlight commonly observed S-Re-S pair vacancies which change atomic level local interactions sufficiently enough, leading to 180^{o} in-plane Re chain rotation by Re slipping motion as shown in **Figure 3.9d**. Interestingly, atomic structure around cluster defects (red dashed circles in **Figure 3.9a**) heavily influences Re chain directions. The highlighted red strips in **Figure 3.9e** demonstrates that the Re chains do not extend along infinitely but instead change their directions in multiples of 60° around the cluster defects. These observed defect behaviors, either close to or away from the grain boundaries, are significantly different from isotropic 2D systems, such as graphene and MoS_2, providing valuable insight into atomic level structure information of the CVD grown ReS_2.

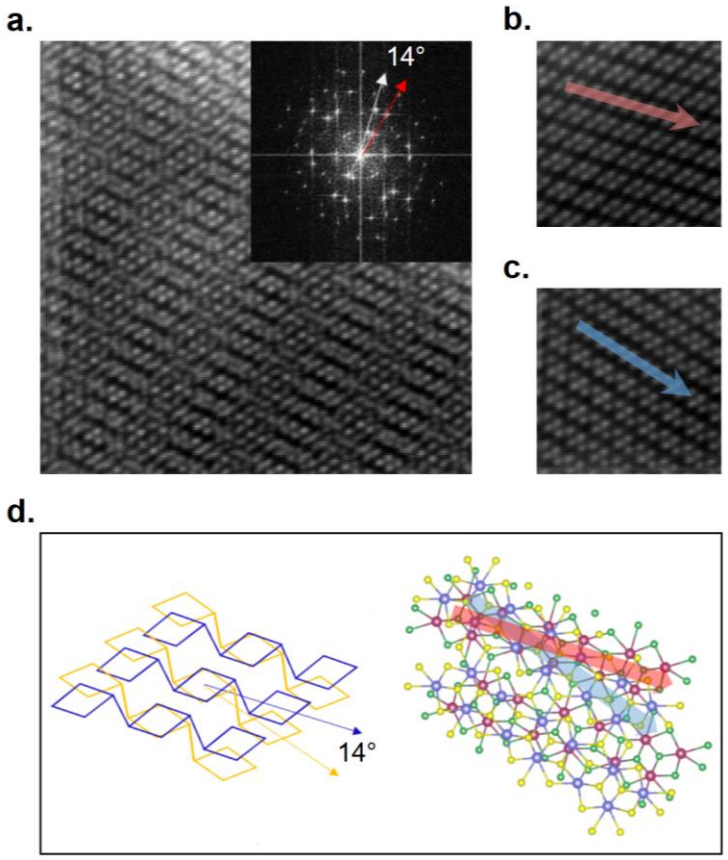

Figure 3.10 a. HRSTEM image and selected area electron diffraction (SAED) pattern collected from ReS_2 bilayers showing 14° rotation angle between adjacent layers. b. and c. Constructed images of each individual layer. d. Schematic depiction of the vertically stacked ReS_2 bilayers.

Even though CVD growth mostly yields monolayer ReS_2 domains, bilayer ReS_2 can be achieved when monolayers continue to grow on top of each other. The HR-STEM image (**Figure 3.10a**) taken from bilayer ReS_2 exhibits moiré fringes, and the diffraction pattern (**Figure 3.10a** inset) further reveals that each ReS_2 monolayer is rotated by 14° with respect to each other as illustrated in **Figure 3.10d**. The fast Fourier transform analysis in **Figure 3.10b and 3.10c** shows the chain direction of the two ReS_2 monolayers and their superposition of lattice that produces moiré fringes. Therefore, the bilayer ReS_2 domains

consist of monolayers stacking onto each other rotationally instead of vertically stacking of Re chains.

3.7. Local defects and anisotropy

Our angle resolved Raman mapping and reflectivity measurements have showed the presence of ReS_2 sub-domains with well-defined *b*-axis and associated polarization dependent optical response. Even though the structural and optical anisotropy can be achieved within sub-domains that constitute the highly symmetric (hexagonal or truncated triangle) flakes, the degree of micro-scale anisotropy of the sub-domains, however, is likely to be reduced by alternating the Re chain direction caused by a variety of imperfections such as cluster defects and vacancies. This is particularly the case in proximity to the defect-rich grain boundaries where the Re chain directions are strongly changed, although the structural anisotropy is quickly recovered away from grains boundaries in relatively defect-free areas within the sub-domains. Therefore, it is predicted that structural and optical anisotropy will be insignificant where there are high density of defects causing nearly randomly oriented Re-chains, and achieving macroscale anisotropic ReS_2 will be a large challenge.

3.8. Conclusions

State-of-art CVD growth techniques, together with angle resolved Raman and 4 K reflectivity spectroscopy, AFM, and STEM measurements have been performed to explore domain architectures, grain boundaries, and crystalline anisotropy of CVD grown quasi-1D ReS_2 monolayers. For the first time, we have obtained highly crystalline ReS_2

flakes with well-defined anisotropic sub-domains demonstrated by angle resolved Raman mapping measurements, which also allowed us to determine the Re chains (*b*-axis) directions within each sub-domain in both hexagonal and truncated triangular flakes. This is particularly surprising since anisotropic interfacial energy stabilizes the completely random dendritic growth. The HR-STEM measurements have provided the insight into atomic architectures at ReS_2 grain boundaries and demonstrated how defect density can reduce the structural anisotropy. The cluster and vacancy defects at the grain boundaries can cause Re chains to change the directions to different angles; those defects located away from the grain can either cause Re chains to change direction in multiples of 60°, or even rotate chains in 180 degrees around their own *b*-axis.

From manufacturability and application perspective, further work may be focused on achieving large anisotropic ReS_2 monolayer flakes for chip scale applications. To achieve this goal, either more sophisticated selective epitaxy routes need to be developed for fabrication at a targeted area with well-defined crystalline anisotropy. Besides, further insights will also be given to alloying ReS_2 and $ReSe_2$, which potentially offers the possibility for bandgap and carrier type engineering for future applications.

Chapter 4 UNUSUAL VIBRATIONAL PROPERTIES OF TITANIUM TRISULFIDE UNDER EXTREAM PRESSURE

This chapter establishes the unusual vibrational properties of quasi-1D TiS_3 both experimentally and theoretically through state-of-art high pressure Raman measurements and density function theory (DFT) calculations. As mentioned in previous chapter, the fundamental vibrational nature of TiS_3 is still unclear. However, understanding the such properties is essential to understanding the true potential of this material since vibrational characteristics dictate its optical properties (through phonon-photon interactions), electronic properties (through electron-phonon interactions). Our work hopes to have solved this problem and may boost the understanding of their optical, electrical, and thermal properties.

4.1. Crystal structure of TiS_3

Titanium trisulfide (TiS_3) crystallizes in a monoclinic $P2_1/m$ space group, and the lattice structure is shown in **Figure 3.1**, respectively. In each unit cell, two titanium atoms and six sulfur atoms are connected within two distorted prisms, in which the titanium atom is at the top vertex of the prism, and the three sulfur atoms are at the three bottom vertices. The two prisms in the unit cell are connected by binding the titanium atoms with their closest sulfur atoms in the neighbor prism. The lattice constants are calculated as a = 4.98 Å, b = 3.39 Å, and c = 8.89 Å. Here, we observe two types of sulfur atoms in a single prism: (1) the sulfur atom that is bonded to the two titanium atoms acting as a bridge, and (2) the remaining two S atoms that are only bonded to only

one Ti atom. For clarification, the two types of sulfur atoms are differentiated and labeled as bridge sulfur and sulfur-sulfur pair. The repeating parallel chains of these triangular prisms are weakly coupled to each other via van der Waals interaction, giving rise to its in-plane signature structural anisotropy.

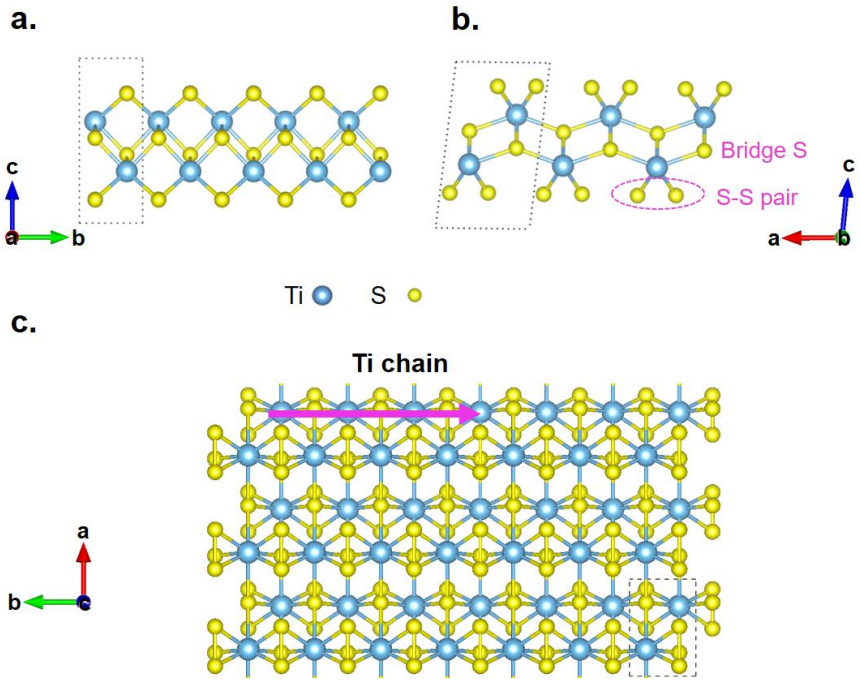

Figure 4.1 Lattice structure of TiS_3 along a. [100], b. [010], and c. [001], respectively.

4.2. Crystal growth and characterization

As discussed in session 2.1, the TiS_3 whiskers were grown directly from the interaction between titanium and sulfur in a sealed evacuated quartz ampule via chemical vapor transport process[2, 3]. Typical growth yields TiS_3 on the interior wall of the quartz ampule (**Figure 4.2a and 4.2b**) in a whisker geometry as a result of the highly anisotropic structure, and the whiskers measures from ~ 0.5 up to 5 mm in length. The XRD pattern (**Figure 4.2c**) obtained was found to be consistent with JCPDS-ICDD 15-

0783. Intense peaks also suggest further confirms the high crystallinity the synthesized TiS_3.

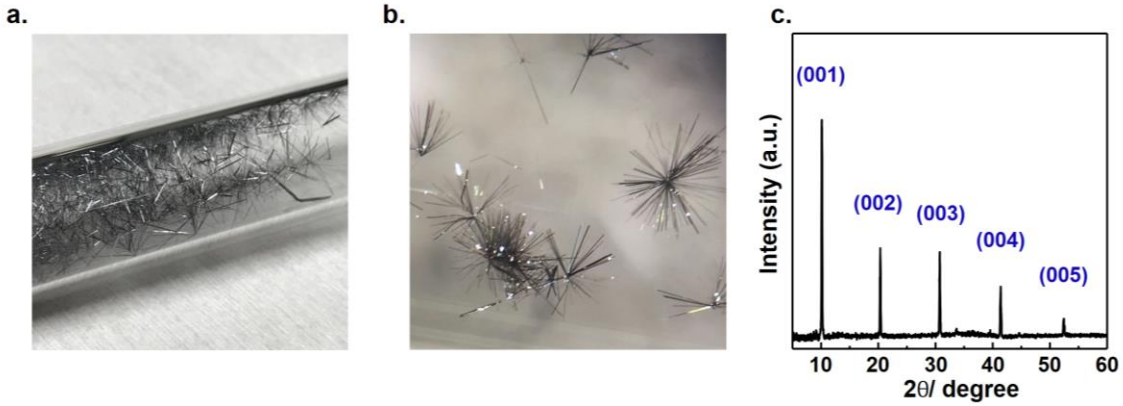

Figure 4.2 As grown TiS_3 on the interior wall of the quartz ampule. b. Macro image of the TiS_3 whiskers. c. Powder XRD pattern of TiS_3 whiskers.

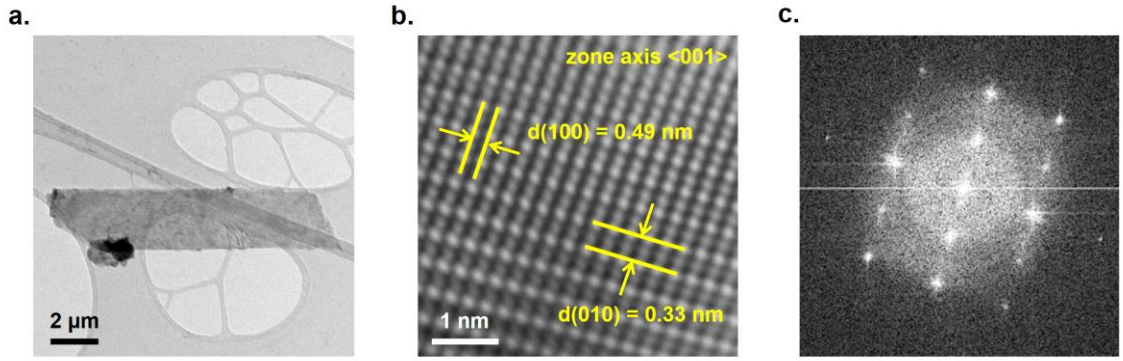

Figure 4.3 a. Low-magnification bright-field TEM image of TiS_3 ribbon. b. HR-TEM image of TiS_3 with zone axis aligned along <001> and c. the corresponding FFT image.

The low-magnification TEM images (**Figure 4.3a**) show the ribbon shape of the TiS_3 microcrystals: the longer dimension along the b-axis measures ~ 11 μm and the width measures ~ 4 μm. The high-resolution transition electron microscopy (HR-TEM) image of the TiS_3 is shown in **Figure 4.3b**. The plane spacing measures ~ 0.49 and ~ 0.33 nm, which agrees well with the distance along <100> and <010> lattice direction when the

sample is aligned with the (001) crystal plane (JCPDS-ICDD 15-0783). The corresponding fast Fourier transform (FFT) image is shown in **Figure 4.3c**.

4.3. Raman spectroscopy and phonon dispersion

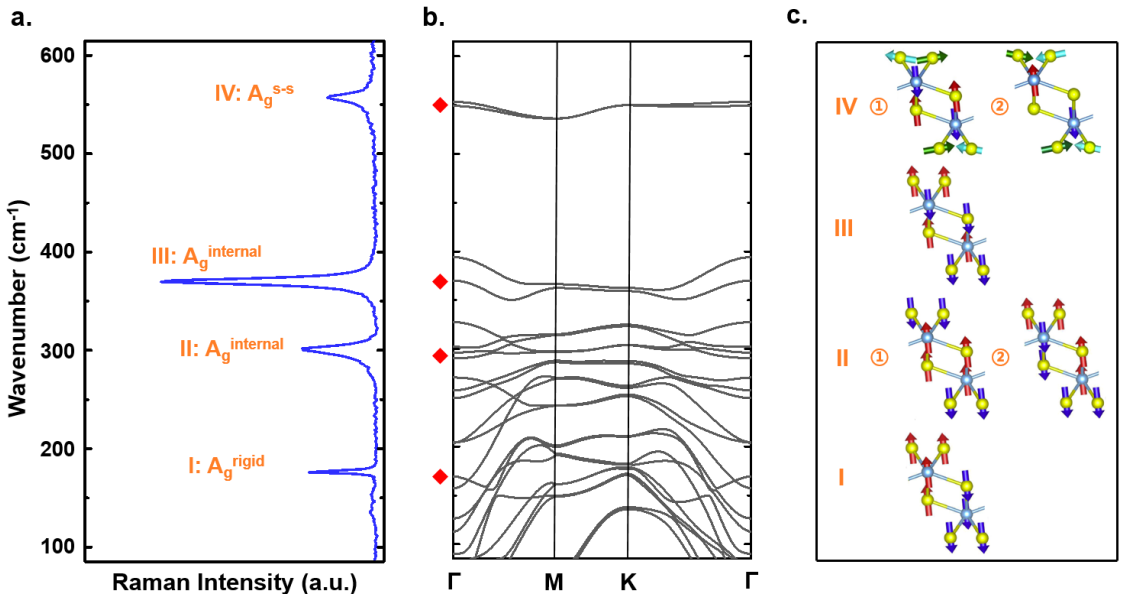

Figure 4.4 a. Raman spectrum of TiS_3 whiskers measured in ambient at room temperature. b. Phonon dispersion of TiS_3 calculated by density function theory. c. The corresponding Raman active optical modes.

Raman spectrum of TiS_3 (**Figure 4.4a**) shows four prominent peaks located at 176, 298, 370, and 556 cm^{-1}, respectively, and the phonon dispersion is shown in **Figure 4.4b**. Each primitive unit cell of TiS_3 contains 2 titanium and 6 sulfur atoms, thus the phonon dispersion yields 3 acoustic modes and 21 optical modes in the first Brillouin zone. The measured Raman spectrum match reasonably well with the calculated phonon dispersion spectrum, in particular to those Raman active modes highlighted by red diamonds in **Figure 4.4b**. Finite displacement method has been performed to understand the

vibrational nature of these Raman active modes, and characteristic atomic motion of each Raman active branch is shown in **Figure 4.4c**.

Displacement method results show that lowest frequency peak (176 cm^{-1}) originates from out-of-phase rigid vibration of each 1D-like TiS_3 chain extending along *b*-axis (Figure 7c labelled I). Since these chains move in the out-of-plane direction (*c*-axis) and the atomic displacements within the chain is in-phase, keeping the rigidity of 1D chains owing to no relative displacement among TiS_3 atoms, we label this peak as I-A_g^{rigid}. Overall, this mode can be pictured as two quasi-1D chains vibrating with respect to each other while keeping Ti-S bonding distance fixed within each chain. In contrast to the rigid chain I-A_g^{rigid} mode, the peaks at 298 cm^{-1} (II-$A_g^{internal}$) and 370 cm^{-1} (III-$A_g^{internal}$) involve vibration within each TiS_3 layer, and these two vibrational modes are labeled as $A_g^{internal}$ in relation to internal vibration in each layer. A closer look at Γ~300 cm^{-1} show that two different optical braches coincide with each other. This implies that the II-$A_g^{internal}$ mode consists of two degenerate modes as shown in **Figure 4.4c**. Here, the main difference between mode II-$A_g^{internal}$-① (at lower frequency) and mode II-$A_g^{internal}$-② (at higher frequency) lies in the relative vibration direction between the Ti atoms, bridge S atoms, and S-S pairs across the two prisms. We note that the presence of two near degenerate Raman peaks results in much larger full-width half-maximum (FWHM) value (12.1 cm^{-1}) compared to I-A_g^{rigid} (3.3 cm^{-1}) and III-$A_g^{internal}$ (7.9 cm^{-1}). Large FWHM value of II-$A_g^{internal}$ is attributed to degeneracy (presence of multiple) of modes at ~298 cm^{-1}. Similar to II-$A_g^{internal}$, the III-$A_g^{internal}$ mode also involves vibration of atoms making up the individual layers except that three S atoms (both the bridge S and S-S pair) vibrate

oppositely with the Ti atom in a single prism, whereas the other prism moves in a central symmetry way with it.

In contrast to all the above modes, highest frequency peak at 556 cm^{-1} also appear doubly degenerate with relatively large FWHM value (12.3 cm^{-1}), shown in Figure 7a. Surprisingly, these peaks are predominantly made of in-plane out of phase motion of S-S pair and in part the out-of-plane motion of Ti and the bridge S atoms. Considering the signature S-S pair vibration, this peak is labelled as IV-A_g^{S-S}.

4.4. Pressure dependent Raman spectroscopy

Under high pressure, the interlayer distance of TiS_3 changes accordingly, and as a result, the A_g Raman modes will behave differently. Besides, the material may also undergo unique phase transition under high pressure. Based on the above two motivations, pressure dependent Raman spectroscopy studies have been performed to further understand the vibrational properties of TiS_3 whiskers. The measurements were taken under such a configuration that the laser excitation (**E**) and detection (**D**) polarization was aligned parallel to the chain direction (**E** ∥ **D** ∥ *b*-axis) to achieve high signal to noise ratio. Hydrostatic pressure was applied using a drop of methanol-ethanol (4:1) mixture as the pressure media.

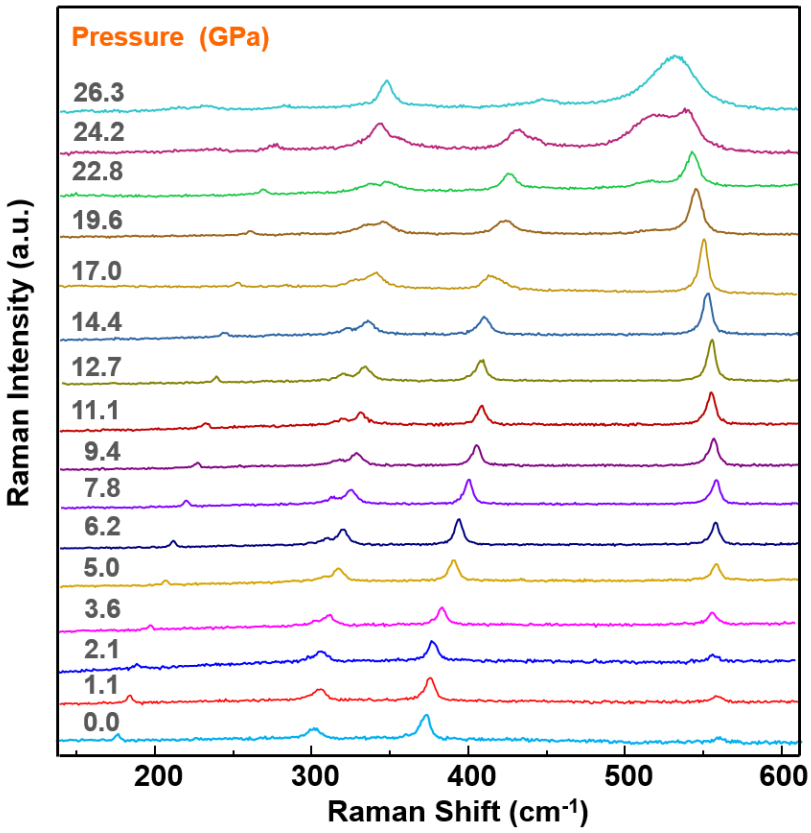

Figure 4.5 Pressure dependent Raman spectrum of TiS_3 under hydrostatic pressure.

The pressure dependent Raman spectrum is shown in **Figure 4.5**: hydrostatic pressure is added from ambient pressure up to 26.3 GPa, which is the highest pressure that can be attained in our setup. It is observed that the I-A_g^{rigid} mode, II-$A_g^{internal}$ mode, and III-$A_g^{internal}$ mode all stiffen with increasing pressure as a result of the increased interlayer interaction, which either stiffens the atomic bonds within each monolayer or increases the interaction strength across the chain structures.

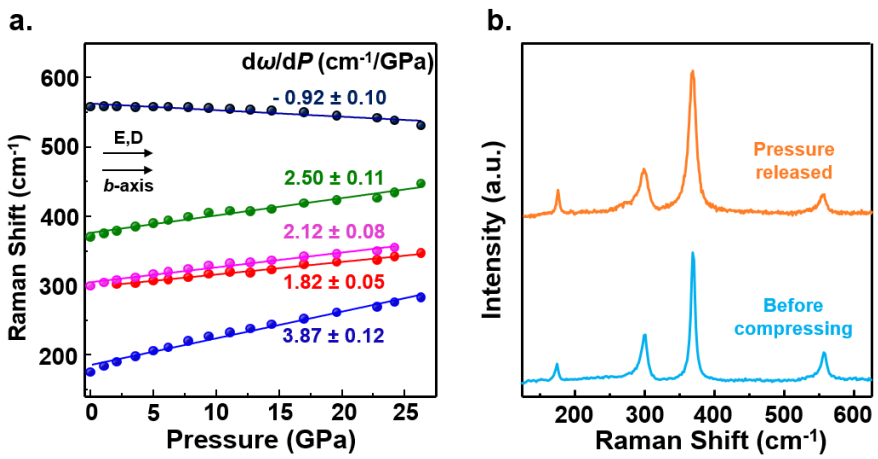

Figure 4.6 a. Raman peak position as a function of pressure. b. Comparison between the Raman spectra of TiS_3 before applying and after releasing pressure.

The peak position of the vibration modes scales linearly with pressure (**Figure 4.6a**), and the frequency values can be therefore described as $\omega(P) = \omega_0 + (d\omega/dP)P$, where ω is the peak position, P is the pressure. It is also noteworthy that the A_g^{rigid} mode is significantly more sensitive to applied pressure ($d\omega/dP$ = 3.82 cm^{-1}/GPa) compared to the internal modes ($d\omega/dP$ = ~ 2 cm^{-1}/GPa) due to the easiness to increase interaction between moderately interacting 1D-like chains. We conclude that the I-A_g^{rigid} mode is much stiffer than other modes due to its rigid chain nature. In contrast to other Raman modes, the $A_g^{S\text{-}S}$ mode softens with pressure ($d\omega/dP$ <0), which is rather unique compared to the observations from layered systems. The origin of negative $d\omega/dP$ value of $A_g^{S\text{-}S}$ mode can be attributed to the following reasons. Since the IV-$A_g^{S\text{-}S}$ mode is the only mode with finite in-plane S-S vibrations, it is possible that the reduced interlayer distance at high pressures increases the S-S distance through increase in S-Ti-S angle due to increase orbital interaction between adjacent layers. Therefore, the negative $d\omega/dP$ value is potentially related to the softening of S-S vibration reducing the vibrational

frequency of A_g^{S-S} mode. After the pressure is released, the Raman peaks (**Figure 4.6b**) retains the same as the original state (before compressing), suggesting that the pressure effects are reversible up to 26.3 GPa.

Table 4.1 Quantitative analysis of vibration properties of TiS_3

Vibration mode	$\omega_{ambient}$ (cm^{-1})	$d\omega/dP$ (cm^{-1}/GPa)	Grüneisen parameter
I - A_g^{rigid}	176	3.87 ± 0.12	1.10 ± 0.03
II - $A_g^{internal}$ - ①	298 (degenerate)	1.82 ± 0.05	0.31 ± 0.01
II - $A_g^{internal}$ - ②		2.12 ± 0.08	0.36 ± 0.01
III - $A_g^{internal}$	370	2.50 ± 0.11	0.34 ± 0.01
IV - A_g^{s-s} - ①	556 (degenerate)	-	-
IV - A_g^{s-s} - ②		- 0.92 ± 0.10	- 0.08 ± 0.01

To further understand the mode stiffness, we also performed quantitate analysis by calculating the Grüneisen parameters of a vibration mode, γ, which is defines as $\gamma = -(\partial \ln\omega/\partial \ln V) = (\omega\chi_T)^{-1}(\partial\omega/\partial P)$, where ω is the frequency of the specific mode of interest, V is the volume, P is the pressure, and $\chi_T = -V^{-1}(\partial V/\partial P)$ is the isothermal compressibility. In our case, the isothermal compressibility χ_T is replaced as $-c^{-1}(\partial c/\partial P)$ since our interested modes are along the c axis. Thus, the final expression of the Grüneisen parameter is expressed as $\gamma = (-\omega c^{-1}(\partial c/\partial P))^{-1}(\partial\omega/\partial P)$. The $d\omega/dP$ values and the calculated Grüneisen parameters are shown in **Table 4.1**.

4.5. Lifting the degeneracy of Raman modes at high pressures

In addition to the negative pressure dependence of $A_g^{S\text{-}S}$ mode, we note the II-$A_g^{internal}$ and IV-$A_g^{S\text{-}S}$ split into two peaks going from ambient to high pressures. In **Figure 4.7**, we compare the shape of each Raman peak between 0 and 22.8 GPa: the II-$A_g^{internal}$ mode and the IV-$A_g^{S\text{-}S}$ modes both splits into two parts, whereas the other two modes (I-A_g^{rigid} and III-$A_g^{internal}$) retain their overall peak shape except minuscule broadening in their full width at half maximum (FWHM). The origin of the Raman peak splitting may (erroneously) be interpreted as 'pressure induced-phase transition'. However, careful pressure dependent DFT calculations illustrate that material retains its symmetry and does not undergo phase transition up to 30 GPa. Furthermore, we note that the pressure induced peak splitting only occurs at the doubly degenerate II-$A_g^{internal}$ and IV-$A_g^{S\text{-}S}$ modes. Since each Raman mode, including degenerate ones, has different pressure dependence (different $d\omega/dP$ values), we argue that the peak splitting effect may be attributed to lifting the degeneracy of II-$A_g^{internal}$ and IV-$A_g^{S\text{-}S}$ modes at high pressure.

More explicitly, at ambient pressure, the degenerate modes are in close proximity to each other within ~ 5 cm^{-1}, causing II-$A_g^{internal}$ and IV-$A_g^{S\text{-}S}$ modes to have larger FWHM values (12.1 cm^{-1} and 12.3 cm^{-1}) compared to other modes. As the pressure is being applied, the degenerate modes start to separate from each other due to different $d\omega/dP$ values (**Table 4.1**). In addition, the splitting of the II-$A_g^{internal}$ mode is shown in **Figure 4.7b**, the FWHM values of the two peaks at 22.8 GPa (the green dash line representing the II-$A_g^{internal}$-① mode and the blue dash line representing the II-$A_g^{internal}$-② mode) are comparable to that of the original degenerate II-$A_g^{internal}$ mode at ambient pressure.

Similarly, the blue and green dash lines in **Figure 4.7d** can be attributed to the degenerate mode which consists of two A_g^{S-S} peaks.

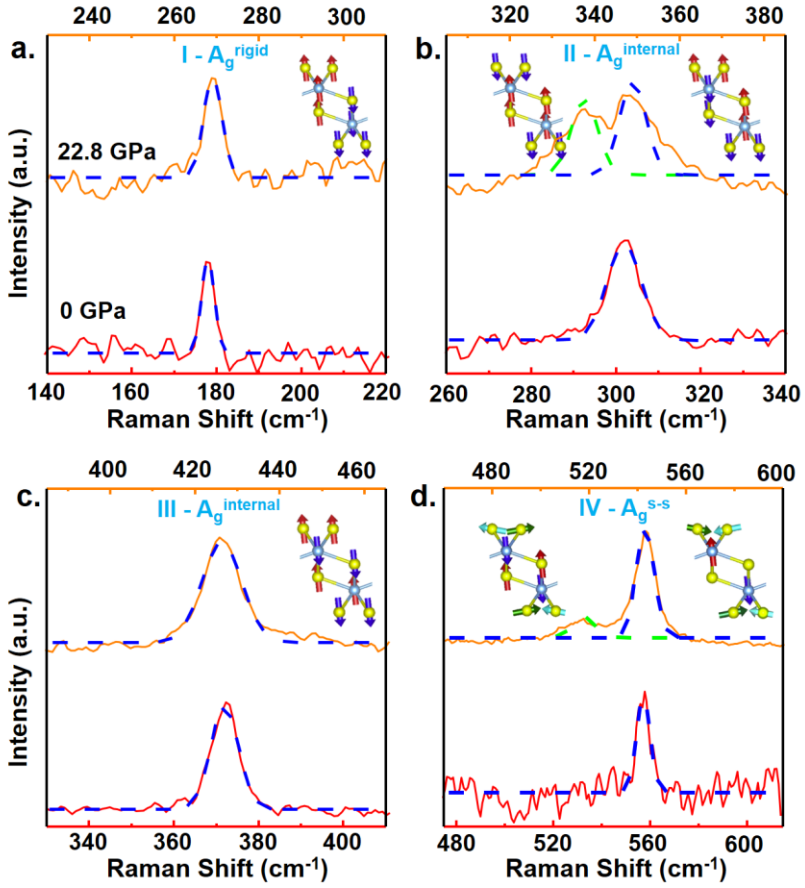

Figure 4.7 A comparison between the shape of each Raman peak at 0 and 22.8 GPa showing the lifting of degeneracy. a. I-A_g^{rigid} mode, b. II-$A_g^{internal}$ mode, c. III-$A_g^{internal}$ mode, and d. IV-A_g^{s-s} mode, respectively.

4.6. Angle-resolved Raman spectroscopy

In addition to the unusual pressure dependence of the vibrational modes. We note that Raman peaks show large angular variation with polarization angle, which is apparent from angle-resolved Raman spectroscopy data presented in 2D contour plots in **Figure**

4.8, in the parallel (**E** || **D**) and cross (**E** ⊥ **D**) configurations, respectively. The polarization angle is defined as the angle between the detection direction and the *b* axis. Depending on the polarization angle and configuration, Raman intensity of different modes goes through maxima and minima, showing two- or four-lobed features that are associated with the particular Raman tensors specific to this material system.

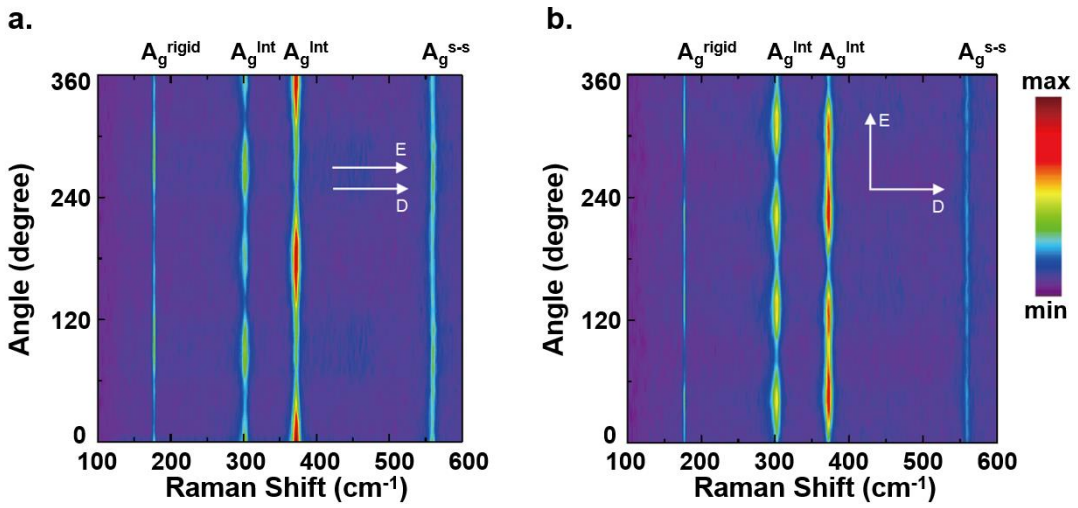

Figure 4.8 Angle resolved Raman spectroscopy (2D contour plots) for all the Raman peaks in the a. parallel (**E** ‖ **D**), and b. cross (**E** ⊥ **D**) configuration.

4.7. Conclusions

Our results mark the first high pressure Raman and theoretical investigation of pseudo-1D TiS_3 layered material and establish the fundamental understanding of TMTCs material systems. DFT and finite displacement methods demonstrated the TiS_3 vibrational modes are drastically different from other isotropic (MoS_2, WSe_2, etc.) even anisotropic material (ReS_2, $ReSe_2$, and black phosphorus) systems. TiS_3 exhibits various Raman modes that are related to unique rigid chain vibrations (A_g^{rigid}), sulfur-sulfur pair oscillations (A_g^{s-s}), and conventional out-of-plane modes ($A_g^{internal}$). Pressure dependent

Raman studies reveal that the A_g^{S-S} mode has a unique negative response to applied hydrostatic pressure, and the $A_g^{internal}$ mode at 298 cm^{-1} and the A_g^{S-S} mode at 556 cm^{-1} appear to be degenerate at ambient pressure, which can be lifted when pressure is applied. Overall results establish, priori unknown vibrational properties of a new-class of material TiS_3 with broader impact towards understanding and interpreting thermal (thermal transport), structural (defects and impurities) and mechanical (strain) properties of TiS_3 relevant to potential applications in optoelectronic and photonic devices.

Chapter 5 HIGH PRESSURE VIBRATIONAL PROPERTIES OF ORTHORHOMBIC TANTALUM TRISULFIDE

This chapter reports the unique vibrational properties of orthorhombic tantalum trisulfide (*o*-TaS_3) measured through angle-resolved Raman spectroscopy and high-pressure diamond anvil cell studies. The broad-spectrum Raman measurements first identify optical and low frequency shear modes in pseudo-1D TaS_3 for the first time, and introduce their polarization resolved Raman responses to understand atomic vibrations for these modes. The high-pressure Raman measurements reveal previously unknown four distinct types of responses to applied pressure, including positive, negative, and non-monotonic pressure dependence. Our results also reveal that the material approaches to isotropic limit under applied pressure as evidenced by much reduced (~ 70%) degree of anisotropy. Overall findings not only significantly advance our understanding of their fundamental properties of pseudo-1D materials, but also offer valuable insights about thermal, electrical, and optical properties of pseudo-1D material systems.

5.1. Charge-density-wave behaviors and crystal structures

Tantalum trisulfide (TaS_3) is known as a quasi-one-dimensional (1D) semiconductor which become a charge-density-wave (CDW) conductor undergoing Peierls' transition at low temperature[101]. The electrical properties, especially the charge-density-wave transport properties[102-103] of bulk TaS_3 has been investigated by different groups. Temperature dependent electrical resistivity measurements[104] on *o*-TaS_3 exhibits a metal-semiconductor transition at T_C = 215 K, whereas the transition temperature increases to

240 K for *m*-TaS_3 with another transition in the semiconducting state at 160 K. Temperature dependent Raman measurements on *o*-TaS_3 show that the position of the peak at 283 cm^{-1} shifts lineally to high wavenumber between 300 K and 220 K until a step shift of 13.5 cm^{-1} is observed at 220 K, below which non-linear Raman behavior takes place, revealing the Peierls' transition at ~ 220 K[105]. The electrical resistance of *o*-TaS_3 measured from 1 to 300 K at high pressure up to 20 GPa shows a gradual decrease of the transition temperature with applied pressure of $T_{CDW} = 215K[(P_c\text{-}P)/P_c]^{0.5}$, where the critical pressure P_c equals 11.5 GPa. Also, a superconducting dome with a maximum transition temperature T_c = 3.1 K appears at high pressures[106].

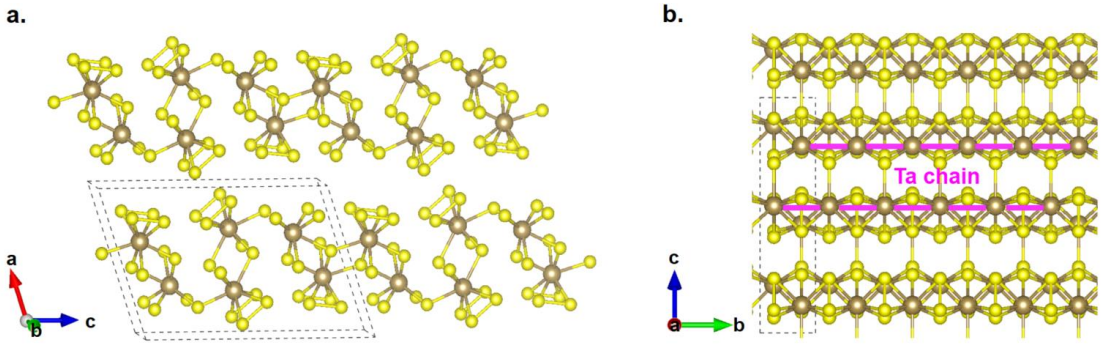

Figure 5.1 a. Crystal structure of *m*-TaS_3 with the dash line presenting the unit cell. b. Infinite Ta chains extending along *b*-axis.

TaS_3 crystalizes in two distinct phase: orthorhombic and monoclinic[107-108]. The lattice parameters have been determined to be a = 9.52 Å, b = 3.34 Å, c = 14.91 Å, and β = 109.99° for *m*-TaS_3, and a = 36.80 Å, b = 15.17 Å, and c = 3.34 Å for *o*-TaS_3**.** The *m*-TaS_3 unit cell (**Figure 5.1a**) contains six tantalum atoms and eighteen sulfur atoms where each the center tantalum atom is surrounded by six sulfur atoms located at the corners of a trigonal prism, and six prisms are connected by tantalum-sulfur bonding between neighboring prisms. Those trigonal prisms stack on top of each along the *b*-axis by

sharing the triangular sulfur faces, forming infinite Ta chains (**Figure 5.1b**) and giving rise to anisotropic properties. The psudo-1D chains in those weakly interacted van der Waals TaS_3 layers makes TaS_3 known as an anisotropic 2D material. Although the atom arrangement and coordinates of the earlier discovered orthorhombic (*o*-) TaS_3 remain unknown, its unit cell has been described as stacking four slabs of *m*-TaS_3 unit cell and two potential unit cell structures of *o*-TaS_3 are shown in **Figure 5.2**. In contrast with *m*-TaS_3, the Ta chains in the *o*-TaS_3 extends along the *c*-axis.

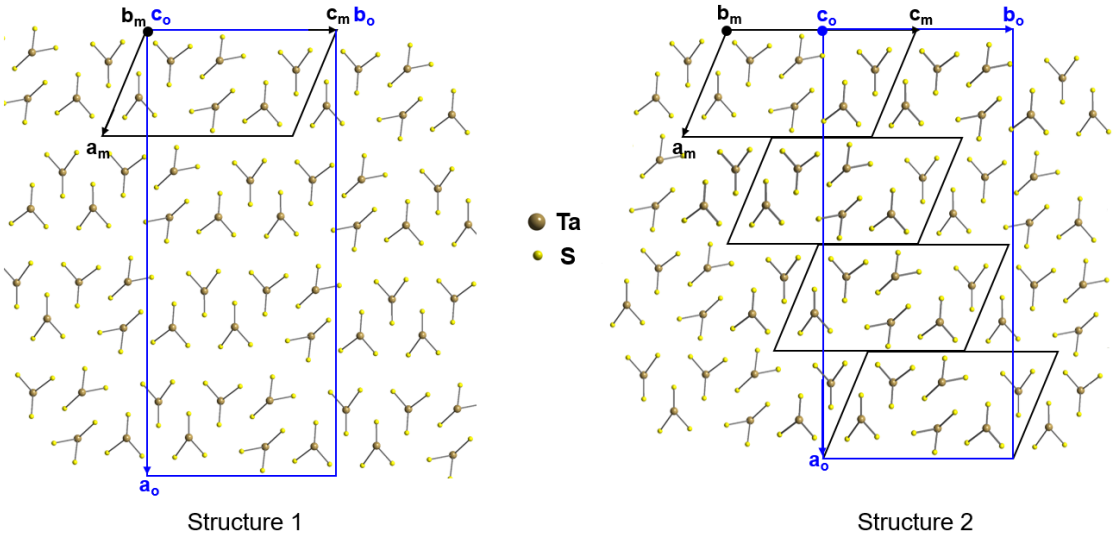

Figure 5.2 Building the unit cell structures of *o*-TaS_3 described as stacking four slabs of *m*-TaS_3 unit cells.

5.2. Growth and characterization of orthorhombic-TaS_3

The *o*-TaS_3 was grown using direct CVT method from tantalum and sulfur precursors in an evacuated ampule with T_{hot} = 650 °C and T_{cold} = 550 °C for 7 days. As shown in **Figure 5.3a**, the as prepared *o*-TaS_3 is hair-like black crystals, indicating the quasi-1D nature. The XRD data in **Figure 5.3b** further confirms the high crystallinity.

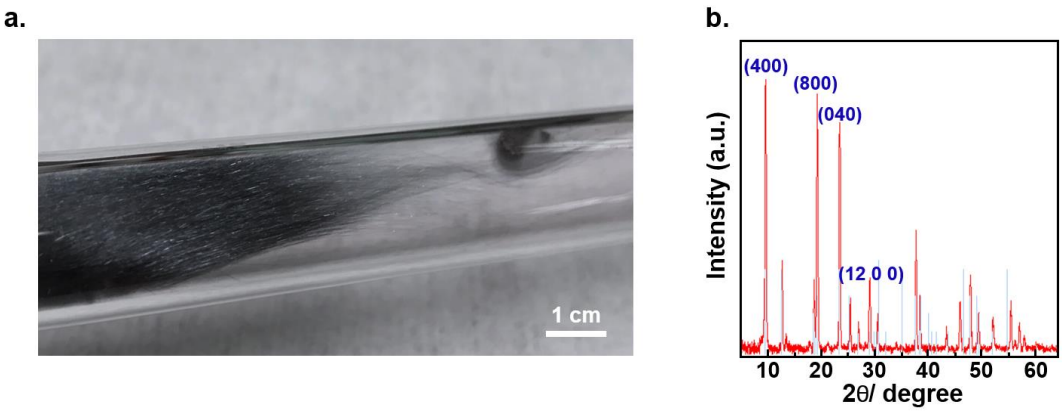

Figure 5.3 a. As prepared *o*-TaS_3 crystal in the sealed ampule. b. XRD spectrum of *o*-TaS_3 (red) compared with database (light blue).

The SEM image in **Figure 5.4a** shows ribbon-like structures of the as-grown TaS_3, which further proves the highly anisotropic structure of the material. The bright field TEM image of a single TaS_3 whisker is shown in **Figure 5.4b**, and the crystal directions can be determined from the electron diffraction pattern (inset), which indicates that the longitudinal direction of the whisker is aligned with [001] axis.

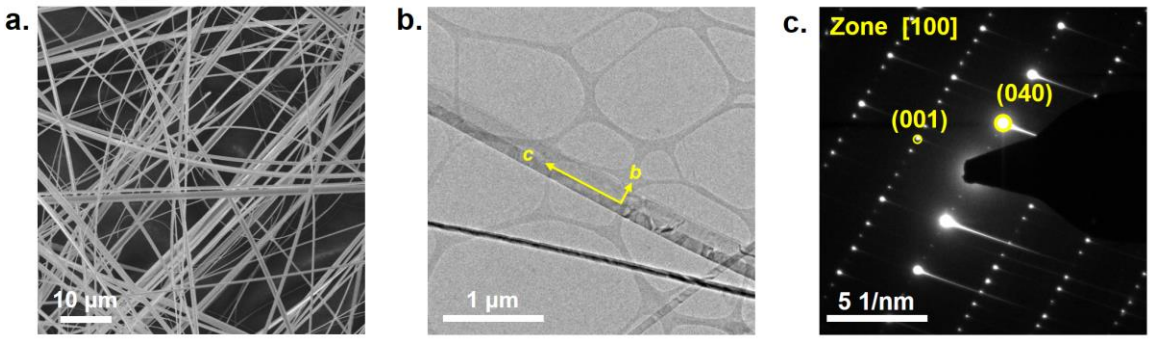

Figure 5.4 a. Scanning electron microscopy (SEM) image of *o*-TaS_3 whiskers showing its pseudo-1D nature. b. Transmission electron microscopy (TEM) and c. corresponding electron diffraction pattern of a single *o*-TaS_3 nanoribbon.

In contrast to the monoclinic phase of TaS_3 where the Ta chains propagates along its *b*-axis, the chain direction (also known as the whisker growth direction) of the *o*-TaS_3

extends along the *c*-axis, resulting in the strong in-plane anisotropy. In the out-of-plane direction (*a*-axis), the TaS_3 layers made of repeating parallel Ta chains are weakly coupled to each other via van der Waals interaction. Similar to *m*-TaS_3, *o*-TaS_3 can be exfoliated down to thin layers on 285 nm SiO_2/Si wafers. Due to its higher mosh hardness scale as well as geometrical anisotropy, however, typical exfoliation process only yields pseudo-1D ribbons that measure between 5 to 15 nm in thickness. Even though, our studies are in the few-layer limit, conclusions extend to monolayers since Raman peak position shifts by ~ 5 cm^{-1} by thickness variation which is a negligible shift for the studies presented in this work.

5.3. Angle-dependent Raman spectroscopy

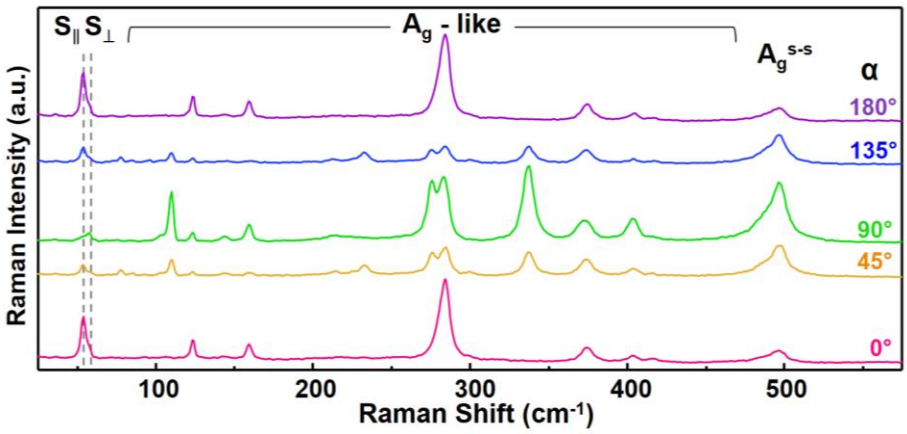

Figure 5.5 Raman spectra of an *o*-TaS_3 nanoribbon exfoliated on sapphire substrate taken at selected polarization angle 0°, 45°, 90°, 135°, and 180°.

Due to their crystalline anisotropy, Raman / vibrational properties of pseudo-1D systems such as TiS_3 and ReS_2 exhibit high sensitivity to angle between chain direction and excitation polarization. Although the lack of atomic structure of TaS_3 limits the ability to depict a full picture of the phonon vibrational modes and it warrants future

theoretical and experimental studies, the angle-resolved Raman polar plots, however, allow one to identify the fundamental origin of variety of atomic vibrations of *o*-TaS_3. In our studies, Raman spectrum of *o*-TaS_3 was measured at different angles that are defined as the angle between incident laser polarization and the *c*-axis (chain direction) of a nanoribbon, and the Raman spectra at selected angles (0°, 45°, 90°, 135°, and 180°) are shown in **Figure 5.5**. Due to complex structure, TaS_3 has primary Raman peaks located at 54, 58, 77, 104, 110, 123, 144, 159, 233, 276, 284, 337, 374, 404, 484, and 498 cm^{-1}.

We find that intensity of the observed Raman peaks displays strong dependence on α (the angle between excitation polarization and *c*-axis) and hence the crystalline orientation. These angular Raman measurements were performed at 15° increments, and the Raman intensity of six characteristic Raman modes have been selected to generate a series of full 360° rotation polar plots (**Figure 5.6**). At low frequency regime, o-TaS_3 display prominent peaks located at 54 and 58 cm^{-1} which is well below anticipated optical branches. These peaks originate from shear displacements between adjacent TaS_3 layers, and appear at low frequencies due to weak interlayer coupling. Out of these three modes, the 54 cm^{-1} mode exhibits a two-lobed feature with maximum value found at 0° and 180°, indicating enhanced Raman scattering when the E-field is along the chain direction. Since the Raman intensity correlates to the polarizability tensor, we conclude that 54 cm^{-1} peak is related to shear mode displacement of individual TaS_3 layers along the chain direction. Thus, this peak is identified as $S_{\parallel}$ and enables us to identify the Ta-chain direction through quick and non-destructive optical methods without any need for advanced microscopy techniques. We note that these shear vibrations can also take place in other directions. Thus, we observe two shear (S) Eigen modes with interlayer displacement

parallel ($S_{\parallel}$ ~54 cm^{-1}) and perpendicular/non-parallel ($S_{\perp}$~58 cm^{-1}) to the Ta-chain direction with peaks at slightly different locations ($\Delta\omega_{(\perp-\parallel)}$ ~ 4 cm^{-1}). Since the chemical and atomic environment change is greater for displacement non-parallel to Ta-chain direction, $S_{\perp}$ vibration frequency is blue shifted (higher) by $\Delta\omega$ and its polar response reflects displacement in other directions.

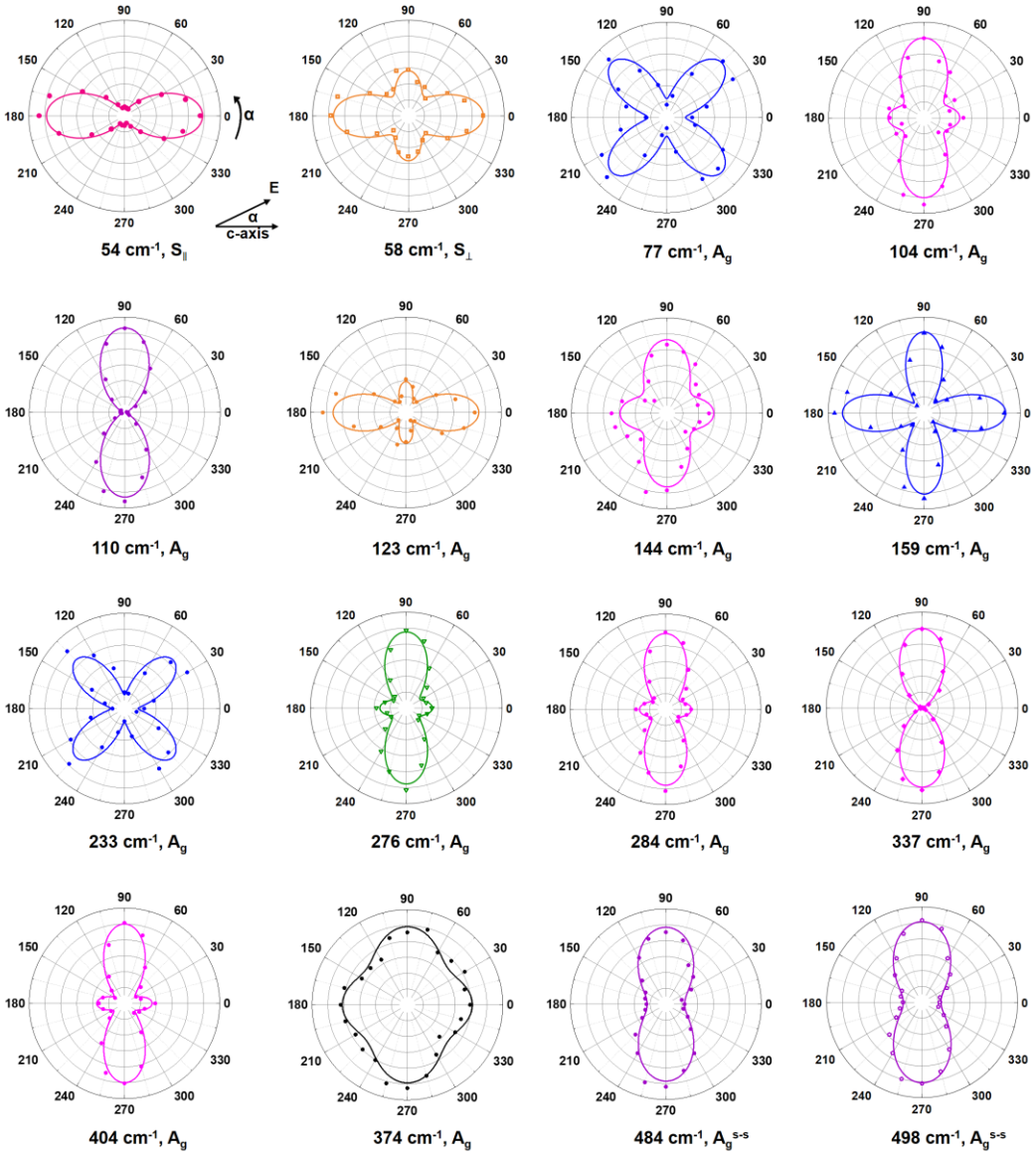

Figure 5.6 Angle-dependent Raman polar plots of an *o*-TaS_3 nanoribbon.

The ARS measurements on the Raman peaks that are associated with optical phonon modes display either four-lobed (such as the 77 cm^{-1} and 159 cm^{-1} peaks) or two-lobed response with orthogonal relation to the c-axis peaks. For example, both A_g - like mode at 337 cm^{-1} and the A_g^{s-s} mode at 498 cm^{-1} exhibit maxima at 90°, suggesting strong atomic vibrations perpendicular to the Ta-chain direction, and cannot be utilized to assess crystalline direction. However, we note that many of the observed angle dependent responses and complex anisotropic Raman response are often attributed to the equally complex Raman tensor of each mode as well as the absorption of the incident laser. Due to the anisotropic light-matter interactions, Raman features can show strong variation with respect to laser wavelength such as black phosphorus (BP) and gallium telluride (GaTe). In our studies, we have focused our Raman measurements on green laser (λ=532 nm) since the Raman intensity is much enhanced compared to other excitation wavelengths due to various reasons including larger absorption coefficient, larger (induced) polarization, and/or larger Raman scattering cross-section at that wavelength.

5.4. High-pressure Raman spectroscopy

To further understand the vibrational properties of *o*-TaS_3, we have performed pressure dependent Raman studies on TaS_3 under hydrostatic pressure using a diamond anvil cell (DAC) where the pressure gauge was a small piece of ruby. Cesium iodide (CsI) served as the pressure transmitting medium. Since Raman intensity maxima of most peaks are seen when the excitation is either parallel (α = 0°) or perpendicular (α = 90°) to the chain, we focus on these two specific configurations and the pressure dependent Raman spectra are shown in **Figure 5.7a** and **5.7b**.

Upon application of pressure, Raman modes located at ω_0 = 123, 144, 276, and 373 cm^{-1} start to split into two or more peaks above 3.7 GPa. In principle, the Raman peak splitting or the presence of new peaks can be attributed to phase transition. For o-TaS_3, however, peak splitting occurs only for select type of modes as opposed to peaks splitting for all Raman peaks due to Brilliouin zone changes during phase transition. Considering that Raman spectrum does not undergo sudden and drastic changes, and peak splitting is only valid for certain set of peaks at rather low pressures (3.7 GPa), we eliminate the possibility of phase transition. Instead, it is likely that complex atomic structure of *o*-TaS_3 leads to Raman peaks made of multiple degenerate Raman modes at ambient pressure with different dω/dP pressure coefficients which results in peak splitting behavior at finite pressure values.

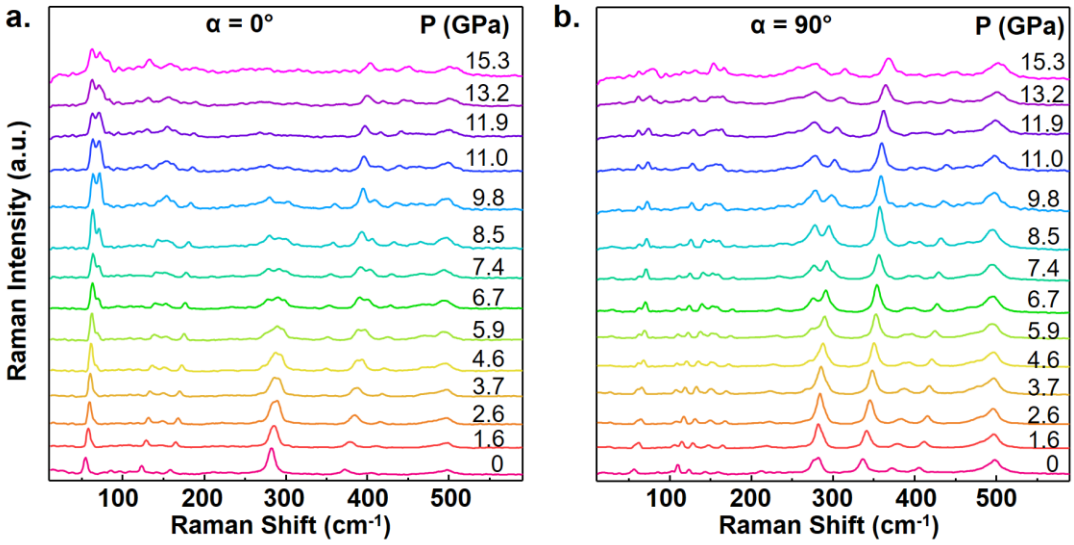

Figure 5.7 Raman spectra of *o*-TaS_3 at selected pressures measured at parallel configurations with the polarization direction a. parallel (α = 0°) and b. perpendicular (α = 90°) to the chain, respectively.

Here, the peak position (ω_p) as a function of pressure (**Figure 5.8**) can be described as $\omega_p = \omega_0 + (d\omega/dP)P$ with ω_0 representing the peak position in ambient, and the fitted $d\omega/dP$ values of each mode are given in **Figure 5.9a.** We also define the $(\Delta\omega/\Delta P)_{Pi}$ value as the pressure dependence (slope) between two successive data points as $(\Delta\omega/\Delta P)_{Pi} = (\omega_i-\omega_{i-1})/(P_i-P_{i-1})$ with the positive integer *i* representing the i_{th} pressure point in **Figure 5.9b**.

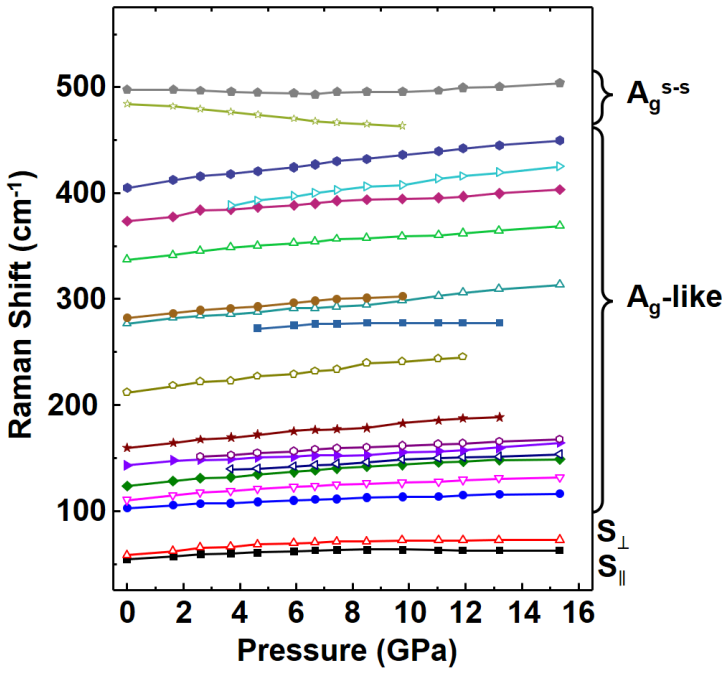

Figure 5.8 Pressure dependent Raman peak position from ambient pressure to 15.3 GPa.

Closer inspection of the Raman peak position with respect to pressure (**Figure 5.9a**) show that observed Raman peaks display four kinds of distinct pressure dependence: Type-I with saturating $\Delta\omega/\Delta P$ response with $\Delta\omega/\Delta P$ approaching ~ 0 cm^{-1} GPa^{-1} above critical pressure ($P_{critical}$ ~ 8.5 GPa), type-II with positive $\Delta\omega/\Delta P$ response across the entire pressure range, type-III modes with unique negative $\Delta\omega/\Delta P$ response, and lastly type-IV behavior where modes first possess negative $\Delta\omega/\Delta P$ but crossover to positive

values above $P_{critical}$. Raman modes of typical materials -including 2D material systems-, however, blue-shift monotonically upon application of pressure due to lattice stiffening effects. Such conventional stiffening response was also observed for most of the prominent optical modes (type II response) in the frequency range spanning from 100 to 450 cm^{-1} with positive and constant $\Delta\omega/\Delta P > 0$ values. Here, observed type-II behavior is a conventional response observed for most (if not all) material systems including 2D materials and will not be further discussed.

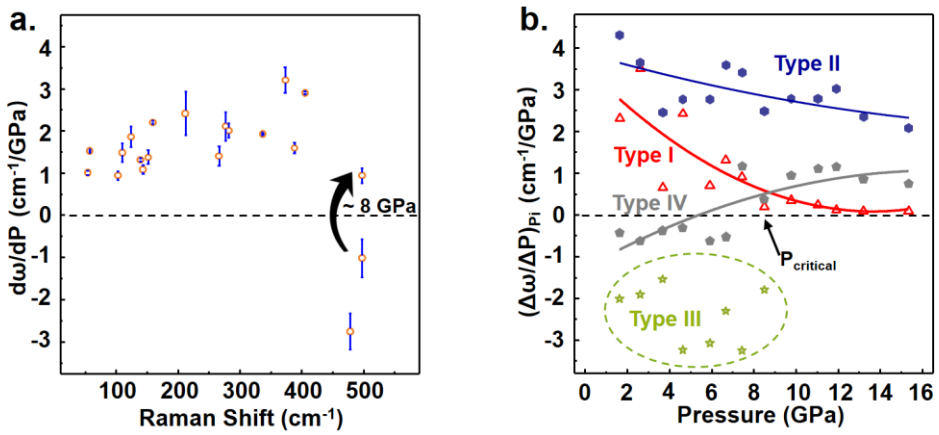

Figure 5.9 a. The fitted dω/dP values of all the Raman modes. b. Four types of characteristic pressure dependent Raman response represented by peaks located at ω_0 = 58 cm^{-1} for type I, ω_0 = 404 cm^{-1} for type II, ω_0 = 484 cm^{-1} for type III, and ω_0 = 498 cm^{-1} for type IV.

Unlike type-II response observed for optical Raman peaks, ultra-low frequency shear modes display positive but suturing pressure dependence (type I response). This is observed in the low-frequency regime (ω < 100 cm^{-1}) for shear modes located at $S_{\parallel}$ ~ 54 and $S_{\perp}$ ~ 58 cm^{-1}, while the modes at 77 and 88 cm^{-1} did not yield sufficient Raman signal to reach any conclusion. From ambient to 8.5 GPa, shear Eigen modes of $S_{\parallel}$ and $S_{\perp}$ both exhibit stiffening behavior with positive dω/dP values of 1.01 ± 0.06 and 1.52 ± 0.02 cm^{-}

^{1}/GPa, respectively. Since $S_{\perp}$ shear mode involves displacement perpendicular to Ta-chain, we attribute larger dω/dP value for $S_{\perp}$ to high sensitivity to applied hydrostatic pressure caused by larger interlayer coupling strength. Interestingly, however, these peaks remain nearly unchanged above $P_{critical}$~8.5 GPa, and dω/dP value thus the Gruneisen parameter ($-d\ln\omega/d\ln V=(\omega\chi_T)d\omega/dP$) approaches to zero. We note that type-IV modes at high frequencies exhibit negative to positive dω/dP crossover (**Figure 5.9a**) at similar hydrostatic pressure threshold ($P_{critical}$). These results will be discussed in greater detail later in the article. The type III behavior represented by the mode at ω_0 = 484 cm^{-1} gives negative values ranging from -1.5 to -3.2 cm^{-1}/GPa without any monotonic trend. Since 484 cm^{-1} peak involves sulfur-sulfur (S-S) atomic vibrations[109], increased pressure enhances the orbital interaction between atoms localized within adjacent layers, and effectively increases the distance (and coupling strength) between S-S by increasing the angle formed along S-Ta-S. We note that type-III peak at 484 cm^{-1} is not detectable above 8 GPa, thus this peak may also display negative to positive pressure coefficient cross-over. Interestingly, the type IV mode (ω_0 = 498 cm^{-1}) first displays negative pressure coefficient but crossover to positive above $P_{critical}$ ~ 8.5 GPa. Even though, this non-monotonic response is not fully understood, it is possible that two competing effects, namely S-S softening and interlayer stiffening responses, play a vital role in determining their overall pressure responses. At low pressures, S-S vibration softens due to reduction in interlayer spacing and consequent repulsion between S-S pairs. As the pressure is increased, second and third order interlayer coupling effects start to dominate the overall response with positive pressure dependence, giving overall non-monotonic response.

5.5. Loss of Raman anisotropy

The applied hydrostatic pressure has shown tremendous stiffening and softening effects on vibrational properties of pseudo-1D *o*-TaS_3, but how does the pressure influence its Raman anisotropy? Here, we define the degree of anisotropy (η) as the ratio between the maximum intensity over the minimum as $\eta_{\omega 0} = I_{\omega 0,\, max} / I_{\omega 0,\, min}$. This notation previously has been shown to be effective by our team as well as others in other systems. The peaks located at $\omega_0 = 54$ and 337 cm^{-1} have been selected to show this effect owing to their two-lobed features in the polar plots with the intensity maxima found either parallel or perpendicular to the chain direction (0° and 180°), and the polar plots for peak intensities in ambient, 5.9 GPa, and 11.0 GPa are given in **Figure 5.10a and 5.10b** where the intensity values are converted to a reader friendly natural logarithmic scale. It is noteworthy that the mode at $\omega_0 = 54$ cm^{-1} (**Figure 5.10a**) retain the two-lobed feature as well as the intensity maxima found along the chain direction, whereas the intensity minima found at 90° and 270° show obvious enhancement as pressure increases, indicating a reduced anisotropic Raman response. Similar response can be observed in the mode at $\omega_0 = 337$ cm^{-1} (**Figure 5.10b**) despite a 90° offset of the maximum intensity axis with respect to the chain direction. Therefore, the pressure effect on the degree of Raman anisotropy is consistent in these Raman modes regardless whether the intensity maxima are aligned parallel or perpendicular to the chain.

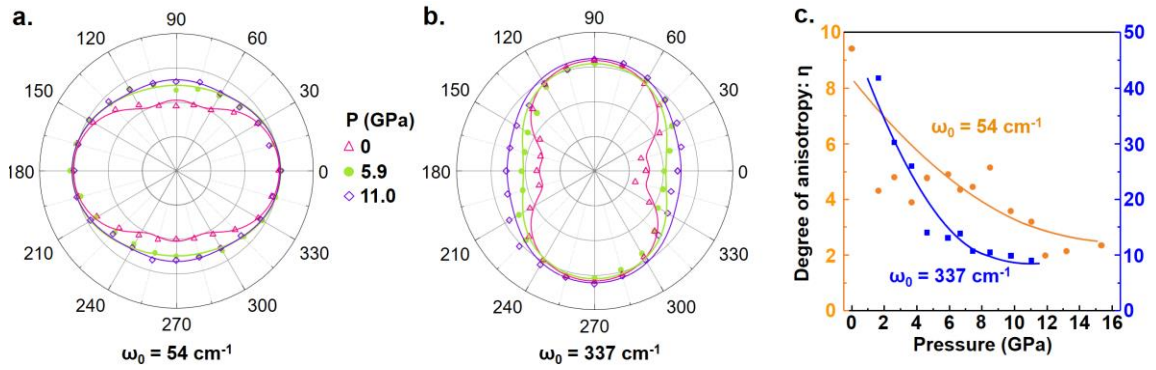

Figure 5.10 Logarithmic scale (radial axis is set to natural log for better assessment) angle-resolved Raman spectra (polar plots) measured at ambient, 5.9 GPa, and 11.0 GPa for Raman modes located at a. ω_0 = 54 and 337 cm^{-1} and b. ω_0 = 337 cm^{-1} with Raman intensity converted to reader friendly natural logarithmic scale. c. Losing the degree of anisotropy (η) as a function of pressure.

To further understand the pressure effect, we have also investigated degree of anisotropy (η) of these two modes as a function of pressure. As shown in **Figure 5.6c**, the η values of the ω_0 = 54 cm^{-1} mode is greatly reduced by ~ 70% in the entire pressure range, and the mode at ω_0 = 337 cm^{-1} also demonstrates a ~ 75 % drop in η with pressure increasing from ambient to 11.0 GPa. We argue that observed reduction in η values might be related to higher degree of coupling (stronger force constant) between neighboring pseudo-1D chains caused by applied hydrostatic applied pressure acting both in the *c*- and *b*-axis directions. However, further studies are necessary to shed light on fundamental mechanisms governing this phenomenon.

5.6. Conclusions

Our results introduce the very first detailed vibrational response of pseudo-1D TaS_3, and their structural and optical response to hydrostatic pressures through careful angle-

resolved Raman spectroscopy (ARS) and diamond anvil cell (DAC) studies. Our studies reveal four distinct responses that are vastly different from other isotropic 2D systems: (1) Systematic ARS measurements establish phonon vibration modes involving atomic vibrations along the chain direction and establish Raman intensity variation with the polarization direction, enabling us to identify anisotropy direction through ARS measurements. (2) TaS_3 under hydrostatic pressure display peak splitting at 3-4 GPa which is well below the pressure required for phase transition. This suggests that a variety of energetically degenerate Raman modes with different pressure coefficients ($d\omega/dP$) exist at atmospheric pressures. (3) Whist all Raman peaks stiffen ($d\omega/dP > 0$) with applied hydrostatic pressure, the high frequency peaks at $\omega_0 = 484$ cm^{-1} and 498 cm^{-1} exhibit previously unobserved non-monotonic behavior between 0 and 15.3 GPa. (4) Interestingly, the degree of anisotropy significantly decreases by ~ 70 % with applied pressure. Our systematic studies shed light on the origin of such anisotropic-to-isotropic crossover. This work not only marks the first investigation of the vibrational characteristics of pseudo-1D *o*-TaS_3, but also provides us with a valuable fundamental insight into their pressure dependent response of its novel Raman modes. Overall, findings significantly advance our understanding of their fundamental properties of pseudo-1D materials, and our interpretations on vibrational characteristics offer valuable insights that are related to their thermal, electrical, as well as optical properties.

Chapter 6 PHASE TRANSITION ACROSS ANISOTROPIC NIOBIUM TRISULFIDE AND TITANIUM TRISULFUIDE AT NOMINAL TITANIUM ALLOYING LIMIT

Alloying selected transitional metal trichalcogenides (TMTCs) offers the opportunities for structural, optical, and electrical engineering thus expands the regime of this class of pseudo-1D layered materials. In this chapter, we show novel phase transition effects in anisotropic $Nb_{(1-x)}Ti_xS_3$ ternary alloys. Through chemical vapor transport (CVT), energy-dispersive X-ray spectroscopy (EDS), Raman microscopy, transmission electron microscopy (TEM), and density functional theory (DFT) calculations, we have identified that high crystalline CVT grown $Nb_{(1-x)}Ti_xS_3$ are fully alloyed in the entire composition range without any phase separation / co-existing with a triclinic to monoclinic phase crossover. Surprisingly, incorporation of a small concentration of Ti (x ~ 0.05 - 0.18) into NbS_3 host matrix is sufficient to induce the phase transition. Theoretical studies suggest that Ti atoms effectively introduce n-type doping due to one less valance electron in Ti compared to Nb, which in return rapidly decreases the total energy of monoclinic phase and induces triclinic-monoclinic phase transition. When alloyed, crystalline and optical anisotropy are largely preserved as evidenced by HR-TEM and angle-resolved Raman spectroscopy measurement that offers fundamental insights into the degree of crystalline anisotropy in these alloys. Overall results introduce $Nb_{(1-x)}Ti_xS_3$ as a new and easy phase change material and mark the novel phase engineering in anisotropic van der Waals (vdW) trichalcogenide systems for their potential applications in 2D electronics, photonics, and in particular information technologies based on phase change materials.

6.1. Crystal structure

As discussed, titanium trisulfide (TiS_3) and niobium trisulfide (NbS_3) are quasi one-dimensional (1D) materials, and they retain 2D sheet as well as 1D chain-like structures. In-plane anisotropy from chain like features induce highly direction dependent properties[110-111]. Despite the similar chemical formula, TiS_3 and NbS_3 have essential distinctions in crystal structures, as shown in **Figure 6.1**.

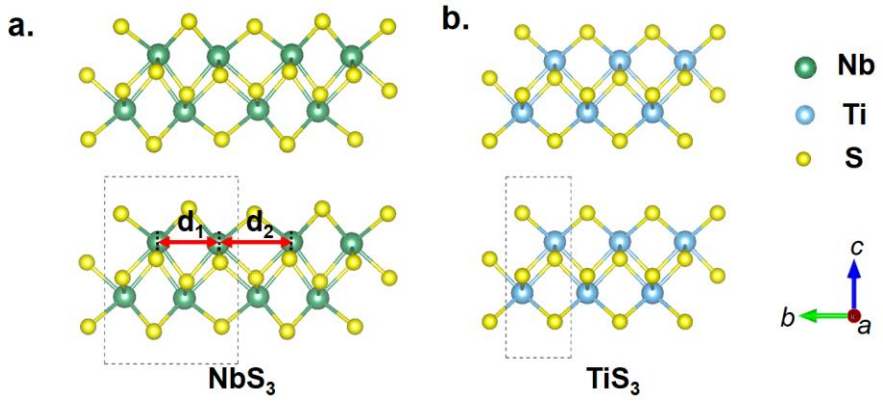

Figure 6.1 a. Schematic description of the crystal structure of a. triclinic NbS_3 and b. monoclinic TiS_3.

Specifically, TiS_3 crystallizes in the monoclinic structure with a = 4.98 Å, b = 3.39 Å and c = 8.89 Å, in which the metal atom (Ti) is surrounded by six sulfur atoms, forming bicapped distorted tetrahedrons. In contrast, however, NbS_3 undergoes linear Peierls distortion and forms alternating Nb-Nb pairs ($d_1 \approx$ 3.0 Å) and Nb-Nb gaps ($d_2 \approx$ 3.7 Å) along the chain direction (b-axis) due to a displacement of the Nb ions by 0.16 Å from the centers of the tetrahedrons[112]. As a result of the distortion, NbS_3 crystallizes in a triclinic phase with a doubling of the volume along the b-axis, and the lattice parameters of triclinic NbS_3 measure as a = 4.96 Å, b = 6.73 Å and c = 9.14 Å.

6.2. Crystal growth and characterization

Figure 6.2 As grown $Nb_{(1-x)}Ti_xS_3$ (x = 0.66) crystals on the interior wall of a quartz ampule.

We have utilized a CVT growth technique to synthesize a series of $Nb_{(1-x)}Ti_xS_3$ alloys with variable compositions ($0 \leq x \leq 1$) using elemental niobium, titanium and sulfur precursors. In a typical growth, silver shiny 1D-like whiskers were found on the interior wall of the quartz ampule as shown for $Nb_{(1-x)}Ti_xS_3$ (x = 0.66) crystals in **Figure 6.2.**

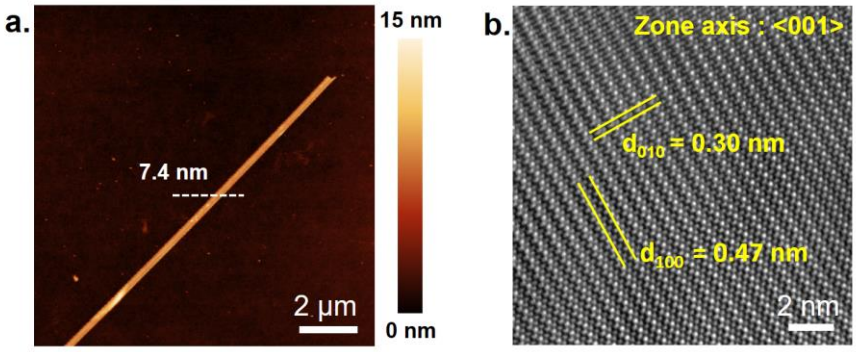

Figure 6.3 a. Atomic force microscopy (AFM) image of exfoliated $Nb_{0.34}Ti_{0.66}S_3$. b. High-resolution transmission electron microscopy (HR-TEM) image collected from $Nb_{0.34}Ti_{0.66}S_3$ alloy

The $Nb_{(1-x)}Ti_xS_3$ crystals can be exfoliated onto a 285 nm SiO_2/Si substrate and the atomic force microscopy (AFM) image of the exemplary $Nb_{0.34}Ti_{0.66}S_3$ nanoribbon studied in this work is shown in **Figure 6.2a**, which clearly shows the large geometric anisotropy and layered nature of this material. **Figure 6.2b** shows the HR-TEM image measured on $Nb_{0.34}Ti_{0.66}S_3$ and the d(100) and d(010) measure 0.47 nm and 0.30 nm, respectively. In agreement with the geometrical anisotropy in the AFM image, the TEM image also shows metal chains extending along the *b*-axis in **Figure 6.2b**. The SEM (**Figure 3a**) and EDS mapping images (**Figure 3b - 3c**) were performed on as-grown $Nb_{0.34}Ti_{0.66}S_3$ crystals and the results show homogeneous spatial distribution of the Nb, Ti, and S elements

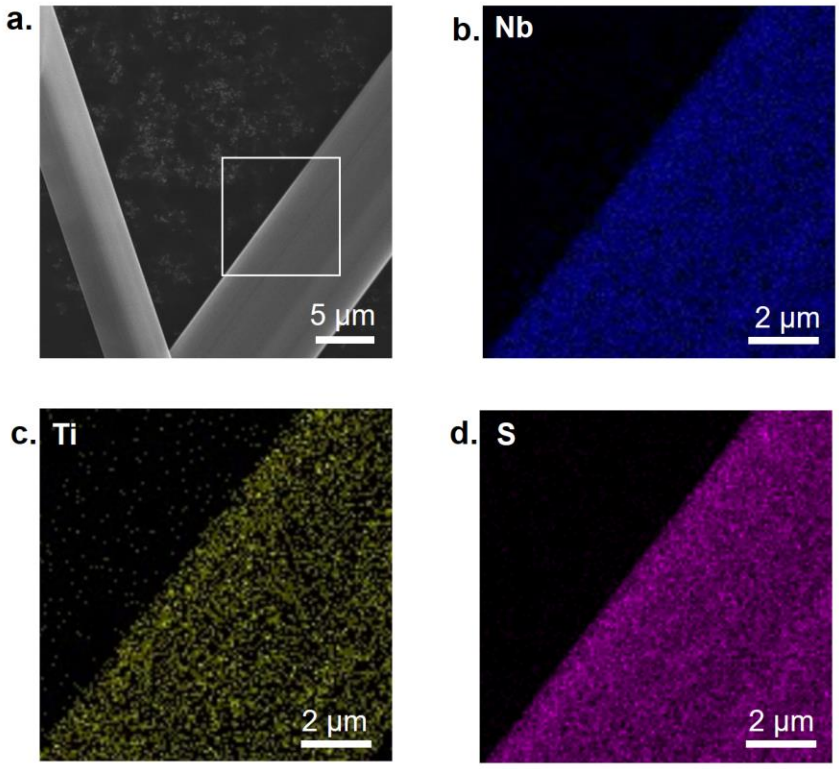

Figure 6.4 a. The scanning electron microscopy (SEM) image taken from $Nb_{0.34}Ti_{0.66}S_3$ whiskers and Energy-dispersive X-ray spectroscopy (EDS) elemental mapping of b. Nb, c. Ti, and d. S element.

Previously, it has been shown that the presence of point defects as well as alloyed atoms introduce crystal potential variations and nanoscale strain in Re-based TMDCs and $ReS_{2(1-x)}Se_{2x}$ alloys energetically, which stabilizes new isotropic phases, and reduces the degree of crystalline anisotropy. Our measurements show that alloying Ti atoms into NbS_3 does not sacrifice the crystalline anisotropy of $Nb_{(1-x)}Ti_xS_3$ ($0 \leq x \leq 1$) material.

6.3. Phase transition at nominal titanium alloying limit

In this section, we provide answers to how the crystal structure and symmetry change in this $Nb_{(1-x)}Ti_xS_3$ alloy system as the Ti atomic concentration (x) is varied from 0 to 1.

Here, the atomic ratio of Ti and Nb elements was estimated by energy-dispersive X-ray spectroscopy (EDS) as shown in **Figure 6.5**, and the Ti concentration (*x*) were found to be 0, 0.05, 0.18, 0.24, 0.41, 0.66, 0.87, and 1.

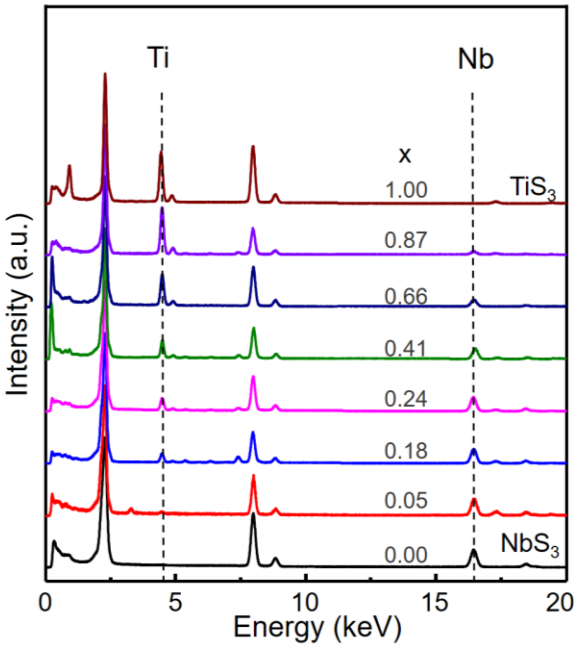

Figure 6.5 Energy-dispersive X-ray spectroscopy (EDS) of $Nb_{(1-x)}Ti_xS_3$ ternary alloys.

The transmission electron microscopy (TEM) and selected area electron diffraction (SAED) analysis have been performed on $Nb_{(1-x)}Ti_xS_3$ alloy at the above *x* values as shown in **Figure 6.6a-h**. A closer look at the figure shows that each of these alloys are well-crystallized as evidenced by clear and sharp diffraction patterns. At a given composition (*x* value), there is only one unique diffraction pattern without any secondary faint pattern, which suggests that crystallized alloys are not phase separated. Further fast Fourier transform (FFT) of high-resolution TEM images shows no secondary spots indicating no phase separation even at nanoscale.

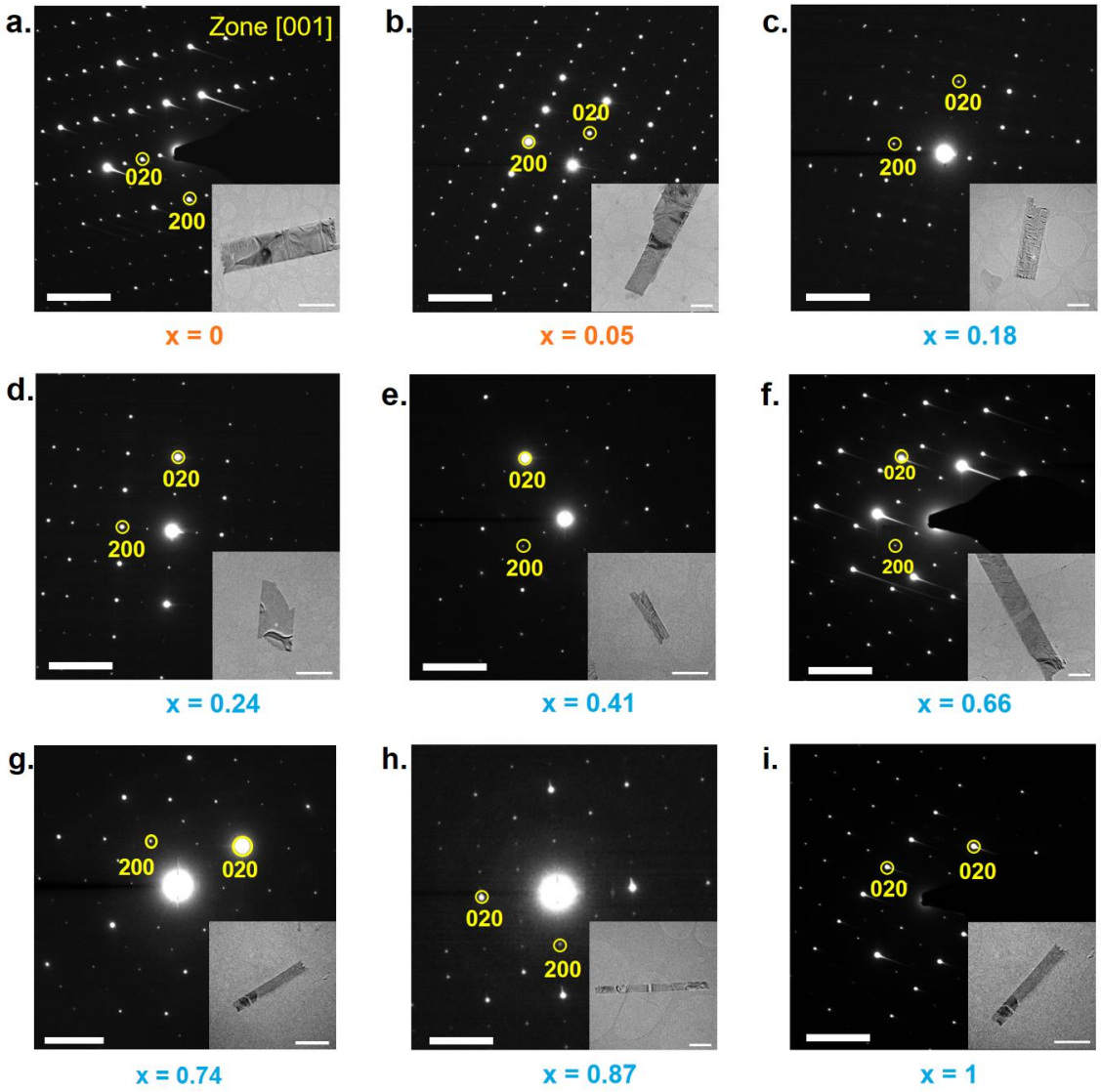

Figure 6.6 Transmission electron microscopy (TEM) and selected area electron diffraction (SAED) pattern $Nb_{(1-x)}Ti_xS_3$ alloys of selected compositions. a. $x = 0$ (NbS_3), b. $x = 0.05$, c. $x = 0.18$, d. $x = 0.24$, e. $x = 0.41$, f. $x = 0.66$, g. $x = 0.74$, h. $x = 0.87$ i. $x = 1$ (TiS_3). Scale bar in the SAED: 5 1/nm; scale bar in the TEM images: 1 μm.

In our measurements, the zone axis was carefully tilted and aligned along [001] direction during the measurement, and diffraction of the (020) and (200) planes were indexed for each of the samples. In agreement with the distinctions in the crystal structures, the d(010) of NbS_3 (**Figure 6.8a**) measures 6.42 Å whereas the d(010) of TiS_3

(**Figure 6.8h**) measures 3.23 Å, indicating the doubling of the *b*-axis of triclinic NbS_3 compared with monoclinic TiS_3. Thus, identifying the composition range in which the *b*-axis doubling exists by comparing the d(010) values across the full alloy range becomes an effective method of providing crystal structure and symmetry information.

More importantly, the observed triclinic crystal structure for NbS_3 changes to monoclinic phase at very small titanium concentrations near x~0.05-0.18 as shown in **Figure 6.6b-c**. Since only a small amount of Ti is needed to cause phase transition, experimental results alone suggest that the triclinic and monoclinic phases are already close in total energies. Since the reduced crystal symmetry and the doubling of the *b*-axis of NbS_3 can be attributed to the Peierls distortion (Nb contains an extra valance electron compared with Ti), the equilibrium of the distortion and the stability of the triclinic structure can possibly be disturbed/lifted with the Ti content (x). We argue that incorporation of Ti into NbS_3 increases the total energy of triclinic phase and stabilizes monoclinic phase at a critical Ti composition range. This can also be pictured as p-type electronic doping induced phase transition since Ti has one less valence electron compared to Nb. These arguments will be further discussed and explained from theoretical perspective later.

The d(010) and d(100) values across the $Nb_{(1-x)}Ti_xS_3$ alloys measured by SAED are shown in **Figure 6.8a**. At a minimal Ti content (x = 0.05), the d (010) measures 6.45 Å which is same as NbS_3 (6.45 Å) demonstrating the doubling of *b*-axis and the triclinic nature of this alloy ($Nb_{0.95}Ti_{0.05}S_3$). This d(010) distance significantly drops by 50% down to 3.22 Å at x=0.18 ($Nb_{0.82}Ti_{0.18}S_3$) in agreement with previous discussions, and ranges from 3.04 to 3.26 Å as x is increased to 1.0. Meanwhile, the d (100) spacing of the

alloys measures 4.63 ± 0.09 Å which falls between that of measured NbS_3 (4.60 Å) and TiS_3 (4.67 Å). Interestingly, the d(001) spacing of the $Nb_{(1-x)}Ti_xS_3$ alloys measured by XRD (**Figure 6.7**)follows almost linearly with the EDS estimated composition as described by $d(100)_x = 9.07 - 0.36x$ Å, $0 \leq x \leq 1$. Therefore, XRD technique provides us with a quick and non-destructive method to estimate the composition without the complexity of electron microscopy.

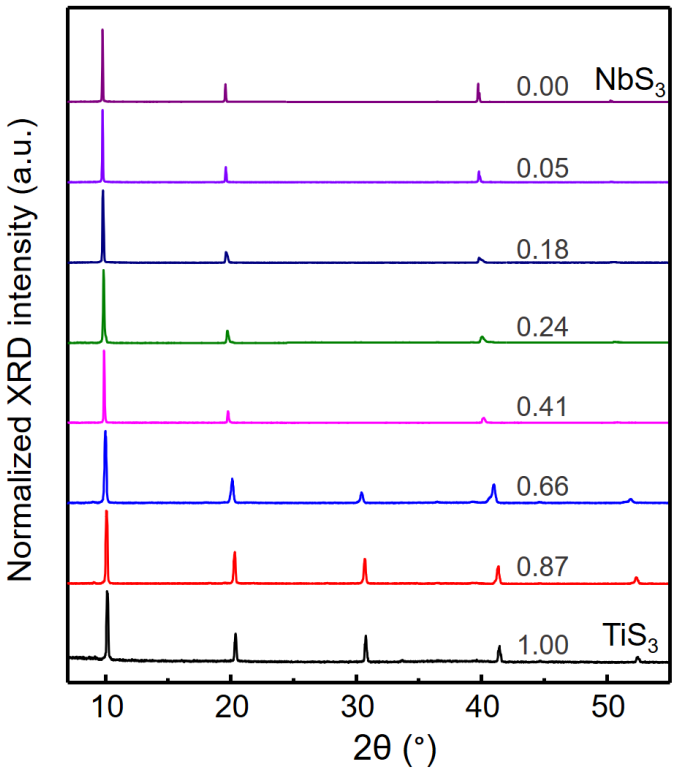

Figure 6.7 XRD patterns of of $Nb_{(1-x)}Ti_xS_3$ ternary alloys.

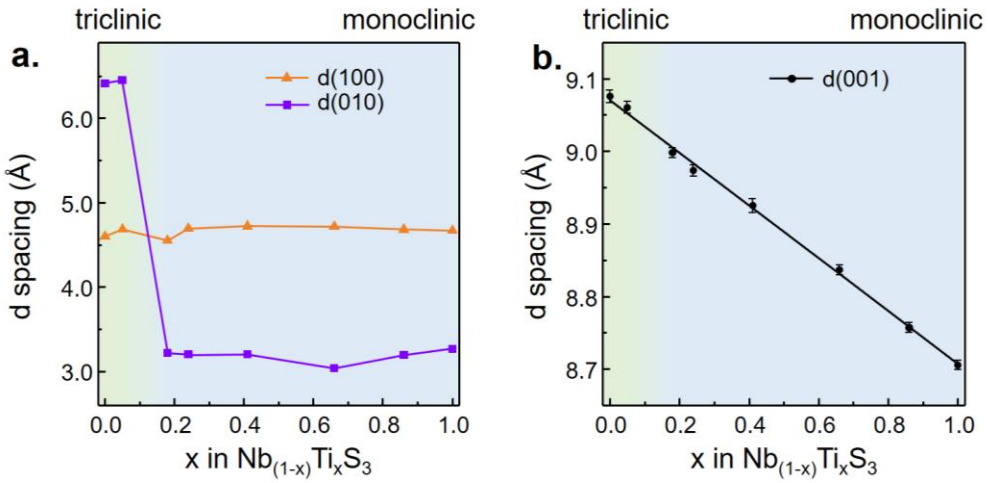

Figure 6.8 a. The d (100) and d (010) values of selected $Nb_{(1-x)}Ti_xS_3$ alloys obtained from the SEAD measurements. b. The d (100) values of selected $Nb_{(1-x)}Ti_xS_3$ alloys obtained from the XRD measurements preformed on as-grown $Nb_{(1-x)}Ti_xS_3$ crystals.

In summary, results suggest that (*i*) the alloys across the full composition range are accessible without a forbidden range or a phase coexistence / separation region, (*ii*) triclinic to monoclinic phase crossover takes place at a low Ti range ($0.05 < x < 0.18$), and alloys stabilize in triclinic structure at $0 \leq x \leq 0.05$ but form monoclinic phase at $0.18 \leq x \leq 1$; (*iii*) as the Ti starts to alloy into NbS_3 (replacing Nb atoms), the equilibrium of linear Peierls distortion is broken thus the metal-metal pairs and gaps disappear, rendering the crystal structure to monoclinic with higher symmetry.

6.4. Theoretical insights into the phase transition

To further investigate the structural evolution, we have performed density functional theory calculations (see experimental session) of the formation energy (E_F) of both triclinic (red triangles) and monoclinic (blue squares) phases of the $Nb_{(1-x)}Ti_xS_3$ alloys at different Ti content as shown in **Figure 6.9a**. Results show that initially NbS_3 (x = 0) and

TiS_3 (x = 1) stabilizes in triclinic and monoclinic phases by showing a lower formation energy, respectively. As the titanium composition increase, the formation energy of these two phases intersect with each other at a Ti content of x = 0.20, indicating the stabilization of the monoclinic phase when x is greater than 0.20. A closer look at the formation energy difference (**Figure 6.9a inset)** shows that the phase crossover takes place at an x range of 0.125 to 0.250, which is consistent with the experimental observed value of 0.05 to 0.18. Combining the experimental and theatrically results, we thus narrow down the phase cross over range to $0.12 < x < 0.18$.

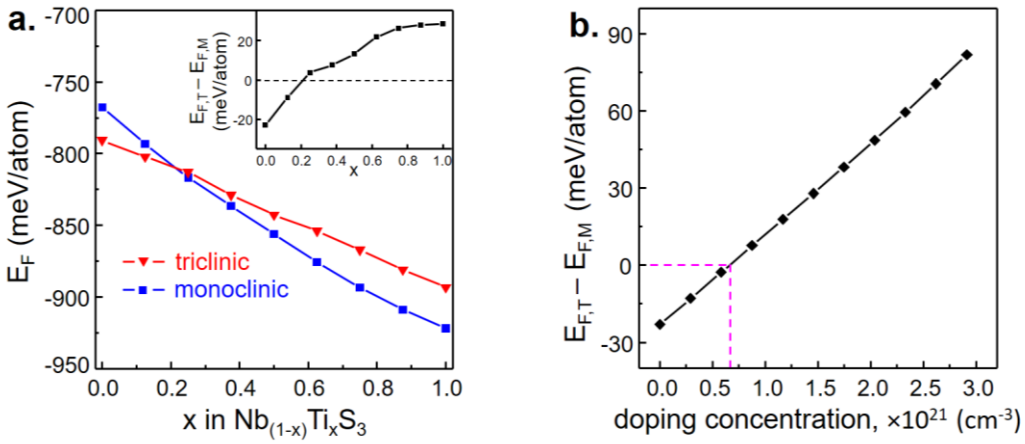

Figure 6.9 A comparison of the formation energy (E_F) of the $Nb_{(1-x)}Ti_xS_3$ alloys crystalized in triclinic ($E_{F,T}$) and monoclinic ($E_{F,M}$) phase and (inset) the difference in the formation energy ($E_{F,T}$ - $E_{F,M}$) b. The difference in formation energy of triclinic NbS_3 ($E_{F,T}$) vs monoclinic NbS_3 ($E_{F,M}$) showing the triclinic to monoclinic phase cross-over of NbS_3 at a p-type doping concentration of 0.7×10^{21} cm^{-3}.

As discussed above, the origin of the phase transition of the alloy system lies in the one less valance electron in Ti compared with Nb, which is comparable to the effect of p-type doping in the maternal NbS_3 crystals. How does this p-type doping affect the Peierls distortion and phase stability in NbS_3? We have calculated the formation energy of NbS_3

crystallized in both triclinic ($E_{F,T}$) and monoclinic ($E_{F,M}$) phase as a function of p-type doping concentration and the energetic difference ($E_{F,T}$ - $E_{F,M}$) is shown in **Figure 6.9b**. We note that a p-type doping of 6×10^{20} cm^{-3} is required to switch the triclinic NbS_3 to monoclinic phase, which is tough to be achieved in traditional semiconductor processing. However, in the 2D regime, this doping concentration is brought down to 7.7×10^{13} cm^{-2} for NbS_3 and can be reduced even lower for Nb-rich triclinic $Nb_{(1-x)}Ti_xS_3$ alloys, which is accessible through electrostatic doping and warrants further studies.

6.5. Vibrational characteristics during phase transition

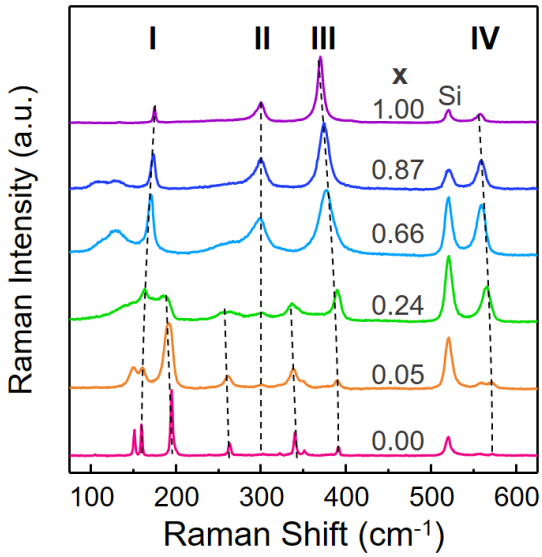

Figure 6.10 The Raman spectra of selected $Nb_{(1-x)}Ti_xS_3$ alloys.

The vibrational properties of triclinic NbS_3 and monoclinic TiS_3 are largely different due to their structural differences. Monoclinic TiS_3 ($P2_1/m$) contains two Ti and six S atoms in the primitive unit cell and its phonon dispersion yields 24 vibrational modes ($\Gamma = 8A_g + 4B_g + 4A_u + 8B_u$) at the center of the Brillouin zone with $8A_g + 4B_g$ Raman

active modes[113]. Triclinic NbS_3 ($P\bar{1}$) has 48 vibrational modes ($\Gamma = 24A_g + 24A_u$) (24 of which are Raman active modes) due to volume doubling of the unit cell, and thus NbS_3 displays more complex Raman spectra[114] compared with TiS_3. This, in return, enables us to further investigate the effects of 2D alloying on the structural and vibrational properties of these vdW crystals. Overall, Raman spectra collected for 2D alloys show gradual transition from NbS_3 to TiS_3 as shown in **Figure 6.10**.

TiS_3 displays four prominent Raman modes at 176 cm^{-1} (A_g^{rigid} mode), 298 cm^{-1} ($A_g^{internal}$ mode), 370 cm^{-1}($A_g^{internal}$ mode), and 556 cm^{-1} (A_g^{s-s} mode) consistent with earlier findings. Considering rich Raman spectrum (with many low intensity Raman peaks), we focus on the most prominent four modes from NbS_3 that are also found to be related and active in TiS_3 and their alloys. Specifically, the mode I at 159 cm^{-1} represents the Nb - Nb stretching mode. The weak peaks at 301 and 322 cm^{-1} can be attributed to Nb - S intrachain vibration (mode II), and the mode III at 380 and 392 cm^{-1} are Nb - S interchain vibration. The two peaks at 557 and 572 cm^{-1} originate from S - S pair oscillation. It is noteworthy that for TiS_3, the mode II ($A_g^{internal}$) at 298 cm^{-1} and the mode IV (A_g^{s-s}) at 556 cm^{-1} both consist of two energetically degenerate phonon branches located at the same frequency. For NbS_3, however, the degeneracy is absent in NbS_3 due to reduced crystal symmetry and a more complex Raman tensor, thus mode II – IV each consists of two distinct peaks.

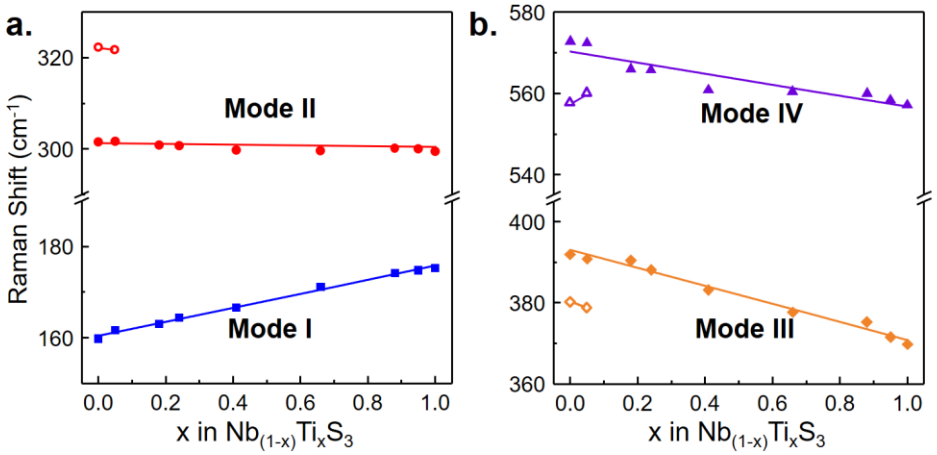

Figure 6.11 Raman peak position across the alloy range of a. mode I and mode II, b. mode III and mode IV.

As titanium concentration (x) increases, Raman peak position of mode I related to rigid chain vibrations blue shifts from 159 cm^{-1} in NbS_3 to 176 cm^{-1} as shown in **Figure 6.11a**. This can be attributed to reduced atomic mass going from Nb to Ti that increases the overall vibration frequency. In contrast, mode III and mode IV (**Figure 6.11b**) red shift (soften) with increasing x. Since these two modes involve out-of-plane atomic vibrations (unlike mode I which involves entire MX_3 rigid chain translation), interaction (oscillator) strength between transition metal and chalcogen (M-X) play a vital role in determining the peak position. We argue that the M-X oscillator strength reduces going from Nb to Ti due to much lower Bohr radius of Ti and less orbital overlap between M-X atoms which in return softens modes III and IV. Interestingly, the peak position of mode II almost remains unchanged possibly due competition between the reduced atomic mass and orbit overlapping effects.

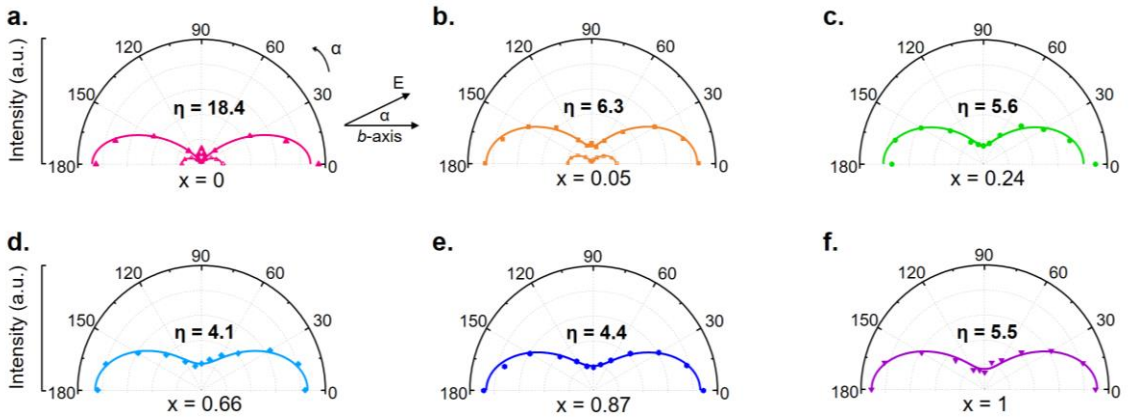

Figure 6.12 Angle-dependent Raman intensity (polar plots) of mode III in selected $Nb_{(1-x)}Ti_xS_3$ alloys where α shows the angle between b-axis and excitation laser; η represents the degree of anisotropy defined by $\eta = I_{max}/I_{min}$. Green laser (λ = 532 nm) was used as the excitation source. *x* = 0, 0.05, 0.24, 0.66, 0.87, 1.0

Lastly, we discuss the structural anisotropy effects in $Nb_{(1-x)}Ti_xS_3$ trichalcogenide alloys. Previously, angle resolved Raman spectroscopy measurements have been successfully utilized to provide the fundamental understanding of the structural anisotropy in 2D anisotropic material systems. However, this method has not been applied to 2D alloys, especially in trichalcogenides, and thus angle resolved measurements are required to understand if these measurements still offer an effective method to assess crystalline anisotropy in trichalcogenide alloys. Careful measurements performed on $Nb_{(1-x)}Ti_xS_3$ nanoribbons reveal that mode III can be used as a reference across the entire alloying composition range to determine the crystalline anisotropy direction (**Figure 6.12**). Raman intensity of mode III reaches to a maximum when the polarization field aligns parallel to the geometrical (*b-axis*) which corresponds to the MX_3 chain direction. Meanwhile, we relate the degree of crystalline anisotropy (meaning how well chains are aligned with respect to each other) to Raman anisotropy ratio (η)

which can be described as $\eta = I_{max}/I_{min}$ where I_{max} and I_{min} corresponds to the Raman intensity maximum and minimum in the polar plots. These plots enable us to understand the anisotropic nature of the alloys for any *x* value. The η value is particularly maximized at *x*=0 (NbS_3) which means that MX_3 chains are well-aligned with respect to each other. In contrast, 2D alloyed $Nb_{(1-x)}Ti_xS_3$ samples and even TiS_3 exhibit η values around 5-6 which is smaller than Peierls distorted NbS_3 crystals. η value drops from 18.4 for NbS_3 (*x* = 0) to 6.3 for $Nb_{0.95}Ti_{0.05}S_3$ at a minimal Ti content (*x* = 0.05) which suggests that the introduction of these point defects (Ti substitutes) potentially cause MX_3 chains to change their propagation direction. This effect has been previously demonstrated for anisotropic ReS_2 monolayers and is consistent with our findings. After the phase crossover point, η further reduces to η = 4.1 for $Nb_{0.34}Ti_{0.66}S_3$ (*x* = 0.66) until in the Ti-rich alloys (**Figure 6.12d-f**), the Raman anisotropy is gradually recovered to 4.4 for $Nb_{0.13}Ti_{0.87}S_3$ (*x* = 0.87) and 5.5 for TiS_3 (x = 1), respectively. The overall findings suggest that angle resolved measurements can be used to assess chain propagation direction as well as the degree of crystalline anisotropy.

6.6. Conclusions

Overall results mark a variety of findings in this newly developing 2D anisotropic trichalcogenide community, and further offer fundamental insights when materials with vastly different electronic properties and structural characteristics are alloyed. Demonstrated synthesis shows that full alloying across the entire composition range can be attained to synthesize $Nb_{(1-x)}Ti_xS_3$ alloys without any phase separation. Electron microscopy, x-ray diffraction, and angle resolved Raman spectroscopy measurements

show that small amount of Ti incorporation into NbS_3 induces triclinic to monoclinic phase transition. Theoretical studies suggest the phase transition can be attributed to increase in total energy of triclinic phase by p-type doping induced by Ti atoms which contain one less valance electron compared to Nb. Detailed Raman measurements provide further insights into structural and vibrational characteristics of $Nb_{(1-x)}Ti_xS_3$ alloys, and enable us to investigate how structural anisotropy is influenced by the alloying effects. Overall results mark the first phase engineering in anisotropic vdW trichalcogenide systems for their potential applications in 2D superconductivity, electronics, and photonics.

REFERENCES

1. Bhimanapati, G. R.; Lin, Z.; Meunier, V.; Jung, Y.; Cha, J.; Das, S.; Xiao, D.; Son, Y.; Strano, M. S.; Cooper, V. R.; Liang, L.; Louie, S. G.; Ringe, E.; Zhou, W.; Kim, S. S.; Naik, R. R.; Sumpter, B. G.; Terrones, H.; Xia, F.; Wang, Y.; Zhu, J.; Akinwande, D.; Alem, N.; Schuller, J. A.; Schaak, R. E.; Terrones, M.; Robinson, J. A., Recent Advances in Two-Dimensional Materials beyond Graphene. *ACS Nano* **2015,** *9* (12), 11509-39.

2. Yazyev, O. V.; Chen, Y. P., Polycrystalline graphene and other two-dimensional materials. *Nat Nanotechnol* **2014,** *9* (10), 755-67.

3. Novoselov, K. S.; Geim, A. K.; Morozov, S. V.; Jiang, D.; Zhang, Y.; Dubonos, S. V.; Grigorieva, I. V.; Firsov, A. A., Electric field effect in atomically thin carbon films. *science* **2004,** *306* (5696), 666-669.

4. Jariwala, D.; Sangwan, V. K.; Lauhon, L. J.; Marks, T. J.; Hersam, M. C., Emerging device applications for semiconducting two-dimensional transition metal dichalcogenides. *ACS Nano* **2014,** *8* (2), 1102-20.

5. Tongay, S.; Suh, J.; Ataca, C.; Fan, W.; Luce, A.; Kang, J. S.; Liu, J.; Ko, C.; Raghunathanan, R.; Zhou, J.; Ogletree, F.; Li, J.; Grossman, J. C.; Wu, J., Defects activated photoluminescence in two-dimensional semiconductors: interplay between bound, charged, and free excitons. *Sci Rep* **2013,** *3*, 2657.

6. You, Y.; Zhang, X.-X.; Berkelbach, T. C.; Hybertsen, M. S.; Reichman, D. R.; Heinz, T. F., Observation of biexcitons in monolayer WSe2. *Nature Physics* **2015,** *11* (6), 477-481.

7. Chernikov, A.; Berkelbach, T. C.; Hill, H. M.; Rigosi, A.; Li, Y.; Aslan, O. B.; Reichman, D. R.; Hybertsen, M. S.; Heinz, T. F., Exciton binding energy and nonhydrogenic Rydberg series in monolayer WS(2). *Phys Rev Lett* **2014,** *113* (7), 076802.

8. Conley, H. J.; Wang, B.; Ziegler, J. I.; Haglund, R. F., Jr.; Pantelides, S. T.; Bolotin, K. I., Bandgap engineering of strained monolayer and bilayer MoS2. *Nano Lett* **2013,** *13* (8), 3626-30.

9. Kim, S. J.; Choi, K.; Lee, B.; Kim, Y.; Hong, B. H., Materials for flexible, stretchable electronics: Graphene and 2D materials. *Annual Review of Materials Research* **2015,** *45*, 63-84.

10. Mak, K. F.; He, K.; Shan, J.; Heinz, T. F., Control of valley polarization in monolayer MoS2 by optical helicity. *Nat Nanotechnol* **2012,** *7* (8), 494-8.

11. Xiao, D.; Liu, G.-B.; Feng, W.; Xu, X.; Yao, W., Coupled spin and valley physics in monolayers of MoS 2 and other group-VI dichalcogenides. *Physical Review Letters* **2012,** *108* (19), 196802.

12. Zeng, H.; Dai, J.; Yao, W.; Xiao, D.; Cui, X., Valley polarization in MoS2 monolayers by optical pumping. *Nat Nanotechnol* **2012,** *7* (8), 490-3.

13. Radisavljevic, B.; Radenovic, A.; Brivio, J.; Giacometti, V.; Kis, A., Single-layer MoS2 transistors. *Nat Nanotechnol* **2011,** *6* (3), 147-50.

14. Akinwande, D.; Petrone, N.; Hone, J., Two-dimensional flexible nanoelectronics. *Nature communications* **2014,** *5*.

15. Chen, Y.; Tan, C.; Zhang, H.; Wang, L., Two-dimensional graphene analogues for biomedical applications. *Chemical Society Reviews* **2015,** *44* (9), 2681-2701.

16. Novoselov, K.; Geim, A. K.; Morozov, S.; Jiang, D.; Katsnelson, M.; Grigorieva, I.; Dubonos, S.; Firsov, A., Two-dimensional gas of massless Dirac fermions in graphene. *nature* **2005,** *438* (7065), 197-200.

17. Geim, A. K., Graphene: status and prospects. *science* **2009,** *324* (5934), 1530-1534.

18. Balandin, A. A.; Ghosh, S.; Bao, W.; Calizo, I.; Teweldebrhan, D.; Miao, F.; Lau, C. N., Superior thermal conductivity of single-layer graphene. *Nano letters* **2008,** *8* (3), 902-907.

19. Neto, A. C.; Guinea, F.; Peres, N. M.; Novoselov, K. S.; Geim, A. K., The electronic properties of graphene. *Reviews of modern physics* **2009,** *81* (1), 109.

20. Lin, M.-W.; Ling, C.; Zhang, Y.; Yoon, H. J.; Cheng, M. M.-C.; Agapito, L. A.; Kioussis, N.; Widjaja, N.; Zhou, Z., Room-temperature high on/off ratio in suspended graphene nanoribbon field-effect transistors. *Nanotechnology* **2011,** *22* (26), 265201.

21. Balog, R.; Jørgensen, B.; Nilsson, L.; Andersen, M.; Rienks, E.; Bianchi, M.; Fanetti, M.; Lægsgaard, E.; Baraldi, A.; Lizzit, S., Bandgap opening in graphene induced by patterned hydrogen adsorption. *Nature materials* **2010,** *9* (4), 315-319.

22. Wilson, J.; Yoffe, A., The transition metal dichalcogenides discussion and interpretation of the observed optical, electrical and structural properties. *Advances in Physics* **1969,** *18* (73), 193-335.

23. Chen, Y.; Xi, J.; Dumcenco, D. O.; Liu, Z.; Suenaga, K.; Wang, D.; Shuai, Z.; Huang, Y.-S.; Xie, L., Tunable band gap photoluminescence from atomically thin transition-metal dichalcogenide alloys. *Acs Nano* **2013,** *7* (5), 4610-4616.

24. Komsa, H.-P.; Krasheninnikov, A. V., Two-Dimensional Transition Metal Dichalcogenide Alloys: Stability and Electronic Properties. *The Journal of Physical Chemistry Letters* **2012,** *3* (23), 3652-3656.

25. Wang, Q.; Kalantar-Zadeh, K.; Kis, A.; Coleman, J. N.; Strano, M. S., Electronics and optoelectronics of two-dimensional transition metal dichalcogenides. *Nature Nanotechnology* **2012,** *7* (11), 699-712.

26. Mak, K. F.; Lee, C.; Hone, J.; Shan, J.; Heinz, T. F., Atomically thin MoS 2: a new direct-gap semiconductor. *Physical Review Letters* **2010,** *105* (13), 136805.

27. Tongay, S.; Zhou, J.; Ataca, C.; Lo, K.; Matthews, T. S.; Li, J.; Grossman, J. C.; Wu, J., Thermally driven crossover from indirect toward direct bandgap in 2D semiconductors: MoSe2 versus MoS2. *Nano letters* **2012,** *12* (11), 5576-5580.

28. Gutiérrez, H. R.; Perea-López, N.; Elías, A. L.; Berkdemir, A.; Wang, B.; Lv, R.; López-Urías, F.; Crespi, V. H.; Terrones, H.; Terrones, M., Extraordinary room-temperature photoluminescence in triangular WS2 monolayers. *Nano letters* **2012,** *13* (8), 3447-3454.

29. Ghatak, S.; Pal, A. N.; Ghosh, A., Nature of electronic states in atomically thin MoS2 field-effect transistors. *Acs Nano* **2011,** *5* (10), 7707-7712.

30. Late, D. J.; Liu, B.; Matte, H. R.; Dravid, V. P.; Rao, C., Hysteresis in single-layer MoS2 field effect transistors. *Acs Nano* **2012,** *6* (6), 5635-5641.

31. Geim, A. K.; Grigorieva, I. V., Van der Waals heterostructures. *Nature* **2013,** *499* (7459), 419-425.

32. Yu, W. J.; Liu, Y.; Zhou, H.; Yin, A.; Li, Z.; Huang, Y.; Duan, X., Highly efficient gate-tunable photocurrent generation in vertical heterostructures of layered materials. *Nature nanotechnology* **2013,** *8* (12), 952-958.

33. Hong, X.; Kim, J.; Shi, S.-F.; Zhang, Y.; Jin, C.; Sun, Y.; Tongay, S.; Wu, J.; Zhang, Y.; Wang, F., Ultrafast charge transfer in atomically thin MoS2/WS2 heterostructures. *Nature Nanotechnology* **2014,** *9* (9), 682-686.

34. Tongay, S.; Suh, J.; Ataca, C.; Fan, W.; Luce, A.; Kang, J. S.; Liu, J.; Ko, C.; Raghunathanan, R.; Zhou, J., Defects activated photoluminescence in two-dimensional semiconductors: interplay between bound, charged, and free excitons. *Scientific reports* **2013,** *3*, 2657.

35. Mayorov, A. S.; Gorbachev, R. V.; Morozov, S. V.; Britnell, L.; Jalil, R.; Ponomarenko, L. A.; Blake, P.; Novoselov, K. S.; Watanabe, K.; Taniguchi, T., Micrometer-scale ballistic transport in encapsulated graphene at room temperature. *Nano letters* **2011,** *11* (6), 2396-2399.

36. Qiao, J.; Kong, X.; Hu, Z.-X.; Yang, F.; Ji, W., High-mobility transport anisotropy and linear dichroism in few-layer black phosphorus. *Nature communications* **2014,** *5*.

37. Tongay, S.; Sahin, H.; Ko, C.; Luce, A.; Fan, W.; Liu, K.; Zhou, J.; Huang, Y.-S.; Ho, C.-H.; Yan, J., Monolayer behaviour in bulk ReS2 due to electronic and vibrational decoupling. *Nature communications* **2014,** *5*.

38. Chenet, D. A.; Aslan, O. B.; Huang, P. Y.; Fan, C.; van der Zande, A. M.; Heinz, T. F.; Hone, J. C., In-plane anisotropy in mono-and few-layer ReS2 probed by Raman spectroscopy and scanning transmission electron microscopy. *Nano letters* **2015,** *15* (9), 5667-5672.

39. He, R.; Yan, J.-A.; Yin, Z.; Ye, Z.; Ye, G.; Cheng, J.; Li, J.; Lui, C. H., Coupling and stacking order of ReS2 atomic layers revealed by ultralow-frequency Raman spectroscopy. *Nano letters* **2016,** *16* (2), 1404-1409.

40. Joshua, O. I.; Aday, J. M.-M.; Mariam, B.; Robert, B.; Eduardo, F.; José, M. C.; José, R. A.; Carlos, S.; Herre, S. J. v. d. Z.; Roberto, D. A.; Isabel, J. F.; Andres, C.-G., Electronics and optoelectronics of quasi-1D layered transition metal trichalcogenides. *2D Mat.* **2017,** *4* (2), 022003.

41. Li, L.; Yu, Y.; Ye, G. J.; Ge, Q.; Ou, X.; Wu, H.; Feng, D.; Chen, X. H.; Zhang, Y., Black phosphorus field-effect transistors. *Nature nanotechnology* **2014,** *9* (5), 372-377.

42. Xia, F.; Wang, H.; Jia, Y., Rediscovering black phosphorus as an anisotropic layered material for optoelectronics and electronics. *Nature communications* **2014,** *5*.

43. Wang, X.; Jones, A. M.; Seyler, K. L.; Tran, V.; Jia, Y.; Zhao, H.; Wang, H.; Yang, L.; Xu, X.; Xia, F., Highly anisotropic and robust excitons in monolayer black phosphorus. *Nature nanotechnology* **2015,** *10* (6), 517.

44. Ling, X.; Huang, S.; Hasdeo, E. H.; Liang, L.; Parkin, W. M.; Tatsumi, Y.; Nugraha, A. R.; Puretzky, A. A.; Das, P. M.; Sumpter, B. G., Anisotropic Electron-Photon and Electron-Phonon Interactions in Black Phosphorus. *Nano letters* **2016,** *16* (4), 2260-2267.

45. Dai, J.; Zeng, X. C., Titanium Trisulfide Monolayer: Theoretical Prediction of a New Direct-Gap Semiconductor with High and Anisotropic Carrier Mobility. *Angewandte Chemie International Edition* **2015,** *54* (26), 7572-7576.

46. Island, J. O.; Buscema, M.; Barawi, M.; Clamagirand, J. M.; Ares, J. R.; Sánchez, C.; Ferrer, I. J.; Steele, G. A.; van der Zant, H. S.; Castellanos-Gomez, A., Ultrahigh Photoresponse of Few-Layer TiS3 Nanoribbon Transistors. *Advanced Optical Materials* **2014,** *2* (7), 641-645.

47. Island, J. O.; Biele, R.; Barawi, M.; Clamagirand, J. M.; Ares, J. R.; Sánchez, C.; van der Zant, H. S.; Ferrer, I. J.; D'Agosta, R.; Castellanos-Gomez, A., Titanium trisulfide (TiS3): a 2D semiconductor with quasi-1D optical and electronic properties. *Scientific reports* **2016,** *6*.

48. Island, J. O.; Barawi, M.; Biele, R.; Almazán, A.; Clamagirand, J. M.; Ares, J. R.; Sánchez, C.; van der Zant, H. S.; Álvarez, J. V.; D'Agosta, R., TiS3 transistors with tailored morphology and electrical properties. *Advanced Materials* **2015,** *27* (16), 2595-2601.

49. Gard, P.; Cruege, F.; Sourisseau, C.; Gorochov, O., Single-crystal micro-Raman studies of ZrS3, TiS3 and several Zr1–xTixS3 compounds ($0< x\leqslant 0.33$). *Journal of Raman spectroscopy* **1986,** *17* (3), 283-288.

50. Hart, L.; Dale, S.; Hoye, S.; Webb, J. L.; Wolverson, D., Rhenium dichalcogenides: layered semiconductors with two vertical orientations. *Nano letters* **2016,** *16* (2), 1381-1386.

51. Yang, S.; Tongay, S.; Li, Y.; Yue, Q.; Xia, J.-B.; Li, S.-S.; Li, J.; Wei, S.-H., Layer-dependent electrical and optoelectronic responses of ReSe 2 nanosheet transistors. *Nanoscale* **2014,** *6* (13), 7226-7231.

52. Zhang, E.; Jin, Y.; Yuan, X.; Wang, W.; Zhang, C.; Tang, L.; Liu, S.; Zhou, P.; Hu, W.; Xiu, F., ReS2-Based Field-Effect Transistors and Photodetectors. *Advanced Functional Materials* **2015,** *25* (26), 4076-4082.

53. Aslan, O. B.; Chenet, D. A.; van der Zande, A. M.; Hone, J. C.; Heinz, T. F., Linearly Polarized Excitons in Single-and Few-Layer ReS2 Crystals. *ACS Photonics* **2015,** *3* (1), 96-101.

54. Keyshar, K.; Gong, Y.; Ye, G.; Brunetto, G.; Zhou, W.; Cole, D. P.; Hackenberg, K.; He, Y.; Machado, L.; Kabbani, M., Chemical vapor deposition of monolayer rhenium disulfide (ReS2). *Advanced Materials* **2015,** *27* (31), 4640-4648.

55. Ning, C.-Z.; Dou, L.; Yang, P., Bandgap engineering in semiconductor alloy nanomaterials with widely tunable compositions. *Nature Reviews Materials* **2017,** *2* (12), 17070.

56. Schnohr, C., Compound semiconductor alloys: From atomic-scale structure to bandgap bowing. *Applied physics reviews* **2015,** *2* (3), 031304.

57. Kuech, T. F.; Mawst, L. J.; Brown, A. S., Mixed Semiconductor Alloys for Optical Devices. *Annual review of chemical and biomolecular engineering* **2013,** *4*, 187-209.

58. Yin, Z.; Tang, X., A review of energy bandgap engineering in III–V semiconductor alloys for mid-infrared laser applications. *Solid-state electronics* **2007,** *51* (1), 6-15.

59. Feng, Q.; Zhu, Y.; Hong, J.; Zhang, M.; Duan, W.; Mao, N.; Wu, J.; Xu, H.; Dong, F.; Lin, F., Growth of Large-Area 2D MoS2 (1-x) Se2x Semiconductor Alloys. *Advanced Materials* **2014,** *26* (17), 2648-2653.

60. Li, H.; Duan, X.; Wu, X.; Zhuang, X.; Zhou, H.; Zhang, Q.; Zhu, X.; Hu, W.; Ren, P.; Guo, P., Growth of Alloy MoS2 x Se2 (1–x) Nanosheets with Fully Tunable Chemical Compositions and Optical Properties. *Journal of the American Chemical Society* **2014,** *136* (10), 3756-3759.

61. Li, H.; Zhang, Q.; Duan, X.; Wu, X.; Fan, X.; Zhu, X.; Zhuang, X.; Hu, W.; Zhou, H.; Pan, A., Lateral Growth of Composition Graded Atomic Layer MoS2 (1–x) Se2 x Nanosheets. *Journal of the American Chemical Society* **2015,** *137* (16), 5284-5287.

62. Klee, V.; Preciado, E.; Barroso, D.; Nguyen, A. E.; Lee, C.; Erickson, K. J.; Triplett, M.; Davis, B.; Lu, I.-H.; Bobek, S., Superlinear Composition-Dependent Photocurrent in CVD-Grown Monolayer MoS2 (1–x) Se2 x Alloy Devices. *Nano letters* **2015,** *15* (4), 2612-2619.

63. Su, S.-H.; Hsu, W.-T.; Hsu, C.-L.; Chen, C.-H.; Chiu, M.-H.; Lin, Y.-C.; Chang, W.-H.; Suenaga, K.; He Jr, -. H.; Li, L.-J., Controllable synthesis of band-gap-tunable and monolayer transition-metal dichalcogenide alloys. *Frontiers in Energy Research* **2014,** *2*, 27.

64. Duan, X.; Wang, C.; Fan, Z.; Hao, G.; Kou, L.; Halim, U.; Li, H.; Wu, X.; Wang, Y.; Jiang, J., Synthesis of WS2 x Se2–2 x Alloy Nanosheets with Composition-Tunable Electronic Properties. *Nano letters* **2015,** *16* (1), 264-269.

65. Fu, Q.; Yang, L.; Wang, W.; Han, A.; Huang, J.; Du, P.; Fan, Z.; Zhang, J.; Xiang, B., Synthesis and enhanced electrochemical catalytic performance of monolayer WS2 (1–x) Se2x with a tunable band gap. *Advanced Materials* **2015,** *27* (32), 4732-4738.

66. Wen, W.; Zhu, Y.; Liu, X.; Hsu, H. P.; Fei, Z.; Chen, Y.; Wang, X.; Zhang, M.; Lin, K. H.; Huang, F. S., Anisotropic Spectroscopy and Electrical Properties of 2D ReS2 (1–x) Se2x Alloys with Distorted 1T Structure. *small* **2017,** *13* (12).

67. Cui, F.; Feng, Q.; Hong, J.; Wang, R.; Bai, Y.; Li, X.; Liu, D.; Zhou, Y.; Liang, X.; He, X., Synthesis of Large-Size 1T′ ReS2xSe2 (1− x) Alloy Monolayer with Tunable Bandgap and Carrier Type. *Advanced Materials* **2017,** *29* (46).

68. Song, J.-G.; Ryu, G. H.; Lee, S. J.; Sim, S.; Lee, C. W.; Choi, T.; Jung, H.; Kim, Y.; Lee, Z.; Myoung, J.-M., Controllable synthesis of molybdenum tungsten disulfide alloy for vertically composition-controlled multilayer. *Nature communications* **2015,** *6*, 7817.

69. Zheng, S.; Sun, L.; Yin, T.; Dubrovkin, A. M.; Liu, F.; Liu, Z.; Shen, Z. X.; Fan, H. J., Monolayers of WxMo1− xS2 alloy heterostructure with in-plane composition variations. *Applied Physics Letters* **2015,** *106* (6), 063113.

70. Zhang, W.; Li, X.; Jiang, T.; Song, J.; Lin, Y.; Zhu, L.; Xu, X., CVD synthesis of Mo (1− x) W x S 2 and MoS 2 (1− x) Se 2x alloy monolayers aimed at tuning the bandgap of molybdenum disulfide. *Nanoscale* **2015,** *7* (32), 13554-13560.

71. Gan, L.-Y.; Zhang, Q.; Zhao, Y.-J.; Cheng, Y.; Schwingenschlögl, U., Order-disorder phase transitions in the two-dimensional semiconducting transition metal dichalcogenide alloys Mo 1− x W x X 2 (X= S, Se, and Te). *Scientific reports* **2014,** *4*, 6691.

72. Keum, D. H.; Cho, S.; Kim, J. H.; Choe, D.-H.; Sung, H.-J.; Kan, M.; Kang, H.; Hwang, J.-Y.; Kim, S. W.; Yang, H., Bandgap opening in few-layered monoclinic MoTe 2. *Nature Physics* **2015,** *11* (6), 482.

73. Zhou, J.; Liu, F.; Lin, J.; Huang, X.; Xia, J.; Zhang, B.; Zeng, Q.; Wang, H.; Zhu, C.; Niu, L., Large-area and high-quality 2D transition metal telluride. *Advanced Materials* **2017,** *29* (3).

74. Cho, S.; Kim, S.; Kim, J. H.; Zhao, J.; Seok, J.; Keum, D. H.; Baik, J.; Choe, D.-H.; Chang, K.; Suenaga, K., Phase patterning for ohmic homojunction contact in MoTe2. *Science* **2015,** *349* (6248), 625-628.

75. Rhodes, D.; Chenet, D.; Janicek, B.; Nyby, C.; Lin, Y.; Jin, W.; Edelberg, D.; Mannebach, E.; Finney, N.; Antony, A., Engineering the structural and electronic phases of MoTe2 through W substitution. *Nano letters* **2017,** *17* (3), 1616-1622.

76. Lv, Y.-Y.; Cao, L.; Li, X.; Zhang, B.-B.; Wang, K.; Pang, B.; Ma, L.; Lin, D.; Yao, S.-H.; Zhou, J., Composition and temperature-dependent phase transition in miscible Mo 1− x W x Te 2 single crystals. *Scientific reports* **2017,** *7*, 44587.

77. Oliver, S. M.; Beams, R.; Krylyuk, S.; Kalish, I.; Singh, A. K.; Bruma, A.; Tavazza, F.; Joshi, J.; Stone, I. R.; Stranick, S. J., The structural phases and vibrational properties of Mo1− xWxTe2 alloys. *2D Mat.* **2017,** *4* (4), 045008.

78. Li, H.; Duan, X.; Wu, X.; Zhuang, X.; Zhou, H.; Zhang, Q.; Zhu, X.; Hu, W.; Ren, P.; Guo, P.; Ma, L.; Fan, X.; Wang, X.; Xu, J.; Pan, A.; Duan, X., Growth of Alloy MoS2xSe2(1–x) Nanosheets with Fully Tunable Chemical Compositions and Optical Properties. *Journal of the American Chemical Society* **2014,** *136* (10), 3756-3759.

79. Wang, Y.; Xiao, J.; Zhu, H.; Li, Y.; Alsaid, Y.; Fong, K. Y.; Zhou, Y.; Wang, S.; Shi, W.; Wang, Y., Structural phase transition in monolayer MoTe 2 driven by electrostatic doping. *Nature* **2017,** *550* (7677), 487.

80. Controlled buckling of semiconductor nanoribbons for stretchable electronics. *Controlled buckling of semiconductor nanoribbons for stretchable electronics*.

81. Furuseth, S.; Brattas, L.; Kjekshus, A., Crystal Structures of TiS 3, ZrS 3, ZrSe 3, ZrTe 3, HfS 3 and HfSe 3. *Acta Chemica Scandinavica* **1975,** *29*, 623.

82. Zhou, J.; Lin, J.; Huang, X.; Zhou, Y.; Chen, Y.; Xia, J.; Wang, H.; Xie, Y.; Yu, H.; Lei, J., A library of atomically thin metal chalcogenides. *Nature* **2018,** *556* (7701), 355.

83. Jayaraman, A., Diamond anvil cell and high-pressure physical investigations. *Reviews of Modern Physics* **1983,** *55* (1), 65-108.

84. Mao, H. K.; Bell, P. M.; Shaner, J. W.; Steinberg, D. J., Specific volume measurements of Cu, Mo, Pd, and Ag and calibration of the ruby R1 fluorescence pressure gauge from 0.06 to 1 Mbar. *Journal of Applied Physics* **1978,** *49* (6), 3276-3283.

85. Zhao, J.; Hearne, G.; Maaza, M.; Nieuwoudt, M. K.; Comins, J. D., Multi-aperture gasket for experiments at high pressure in a diamond-anvil cell. *Review of Scientific Instruments* **2000,** *71* (12), 4509-4511.

86. Forman, R. A.; Piermarini, G. J.; Barnett, J. D.; Block, S., Pressure Measurement Made by the Utilization of Ruby Sharp-Line Luminescence. *Science* **1972,** *176* (4032), 284-285.

87. Loudon, R., The Raman effect in crystals. *Advances in Physics* **1964,** *13* (52), 423-482.

88. Shengxue, Y.; Yanhan, Y.; Minghui, W.; Chunguang, H.; Wanfu, S.; Yongji, G.; Li, H.; Chengbao, J.; Yongzhe, Z.; M., A. P., Highly In-Plane Optical and Electrical Anisotropy of 2D Germanium Arsenide. *Adv. Funct. Mater.* **2018,** *28* (16), 1707379.

89. Kresse, G.; Furthmüller, J., Efficient iterative schemes for ab initio total-energy calculations using a plane-wave basis set. *Physical review B* **1996,** *54* (16), 11169.

90. Kresse, G.; Furthmüller, J., Efficiency of ab-initio total energy calculations for metals and semiconductors using a plane-wave basis set. *Computational Materials Science* **1996,** *6* (1), 15-50.

91. Perdew, J. P.; Burke, K.; Ernzerhof, M., Generalized gradient approximation made simple. *Physical review letters* **1996,** *77* (18), 3865.

92. Blöchl, P. E., Projector augmented-wave method. *Physical Review B* **1994,** *50* (24), 17953.

93. Kresse, G.; Joubert, D., From ultrasoft pseudopotentials to the projector augmented-wave method. *Physical Review B* **1999,** *59* (3), 1758.

94. Alfè, D., PHON: A program to calculate phonons using the small displacement method. *Computer Physics Communications* **2009,** *180* (12), 2622-2633.

95. Kresse, G.; Furthmüller, J., Efficient iterative schemes for ab initio total-energy calculations using a plane-wave basis set. *Phys. Rev. B* **1996,** *54* (16), 11169-11186.

96. Zunger, A.; Wei, S. H.; Ferreira, L. G.; Bernard, J. E., Special quasirandom structures. *Phys. Rev. Lett.* **1990,** *65* (3), 353-356.

97. van de Walle, A., Multicomponent multisublattice alloys, nonconfigurational entropy and other additions to the Alloy Theoretic Automated Toolkit. *Calphad* **2009,** *33* (2), 266-278.

98. Perdew, J. P.; Burke, K.; Ernzerhof, M., Generalized Gradient Approximation Made Simple. *Phys. Rev. Lett.* **1996,** *77* (18), 3865-3868.

99. Blöchl, P. E., Projector augmented-wave method. *Phys. Rev. B* **1994,** *50* (24), 17953-17979.

100. Kresse, G.; Joubert, D., From ultrasoft pseudopotentials to the projector augmented-wave method. *Phys. Rev. B* **1999,** *59* (3), 1758-1775.

101. Sambongi, T.; Tsutsumi, K.; Shiozaki, Y.; Yamamoto, M.; Yamaya, K.; Abe, Y., Peierls transition in TaS3. *Solid State Communications* **1977,** *22* (12), 729-731.

102. Thompson, A.; Zettl, A.; Grüner, G., Charge-Density-Wave Transport in Ta S 3. *Physical Review Letters* **1981,** *47* (1), 64.

103. Nad, F.; Monceau, P., Charge-density-wave glass state in quasi-one-dimensional conductors. *Physical Review B* **1995,** *51* (4), 2052.

104. Sugai, S., Effect of the charge-density-wave gap on the Raman spectra in orthorhombic Ta S 3. *Physical Review B* **1984,** *29* (2), 953.

105. Tsang, J.; Hermann, C.; Shafer, M., Raman Spectroscopy of the Charge-Density-Wave State in Ta S 3. *Physical Review Letters* **1978,** *40* (23), 1528.

106. Monteverde, M.; Lorenzana, J.; Monceau, P.; Nunez-Regueiro, M., Quantum critical point and superconducting dome in the pressure phase diagram of o-TaS 3. *Physical Review B* **2013,** *88* (18), 180504.

107. Meerschaut, A.; Guemas, L.; Rouxel, J., Structure and properties of the new phase of the pseudo one-dimensional compound TaS 3. *Journal of Solid State Chemistry* **1981,** *36* (1), 118-123.

108. Kikkawa, S.; Ogawa, N.; Koizumi, M.; Onuki, Y., High-pressure syntheses of TaS 3, NbS 3, TaSe 3, and NbSe 3 with NbSe 3-type crystal structure. *Journal of Solid State Chemistry* **1982,** *41* (3), 315-322.

109. Wu, K.; Torun, E.; Sahin, H.; Chen, B.; Fan, X.; Pant, A.; Parsons Wright, D.; Aoki, T.; Peeters, F. M.; Soignard, E.; Tongay, S., Unusual lattice vibration characteristics in whiskers of the pseudo-one-dimensional titanium trisulfide TiS3. **2016,** *7*, 12952.

110. Cai, H.; Chen, B.; Wang, G.; Soignard, E.; Khosravi, A.; Manca, M.; Marie, X.; Chang, S. L.; Urbaszek, B.; Tongay, S., Synthesis of Highly Anisotropic Semiconducting GaTe Nanomaterials and Emerging Properties Enabled by Epitaxy. *Advanced Materials* **2017,** *29* (8).

111. Wu, K.; Chen, B.; Yang, S.; Wang, G.; Kong, W.; Cai, H.; Aoki, T.; Soignard, E.; Marie, X.; Yano, A., Domain architectures and grain boundaries in chemical vapor deposited highly anisotropic ReS2 monolayer films. *Nano letters* **2016,** *16* (9), 5888-5894.

112. Rijnsdorp, J.; Jellinek, F., The crystal structure of niobium trisulfide, NbS3. *Journal of Solid State Chemistry* **1978,** *25* (4), 325-328.

113. Wieting, T. J.; Grisel, A.; Lévy, F., Lattice dynamical study of the low-dimensional type B compounds TiS3, HfSe3 and ZrTe3. *Physica B+C* **1981,** *105* (1), 366-369.

114. Sourisseau, C.; Cavagnat, R.; Fouassier, M.; Maraval, P., Electronic, vibrational and resonance Raman spectra of the layered semiconducting compound NbS3. *Journal of Raman Spectroscopy* **1990,** *21* (6), 337-349.

APPENDIX A

STATEMENT OF COAUTHORS' PERMISSIONS

I, Kedi Wu, committed that all co-authors have granted their permissions for the usage of following publications in this dissertation.

1. Kedi Wu, Engin Torun, Hasan Sahin, Bin Chen, Xi Fan, Anupum Pant, David Parsons Wright et al. "Unusual lattice vibration characteristics in whiskers of the pseudo-one-dimensional titanium trisulfide TiS_3." Nature communications 7 (2016): 12952.

2. Kedi Wu, Bin Chen, Sijie Yang, Gang Wang, Wilson Kong, Hui Cai, Toshihiro Aoki et al. "Domain architectures and grain boundaries in chemical vapor deposited highly anisotropic ReS_2 monolayer films." Nano letters 16, no. 9 (2016): 5888-5894.

3. Kedi Wu, Bin Chen, Hui Cai, Mark Blei, Juliana Bennett, Shengxue Yang, David Wright, Yuxia Shen, and Sefaattin Tongay. "Unusual Pressure Response of Vibrational Modes in Anisotropic TaS_3." The Journal of Physical Chemistry C 121, no. 50 (2017): 28187-28193.